

# Chapter 5

## Charged Particle Identification System

### 5.1 Introduction

Charged particle identification is an absolute requirement for a modern experiment designed to study the decays of  $b$  and  $c$  quarks. The forward geometry is well suited for a Ring Imaging Cherenkov detector (RICH), that provides powerful particle ID capabilities over a broad range of momentum. Even with the excellent mass resolution of BTeV, there are kinematic regions where signals from one final state will overlap those of another final state. For example,  $B_s \rightarrow D_s K^-$  signal must be distinguished from  $B_s \rightarrow D_s \pi^-$  background in order to measure the CKM phase  $\gamma$ . These ambiguities can be eliminated almost entirely by an effective particle identifier. In addition, many physics investigations involving neutral  $B$ -mesons require “tagging” of the flavor of the signal particle by examining the properties of the “away-side.” Our studies show that kaon tagging is a very effective means of doing this. “Same-side” kaon tagging is also very effective for  $B_s$  mesons.

The RICH detector is located downstream of a 1.6T dipole magnet surrounding the interaction region. It consists of two independent systems. The main system has a 3 m long  $C_4F_8O$  gas volume. Charged particles radiate Cherenkov light in this medium. The light is focused with a segmented mirror onto an array of photodetectors sensitive to light between 280 – 600 nm. These photodetectors can either be multi-anode photomultiplier tubes (MAPMT) or hybrid photodiodes (HPD). The MAPMT is a square device approximately 1” on a side with 16 channels, while the HPD is circular in cross-section with a diameter of about 6.8”. All costing is done assuming MAPMTs that have recently been upgraded. HPDs provide a competitive alternative. Both systems yield about the same number of Cherenkov photons, but currently the MAPMTs are less expensive due to changes in the exchange rates over the last year, and are easier to operate. Therefore we have adopted the MAPMT based system for our baseline.

The second system, used mainly for separating kaons and protons below 10 GeV/c, consists of a liquid  $C_5F_{12}$  radiator, approximately 1 cm thick, placed in front of the gas

volume. Cherenkov photons generated in this medium exit the sides of the gas tank and are detected in an array of 3" diameter photomultiplier tubes. The liquid is contained by the front face of the RICH tank and a 3 mm thick quartz window. There is a 40 cm<sup>2</sup> hole around the beam pipe to avoid radiation from fast particles.

## 5.2 Requirements

### 5.2.1 Physics Requirements

The following requirements describe the RICH detector performance goals dictated by the physics goals of BTeV. The momentum range over which excellent hadron identification is required is between 3 and 70 GeV/c. The low momentum hadron identification optimizes flavor tagging, whereas the high momentum range will enable us to separate  $\pi$ 's and K's from two body B-meson decays. Excellent identification should be provided in the full BTeV solid angle (10-300 mrad). Besides providing excellent hadron identification, the RICH detector is also an integral part of the lepton identification system in the solid angle between 200 and 300 mrad. It is the only detector element available to distinguish  $e$ ,  $\mu$  and hadron species, as the muon detector and the electromagnetic calorimeter have smaller solid angle coverage.

#### 5.2.1.1 Cherenkov Angular Resolution per Track

The separation of charged hadrons into different species will be accomplished in the data analysis by characterizing each charged track with a set of probabilities for being an electron, muon, pion, kaon, or proton. From a knowledge of the distribution of Cherenkov angular resolutions per track such probabilities can be derived.

It has proven useful to specify RICH detectors by their average Cherenkov resolution per track, and we shall do so here. For example, the difference in emission angle of Cherenkov photons from pions and kaons at 70 GeV/c (the upper range for which we require excellent particle identification performance) is 0.44 mrad, so achieving a resolution per track of 0.11 mrad would give a separation of 4 standard deviations. Separation improves dramatically as momentum decreases. Furthermore, the average Cherenkov resolution per track can be understood in terms of the average Cherenkov resolution per photon and the number of photons. A separation of at least  $4\sigma$  for  $\pi$ ,  $K$  and  $p$  in the momentum range of 3-70 GeV/c (or from their Cherenkov photon threshold to 70 GeV/c) is required.

- **Requirements for Gaseous RICH**

- **Average Cherenkov Resolution per Track:** The average Cherenkov angle resolution per track shall be better than 0.12 mrad. This requirement may be met with the following set of parameters:
  - \* The distribution of Cherenkov photons about the correct Cherenkov angle should have an r.m.s. deviation of no more than 0.85 mrad.

- \* The number of Cherenkov photons per track should average at least 50 for tracks in the plateau region.

- **Requirements for Liquid RICH**

- **Average Cherenkov Resolution per Track:** The average Cherenkov angle resolution per track shall be better than 1.9 mrad. This requirement may be met with the following set of parameters:
  - \* The distribution of Cherenkov photons about the correct Cherenkov angle should have an r.m.s. deviation of no more than 6.5 mrad.
  - \* The number of Cherenkov photons per track should average at least 12 in the plateau region.

## 5.2.2 Radiation hardness

The highest radiation in the RICH detector occurs at the entrance and exit windows. Fortunately these are not active components. The MAPMT array is shielded by the magnet and only  $\sim 20\%$  of the photomultiplier tubes in the liquid system see any significant radiation. These are in a narrow cone at the top and bottom of the detector where the magnetic field sweeps slower charged particles. The window containing the liquid is made of quartz, a radiation hard material and doesn't exist in the highest radiation area due to the hole near the beam.

## 5.2.3 Geometrical Requirements

- **Size of RICH Detector:** The RICH detector must subtend at least  $\pm 300$  mrad both horizontally and vertically with respect to the beam axis.
- **Alignment:** The RICH system must be mechanically stable. The mirrors must be aligned so the aberration does not degrade the resolution. Furthermore, the MAPMT position with respect to the mirror focus must be determined to better than  $1/10$  of the MAPMT pixel width.
- **Thickness:** The RICH detector must be of minimal material thickness. The total number of radiation lengths allowed less than 20% of a radiation length.

## 5.2.4 Mirror Requirements

The RICH-mirror system should be designed so that its effect on the total Cherenkov angle resolution per track is not significantly increased for reasons stated in Section 5.2.1. The mirror system consists of segmented mirrors put together to form two big mirrors, each one having a mean radius of curvature  $R_{mean} = 697$  cm and an aperture of 220 cm x 440 cm. One of them will be positioned in the positive  $x$ -direction and tilted by 261 mrad clockwise

and the other one will be positioned in the negative  $x$ -direction and tilted by 261 mrad counter-clockwise. The mirror system requirement can be divided into three categories, namely:

- **Material requirement:** We require the radiation length to be  $< 2\%$  at normal incidence to the mirror. A protective coating for the mirror is also required. This coating should have 99 % transmission at 280 nm.
- **Geometrical requirement:** The mean radius of all mirror tiles must lie within  $697 \pm 3$  cm. The maximum shift of any tile from the mean is allowed to be  $\pm 3$  cm. The surface smoothness must be less than 2.8 nm.
- **Optical requirement:** We define a quantity called spot-size which is the diameter of the circle where 95% of the light reflected from the entire mirror is focused. From simulation, we determine that the spot-size must be less than 2.5 mm.
- **Reflectivity:** The mirror must reflect 90% of the light averaged over the entire surface for wavelengths larger than 280 nm.

### 5.2.5 Electronics Requirements

The baseline photosensitive device MAPMT associated with the gas RICH poses stringent requirements on the electronics in terms of the data rate and throughput at least in the highest occupancy region. The backup HPD system also depends critically on low noise. The expected signal level in the MAPMT's has an approximately flat distribution from threshold up to about  $10^6$  electrons, while the expected signal level from the HPDs is about 5,000 electrons. Thus, we require very low noise front-end electronics for the HPDs, while for MAPMTs, an increase in noise will just reduce somewhat the level of signal photons. Although the average occupancy of the BTeV RICH detector is very small (0.75% hits/pixel), in the hottest MAPMT the number of hits in an event can be as high as 9, with 11% of the events having more than 4 hits per tube, according to a Monte Carlo simulation based on an average of 6 interactions per crossing.

- **Noise of the front end:** The equivalent noise charge of the front end electronics when connected to the MAPMT will be less than or equal to  $1000 e^-$ , or  $500 e^-$  if the backup HPD system is used.
- **Speed:** The analog signal should have a peaking time of about 75 ns and a fall time (10 % of the peak) of 200 ns.
- **Event rate:** All the building blocks of the front end electronics (preamplifier and shaper, gain stage, discriminator, digital architecture) need to be able to process event at a rate of 7.5 MHz without degradation of the performance.

- **Data rate:** The front end electronics will provide digital information of the MAPMT pads hit by a photoelectron within the beam crossing when the event was originated.
- **Threshold uniformity:** Each front end electronics ASIC will have a global threshold, settable by an external DAC that spans the whole dynamic range of the chip (0-6000  $e^-$ ). Moreover a fine tuning of the individual channel threshold will be built within the chip. This fine tuning needs to maintain the threshold dispersion below 200  $e^-$  per chip.
- **Masking out bad channels:** It should be possible to mask out bad channels by digital control.
- **Electronics calibration:** It is necessary to be able to inject a calibration charge on each individual channel to characterize the ASIC performance with the expected signal level.
- **Chip initialization and readback of the downloaded information:** The mode of operation of the chip (calibration/data taking, individual thresholds, active channel mask) needs to be initialized with a serial bit pattern. The downloaded information needs to be available to be read back for diagnostic purposes.
- The hybrids need to have a dead channel count below 1% (at most 1 dead channel per hybrid).

### 5.2.6 Readout Requirements

The success of the experiment relies critically on the quality of the data provided to the data acquisition system.

- **Data Sparsification:** The data output from the detector includes only those cells that are above a settable threshold.
- **RICH output data content:** The hit data must include the beam crossing number, chip identification number, and the addresses of all hit pixels for that beam crossing.
- **Data Rate:** The noise level should be such that the maximum data rate should not exceed an average of 4% of the  $\sim 154,000$  channels.
- **Readout Abort:** The system must have a means of recognizing and aborting the readout of any chip that has an unusually high volume of data output (*e.g.* all the channels lit up).
- **Remote programming of local FPGA's:** All the FPGA's located in the front end devices must be remotely re-programmable from the slow control lines if necessary.

### 5.2.7 Electrical and magnetic interference

The readout chip must be shielded electronically from external noise (MAPMT HV, sensor bias...). Common mode noise arising from the experimental environment should be kept well below the intrinsic noise performance of the front end electronics. Adequate shielding of the analog front end should be part of the final packaging of the devices.

### 5.2.8 Mechanical Properties of the front end hybrids

For the baseline MAPMT system, the 128 channel hybrids must fit within the profile of the 8 tubes (4x2 array) that they are connected to. For the backup HPD system, the front end hybrid should be composed of a rigid component (hyb-A) hosting the analog front end devices, connected via a flex portion (flex) to a rigid component including the logic periphery (hyb-B).

- **Mechanical clearance of hyb-A:** In the case of the HPD, the component hyb-A must be small enough to fit inside the mu-metal shield surrounding the HPD and have holes in locations specified in accordance with the overall HPD support structure.
- **flex mechanical properties:** In the case of the HPD, the flex component of the hybrid must maintain signal line integrity upon the tight bend required to fit into the HPD mechanical structure.

### 5.2.9 Cooling System

Both the gas and liquid system will require active cooling. In the gas RICH, the baseline MAPMT system we need to cool both the readout chips and the bases. For the backup HPD system, the heat load is dominated by the readout chips. The liquid RICH will also require cooling of the bases and the readout chips.

### 5.2.10 Gas and Liquid Systems

The gas and liquid systems both recirculate their respective fluids. Since neither system operates below 280 nm, purity is not an issue in terms of the photon yield. However, the changes induced by impurities to the index of refraction can be a problem, thus we specify that the purity is monitored in both systems. Moreover both systems are cleaned with appropriate techniques to maintain the purity specified below.

- **Gas System Purity:** The  $C_4F_8O$  system shall recirculate gas. By means of standard filtering techniques, the gas purity shall be maintained at better than 99%.
- **Liquid System Purity:** The  $C_5F_{12}$  system shall recirculate liquid. By means of standard filtering techniques, the purity shall be maintained at better than 99%.

- **Gas System for HPD:** The HPD array shall be provided a separate gas system that is resistant to electrical breakdown, necessary because of the 20 kV required by the HPD's. This gas may be sulphur-hexafluoride. This is not required for the baseline MAPMT system.

### 5.2.11 Power Supplies

The MAPMTs are run close to 900 V. There are 3 separate high voltages to be supplied to the HPD's: 20 kV, 19.89 kV, and 15.6 kV. In addition there is a low voltage of  $\sim 60$  V supplied to the silicon sensor inside the HPD. The PMTs system requires 1000 V.

- **Ripple:** The high voltage supplied to the MAPMT must have a ripple on the voltage low enough not to increase the gain variation by more than 25% or the electronic noise by more than 10%.

All high voltages to the HPD must have a ripple on the voltage sufficiently small over the entire frequency range so not to increase the electronic noise by more than 5%. This may be accomplished by either using a very low ripple power supply, or by using an RC filter close to the detector.

- **Voltage reference/grounding:** All low and high voltage power supplies will be floating. Each RICH photosensitive element assembly will have one well-defined local ground and defined isolation (resistive and/or capacitive) from other grounds. The design must take safety of equipment and personnel as well as ground loop avoidance and other noise prevention into consideration.

### 5.2.12 Monitoring

#### Monitoring of the RICH

To check the performance and the safe operation of the RICH System, we need to monitor several items:

- **Temperature & Humidity Monitoring:** The RICH monitoring system should check temperature at  $\sim 16$  individual points in the gas, and in the liquid. We will also monitor the temperature in the collision hall. Each hybrid will be monitored by a thermistor. The humidity in the HPD array must be measured and kept below 5% to avoid corona discharge. For the baseline MAPMT system, the humidity should be kept below 40%.
- **High Voltage & Low Voltage Monitoring:** All voltages and currents must be read back from the detectors and their values displayed. All currents must also be monitored.

- **Alarms:** Appropriate limits should be set on the parameters that are being monitored and an alarm will be issued if these limits are exceeded. In some cases, the alarm should automatically start a turn-off sequence to prevent any major damage to the system. In other cases, it will provide a warning.

### 5.2.13 Electrical Requirements

The hardware that is designed and built, or purchased to implement the RICH system will consist of digital electronics. This hardware must comply with the *BTeV Digital Electronics Standards* document. This document contains requirements, standards, and recommendations that apply to all digital electronics in BTeV. The subjects that are addressed in the document include interfaces, grounding, EMI, shielding, infrastructure, safety, reliability, and maintainability.

### 5.2.14 Electronics Protection

BTeV will have a committee to review component electronics protection proposals. BTeV management will provide documents defining acceptable electronics protection procedures. The RICH System should observe all safety rules and regulations as detailed in the BTeV Safety Requirement Document. A series of interlocks and alarms should be in place.

### 5.2.15 Functional Requirements

In order to fully exploit the photodetector capabilities and achieve the required resolution on the Cherenkov ring, the mirror panels need to be carefully aligned with respect to each other and with respect to the MAPMT planes.

- **Mirror Alignment:** The mirror panels will be aligned in the experimental hall with accuracy consistent with the geometrical requirements described in Section 5.5.4.
- **MAPMT Alignment:** The MAPMT position in the detector will be aligned with respect to the mirror surface with accuracy consistent with the geometrical requirements described in Section 5.5.4.
- **Access:** It should be possible to access individual MAPMT (or HPD) modules, PMT modules and Mirror panels for adjustment or repair.

### 5.2.16 Requirements on Rest of BTeV

- **Stray Magnetic fields:** The magnetic field in the region of the MAPMT and PMT arrays must be enclosed in a shield adequate to keep the magnetic field below 10 Gauss, without individual shielding of the devices. (Mu-metal shields then will reduce the field below our level of sensitivity).



- **Beryllium Beam Pipe:** The beam pipe between the magnet and the end of the RICH detector needs to be made of thin Beryllium to minimize the radiation lengths in order to keep the backgrounds at an acceptable level.
- **Tracking:** Tracking must be provided before and after the RICH detector. The current requirements for the Straw and Silicon systems are adequate for our purposes.
- **Operating Temperature:** The operating temperature of the detector must be kept below 28°C, otherwise the liquid radiator will become gaseous. The temperature variation should be kept within  $\pm 2$  °C. The temperature need not be uniform across the entire detector.

## 5.3 Technical Description

The RICH detector consists of two separate subsystems that share the same space along the beam line, as shown in Fig. 5.1. The main system consists of a 3 m long  $C_4F_8O$  gas radiator, a focusing mirror and a photon detector consisting of arrays of multi-anode photomultipliers (MAMPT) or hybrid photo-diodes (HPD) that have pixilated elements approximately 6 mm x 6 mm in size. An example of simulated Cherenkov rings detected in the gaseous RICH is shown in Fig. 5.2. The second system consists of a 1 cm thick  $C_5F_{12}$  liquid radiator and an array of standard 3" photomultiplier tubes placed on the sides of the gas radiator tank. Cherenkov rings created in the liquid radiator are directly projected onto the photomultiplier arrays (so called "proximity focusing"). An example of simulated Cherenkov rings detected in the liquid radiator RICH is shown in Fig. 5.3. In this section we discuss the motivation for the technology choices and then we describe each of the major components of the RICH.

### 5.3.1 Selection of RICH Radiators

Because of the large particle momenta there is really only one choice of detector technology: a gaseous ring-imaging Cherenkov detector. Pions and kaons can be separated in the required momentum region with a single gas radiator (see Fig. 5.4). Initially we chose  $C_4F_{10}$  (the heaviest RTP gas) and assumed an index of refraction of approximately 1.00138 in the visible range [5]. This gas has been used by DELPHI (endcap) [1], HERA-B [2] and HERMES [3]. It was also the choice for one of the LHCb RICH detectors [4].

Unfortunately, the main manufacturer of  $C_4F_{10}$ , the 3M company, recently stopped producing this gas. Although still available, the price has risen by a factor of five and we do not believe that the source is stable. To determine a replacement we needed to measure the refractive index of different gases to determine if they were suitable. Fig. 5.5 shows our measurements of refractive indices as a function of wavelength for three different gases, the original  $C_4F_{10}$ ,  $C_4F_8O$  and  $C_4F_8$ . The curve is the one we have been using in our simulations; it is contained in a HERAb thesis and appears to be an extrapolation of DELPHI measurements that were done in the UV. Fortunately the  $C_4F_8O$  falls right on the curve and use of

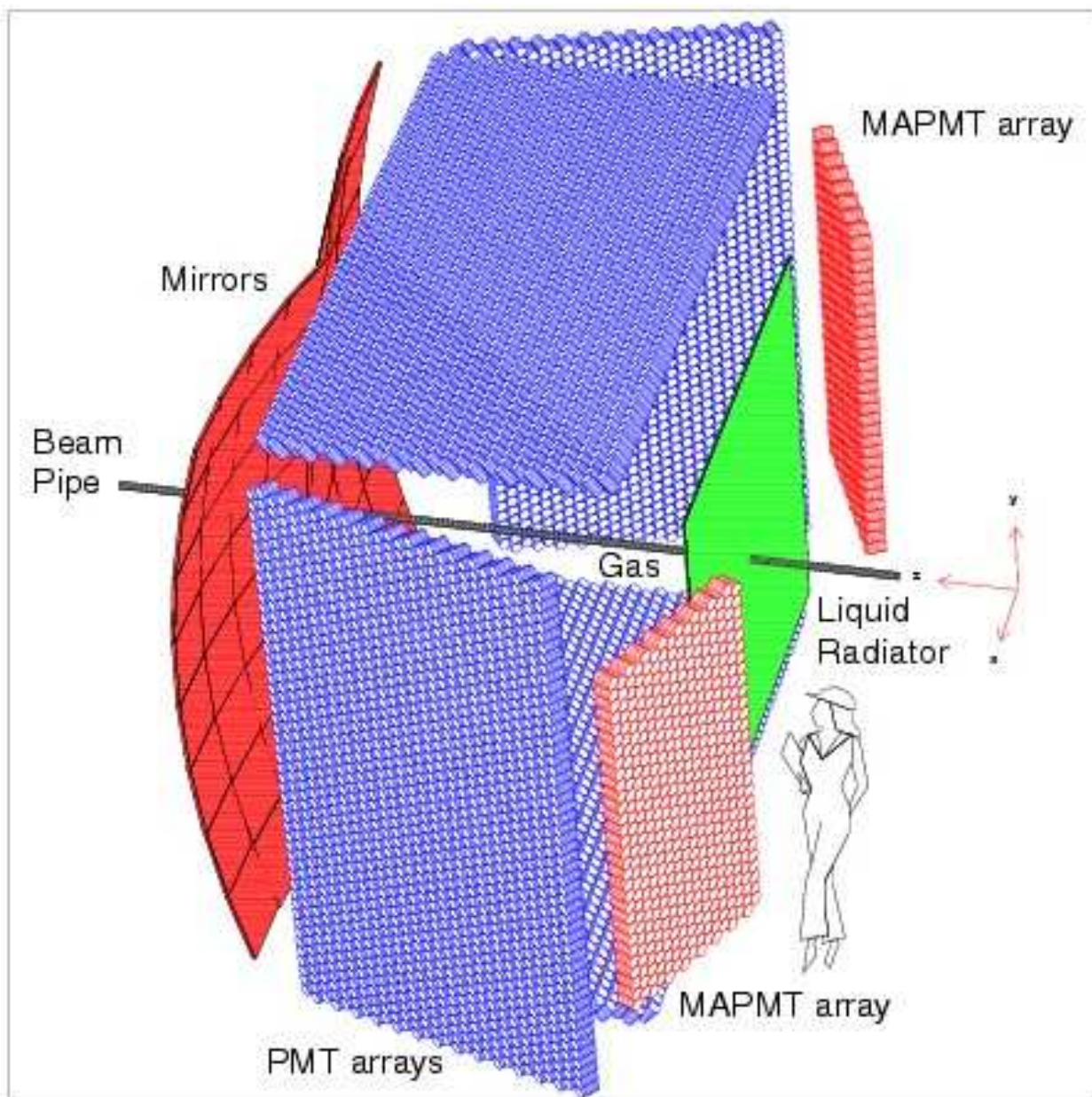


Figure 5.1: Outline of the important RICH components.

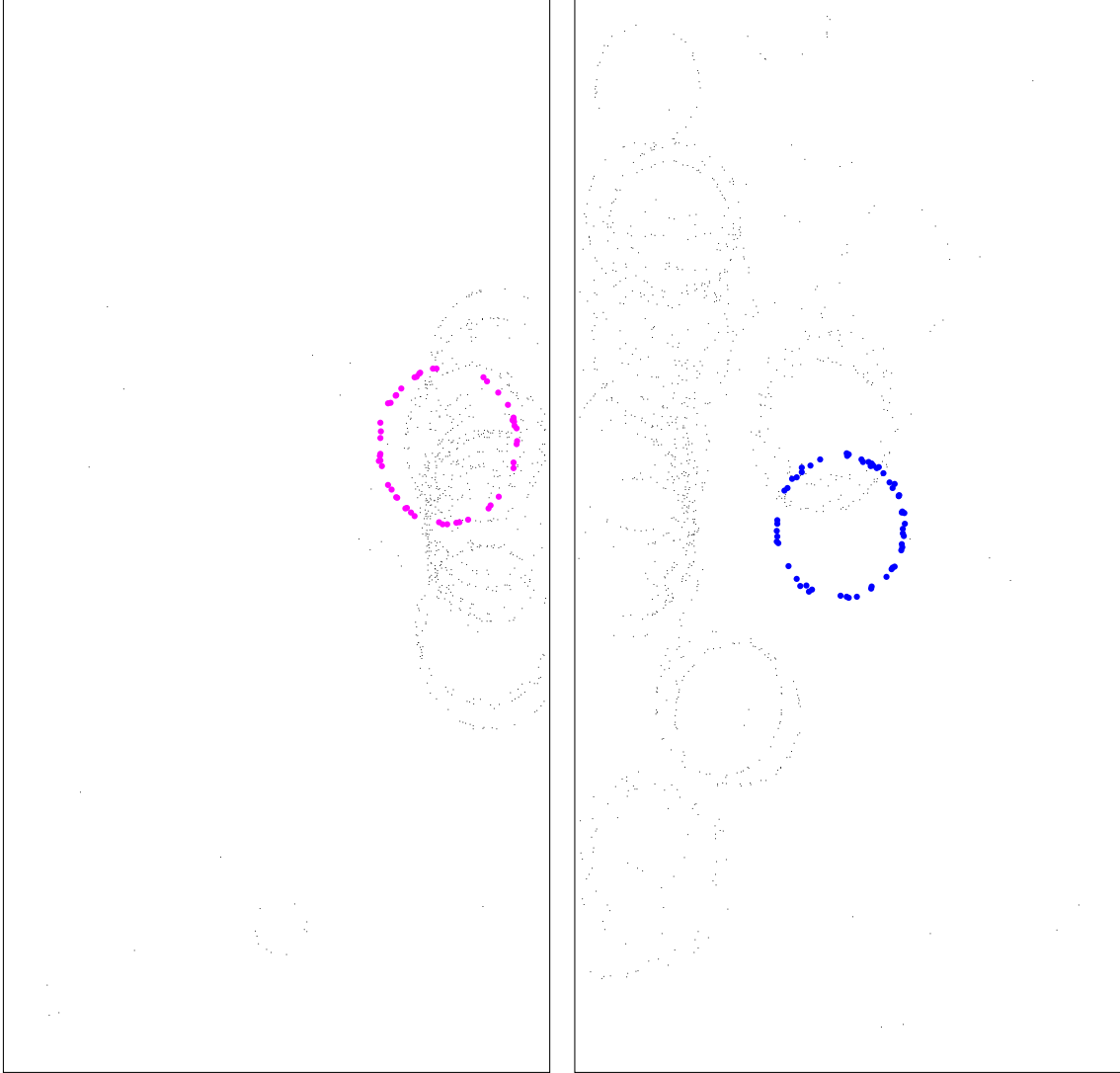


Figure 5.2: Cherenkov rings from the gas radiator detected in the MAPMT arrays as simulated for a  $B \rightarrow \pi^+\pi^-$  event with two minimum bias interactions in the same bunch crossing. The Cherenkov hits for the pions from the  $B$  decay are highlighted.

this gas will therefore provide identical performance to that of the initially simulated  $\text{C}_4\text{F}_{10}$ . The 3M company produces  $\text{C}_4\text{F}_8\text{O}$  and has told us that there are no plans to discontinue its production. We also note that using  $\text{C}_4\text{F}_8$  would only marginally change the physics performance, by reducing the high momentum particle separation between kaons and pions, for example, by  $\sim 1 \text{ GeV}/c$ .

Below  $\sim 9 \text{ GeV}$ , no gas can provide  $K/p$  separation since, for these momenta, both  $K$  and  $p$  are below radiation threshold. In this case, the RICH operates in a threshold mode for ( $K$  or  $p$ ) vs.  $\pi$  separation (except that it has much better noise discrimination than a normal threshold counter because it still measures a Cherenkov ring for pions). Separation of kaons from protons turns out to be important for  $b$ -flavor tagging. In the case of the  $B_s^0$ , we use

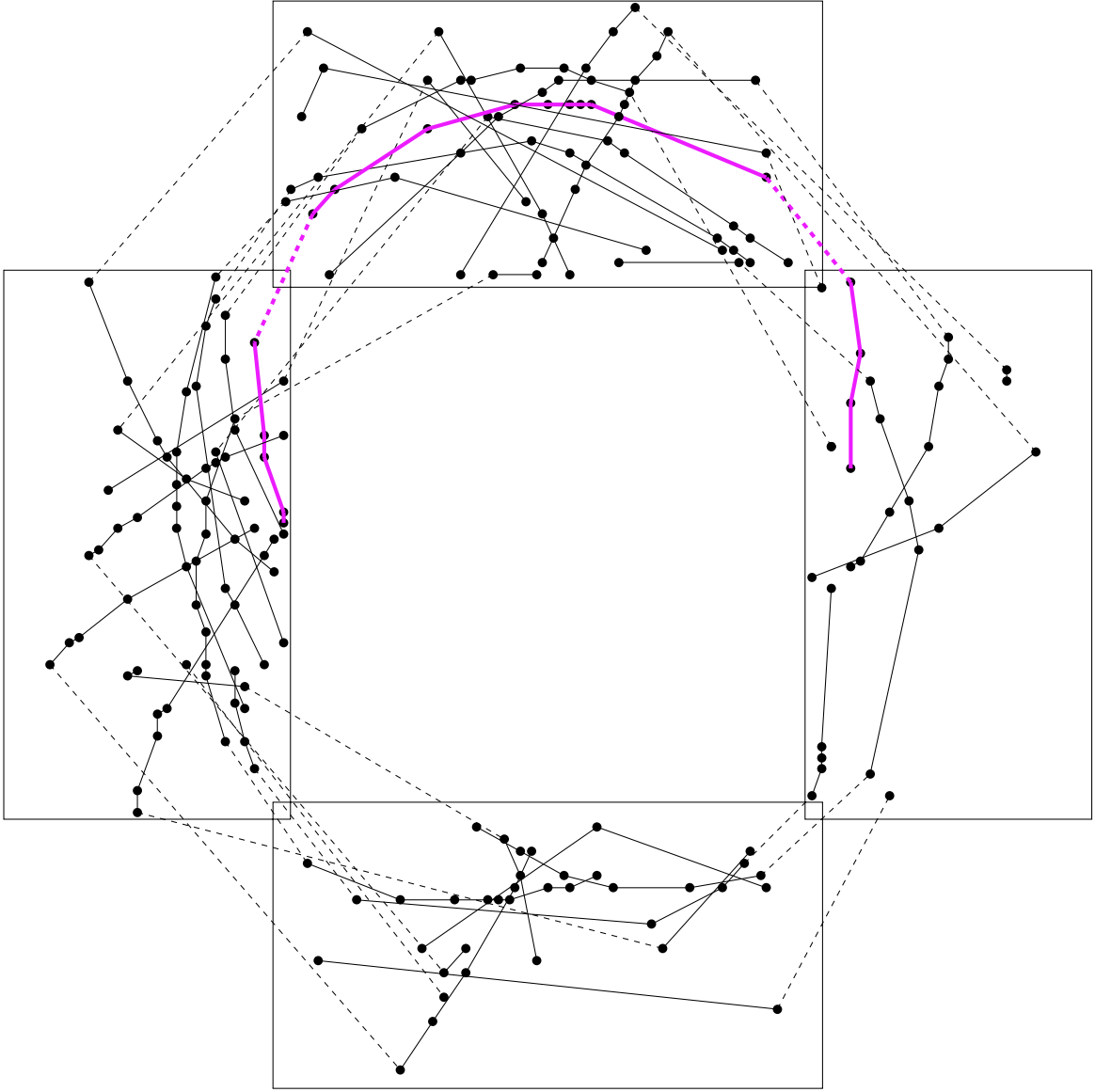


Figure 5.3: Cherenkov rings from the liquid radiator detected in the PMT arrays as simulated for a kaon tagged  $B$  event with two minimum bias interactions in the same bunch crossing. Hits belonging to the same track are connected. The Cherenkov hits for the tagging kaon are connected by a thick line.

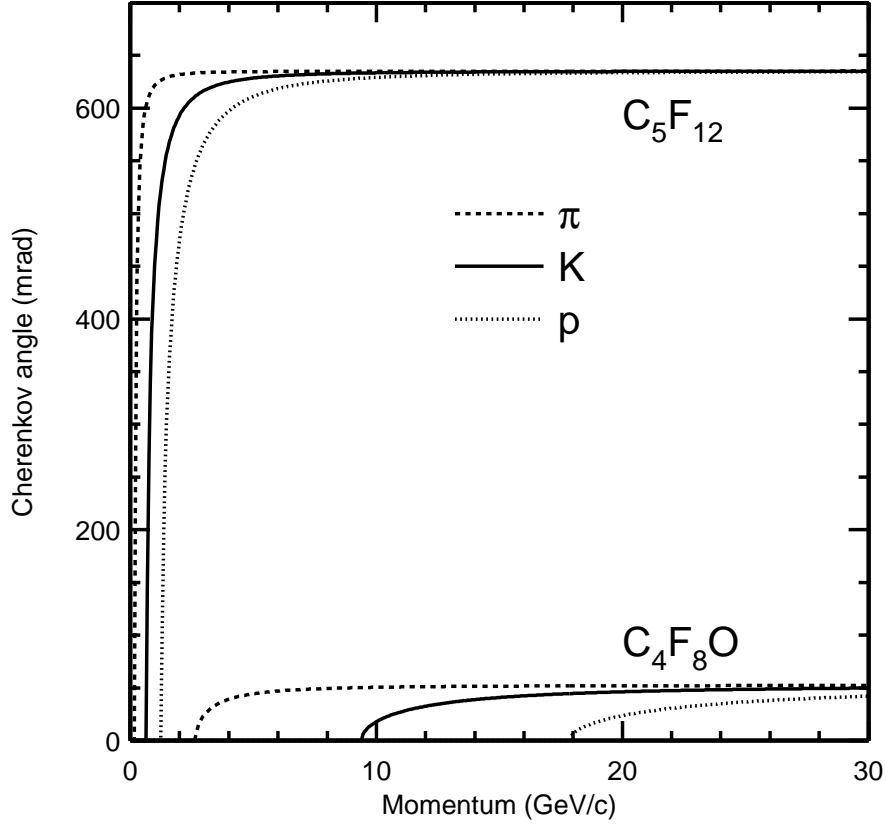


Figure 5.4: Cherenkov angles for various particle species as a function of particle momentum for  $C_4F_8O$  ( $n = 1.00138$ ) and liquid  $C_5F_{12}$  ( $n = 1.24$ ) radiators.

a positively identified kaon for both “same side” and “away-side” tagging. For the  $B_d$ , only the “away-side” case requires kaons. In the “same side” tag, there is a strong correlation between the sign of the fragmentation kaon and the flavor of the  $B_s$ . However, the tagging fragmentation kaon comes from the primary vertex which also contains many protons that can cause false tags. In “away-side” tagging, the lack of  $K/p$  separation prevents one from distinguishing kaons from  $p, \bar{p}$ , which occurs  $\sim 8\%$  of the time in  $B$  meson decays. Decays of  $\Lambda_b$  baryons produce  $p, \bar{p} \sim 50\%$  of the time, but their production rate is suppressed relative to  $B$  meson production. These low momentum protons lead to a reduction in the purity of tagged kaons.

Originally we planned to improve identification of low momentum particles by inserting a thin ( $\sim 4$  cm) piece of aerogel ( $n = 1.03$ ) at the entrance to the gas RICH, as proposed by LHCb [6]. The Cherenkov rings were focused by the mirrors of the RICH and were detected using the same photon detector array (somewhat enlarged) as the gas photons. A study using detailed reconstruction of the Cherenkov rings showed that the relatively low light yield from

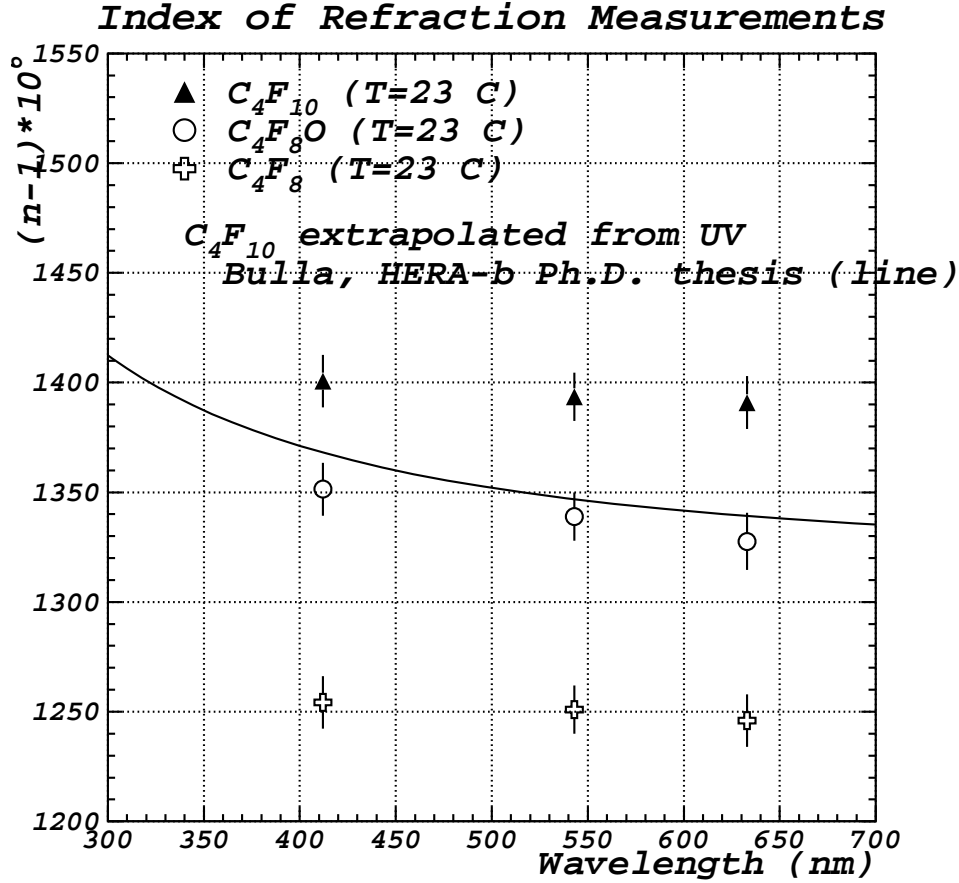


Figure 5.5: Syracuse measurements of refractive indices of various gases as a function of wavelength compared with the curve from HERAb for  $C_4F_{10}$  [5].

the aerogel, combined with confusion from the larger number of overlapping rings from higher momentum tracks radiating in the gas, resulted in very little particle discrimination.

We now plan to use a liquid  $C_5F_{12}$  radiator which has an index of refraction of 1.24 and produces relatively intense, large radius Cherenkov rings, even with only 1 cm of liquid. The  $C_5F_{12}$  radiator has been successfully used in other experiments (e.g., DELPHI). The rings hit the side walls of the RICH gas containment vessel (see Fig. 5.1), which are instrumented with standard 3 inch photomultiplier tubes. Moreover, the small-angle Cherenkov photons produced in the gas radiator almost always intercept the RICH mirror and rarely intercept the side, top, or bottom walls. Thus, the two main limitations of the aerogel scheme, the low amount of Cherenkov light and the confusion between aerogel photons and  $C_4F_8O$  photons, are eliminated. At the same time, the refractive index of  $C_5F_{12}$  is low enough that kaon and proton rings have very different radii, even at 9 GeV, and can be distinguished (Fig. 5.4).

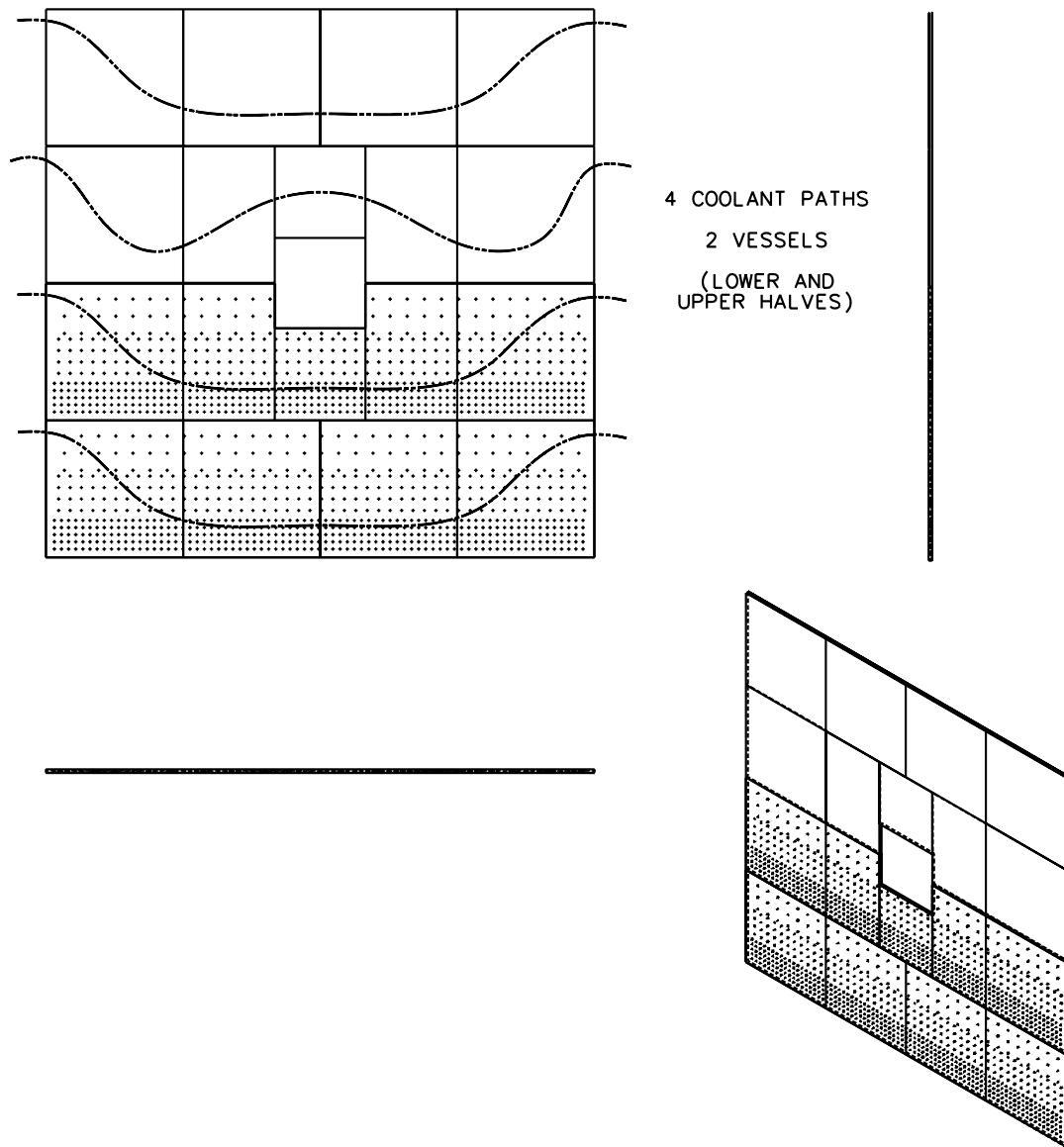


Figure 5.6: Mechanical design of the liquid radiator. The top left figure views the radiator face-on. Side views are also shown. In the figures, the carbon-fiber support posts are only shown on the lower two vessels. The same support scheme will also be used on the upper two vessels.

### 5.3.2 Liquid Radiator

A 1-cm thick liquid radiator will be mounted at the entrance to the RICH vessel. The mechanical design of the liquid radiator is shown in Fig. 5.6. The radiator is about 2.5 m  $\times$  2.5 m in size and will cover the entire RICH entrance window. To suppress unwanted Cherenkov radiation in the liquid by higher momentum tracks, a 40 cm  $\times$  40 cm section of the radiator is removed around the beam pipe. The cut-out helps also the gaseous RICH and ECAL since it reduces a number of photon conversions in the high particle flux area. The liquid is contained in a carbon fiber box with a 3-mm thick quartz exit window. We chose quartz for its radiation hardness. To reduce the static head pressure of the liquid on the window, the radiator is segmented vertically into 4 separate volumes (vessels). There are also a number of reinforcement posts distributed throughout the window, with decreasing spacing towards the bottom of each volume. The total amount of material in the liquid radiator, including its support structure, corresponds to 8.7% of a radiation length.

A liquid re-circulation system is used to provide pure thermally-stable liquid  $C_5F_{12}$  to the four liquid radiator vessels. The total system volume is approximately 20 gallons. A particulate filter, pump, and temperature-regulating heat exchanger are used to circulate and condition the fluid. This single circuit (see Fig. 5.7) services all four vessels. A manifold, however, cannot be used to supply the fluid to the vessels since the increased static head on the lower vessels would exceed the critical breaking stress of the quartz window. Therefore, all vessels are connected in parallel via a switching unit. Also, to prevent any additional stress on the quartz, the chambers are open to atmospheric pressure at both the inlet and outlet. The fluid is collected in a reservoir for recirculation. A PLC-based control system regulates the temperature of the reservoir and the flow-rate of the fluid. Temperature control is necessary to avoid evaporation of the liquid ( $T < 28^\circ\text{C}$ ).

### 5.3.3 Gas Radiator

The gas radiator ( $C_4F_8O$ ) fills the entire tank volume and adds 8% to the radiation thickness of the detector. The average Cherenkov radiation path in the gas is about 2.9 m.

The front and rear windows of the tank are made of carbon fiber; 0.05 inches thick at the front (0.6% r.l.) and 0.04 inches thick at the rear (0.5% r.l.). The seal around the beam-pipe is achieved using a polyurethane bellows and a flange for each window (Fig. 5.8).

The radiator gas circulation system is used to provide pure  $C_4F_8O$  gas to the RICH vessel. The total system volume is approximately 2,000 cubic feet. A simplified flow diagram of the system is shown in Fig. 5.9. The major components of the system are a metal bellows pump, a molecular sieve to remove water vapor and particulates, a parallel purification arm to remove nitrogen, oxygen and other gases, and a passive expansion volume to compensate for external atmospheric pressure changes. The purification arm may be switched in as needed, and contains a compression pump that condenses the  $C_4F_8O$  gas to approximately 3 atmospheres. The impurity gases that do not condense are vented through a relief valve which is set at a pressure just above the condensation pressure of  $C_4F_8O$ . The pure liquified  $C_4F_8O$  is then vaporized and re-enters the system through a regulator valve set just below



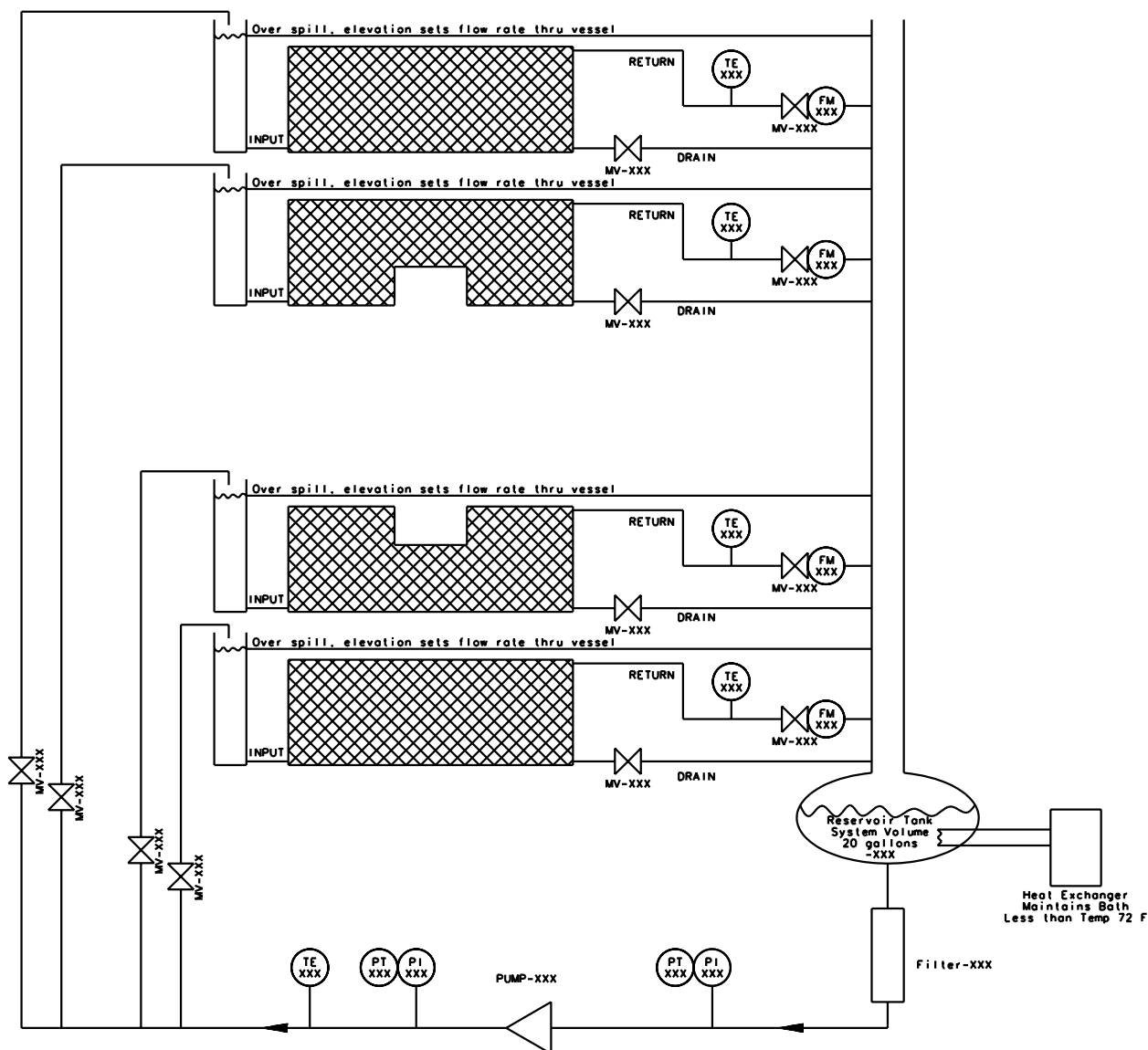


Figure 5.7: Simplified flow diagram of the  $C_5F_{12}$  liquid recirculation system for the RICH.

the gases critical condensation pressure. A PLC-based control system regulates the pumping speeds to maintain an internal vessel pressure equal to atmospheric pressure. The expansion volume is designed to be about 10% of the total gas volume. The concern is that even a small differential between the interior and atmospheric pressures will cause large deflections and stresses in the entrance and exit windows for this heavy gas. Space constraints near the windows prohibit large deflections. A monitoring system will record temperatures and pressures.

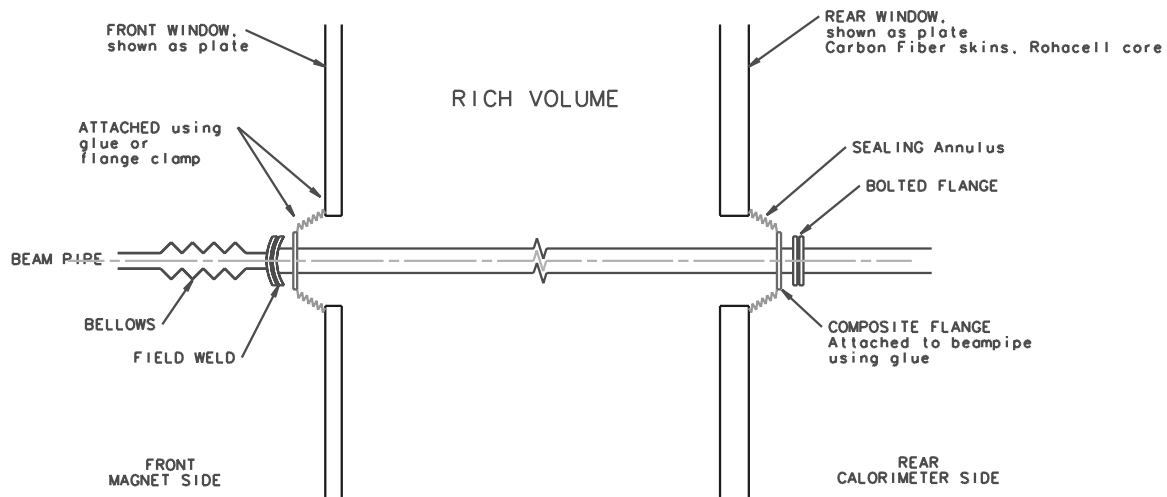


Figure 5.8: Beam-pipe to window seal at the front and rear of the RICH.

### 5.3.4 Mirrors

Spherical mirrors at the end of the gas volume reflect Cherenkov photons radiated in the  $C_4F_8O$  and focus them into rings at the photodetection surface. The mirrors are tilted allowing the photodetectors to be out of the spectrometer acceptance and to be shielded by the magnet. Since the geometric aberrations due to the mirror tilt are significant for the gas radiator, we plan on the longest RICH detector we can accommodate within the space limitations. This also maximizes the photon yield from the gaseous radiator, again improving the resolution of the device.

This mirror system consists of two large mirrors each with a mean radius of  $R_{mean} = 697$  cm, and an aperture of 220 cm x 440 cm. They can be broken down to any number of tiles and shapes to optimize cost and performance. A hole (probably circular in shape) of 3 cm radius is needed in the center of the mirror system to allow the beam pipe to go through, as shown in Fig. 5.10.

Because of the high precision  $PbWO_4$  calorimeter just behind the RICH, we require that the radiation length of the mirror system is less than 2% at normal incidence. This can easily be satisfied if composite mirrors are used.

For performance and cost reasons, it is more practical to handle smaller mirror tiles. Therefore, we divided each of the two big mirrors into arrays of full and half hexagons for an initial design. One possible design is shown in Fig. 5.10. It would consist of 19 full hexagons (64.2 cm side-to-side), 4 half hexagons and 7 hexagons missing one edge-triangle. Once these mirror tiles are produced by the vendor and tested at Syracuse, we will ship them to Fermilab where they will be assembled.

Subsequently we approached different vendors with these preliminary designs. The CMA company of Tuscon, Az has proposed using larger square tiles that has several nice features for us. There design is shown in Fig. 5.11.

In this design there are only 16 mirror for the entire system leading to a much easier task

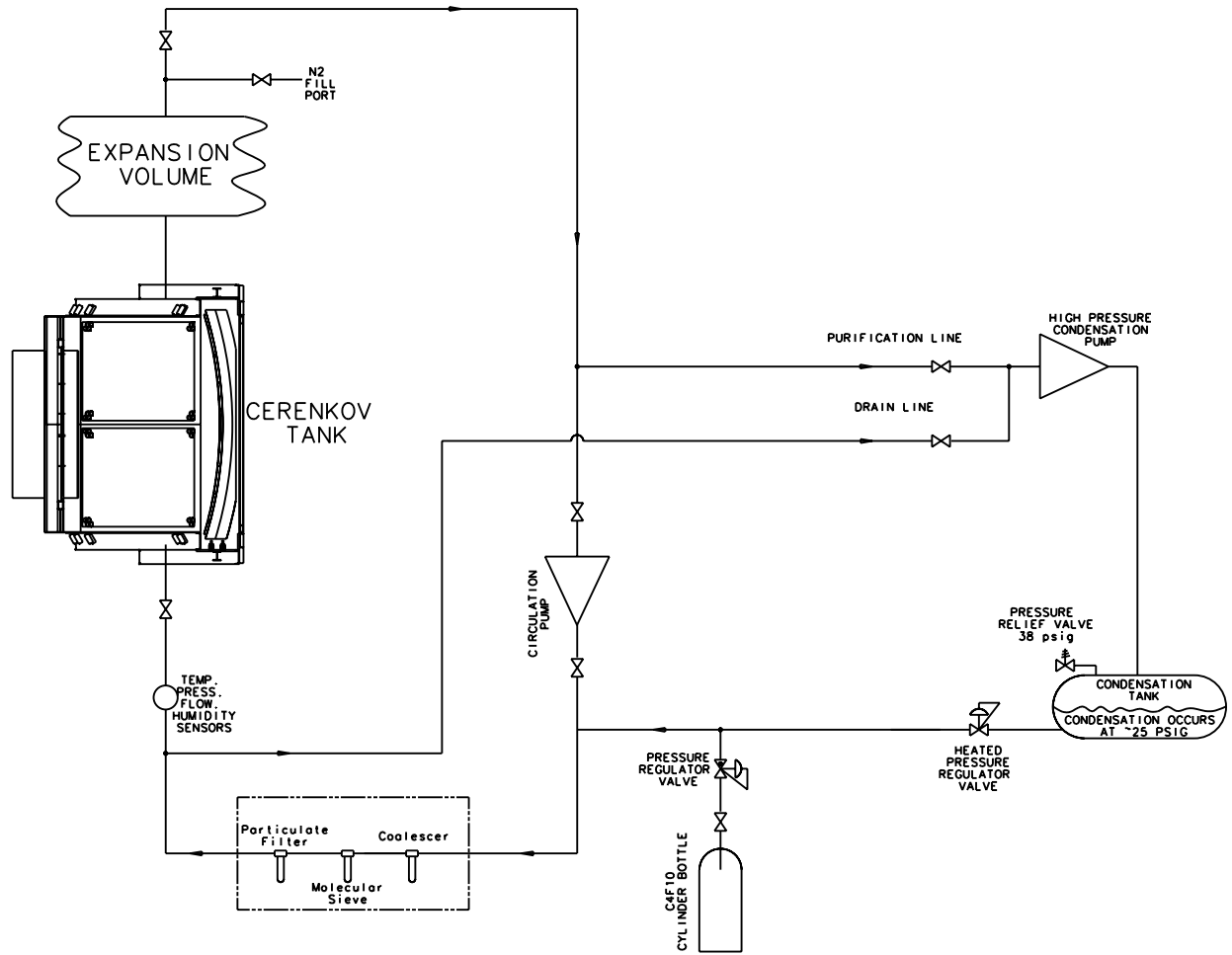


Figure 5.9: Simplified flow diagram of the  $C_4F_8O$  gas recirculation system for the RICH.

of assembling and aligning the segments. These mirrors are made from composite materials and have a thickness  $< 2\%$  r.l. [7].

The mirror support structure, which is integrated with the rear window, is shown in Fig. 5.12. Each mirror tile is supported by a 3-point kinematic mount attached to a large flat support panel, which is made of two carbon fiber skins of each 0.51 mm thick containing between them 7.62 cm of foam. The total radiation length is 2.6%. The size of the support panel is 447 cm x 447 cm made in four strips, one for each vertical column of mirrors. The panels have 48 circular holes with a diameter of 10.16 cm, from which we extend carbon fiber cylinders to the mirror mounts for easy access. These cylinders are attached to bellows which are themselves attached to the rear window. The deflections are computed to be  $\sim 0.4$  mm when the tank is filled with gas.

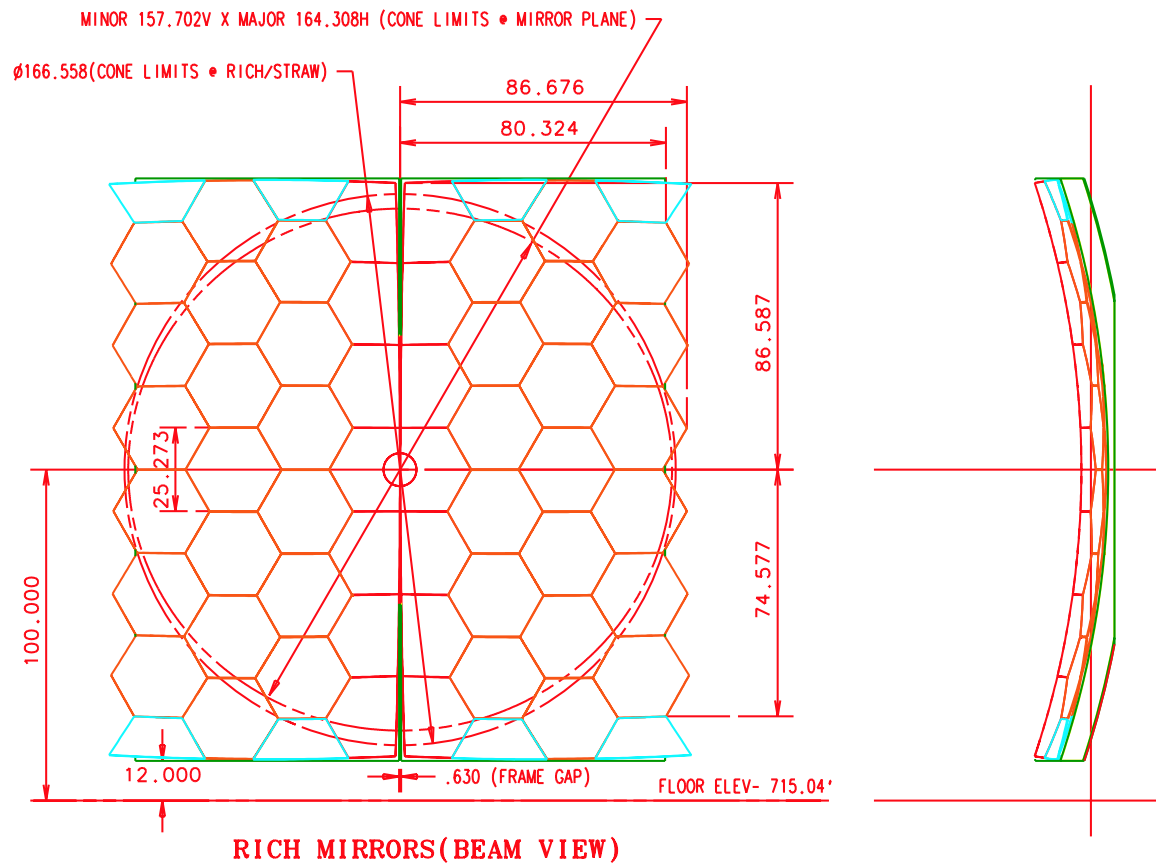


Figure 5.10: The original RICH mirror system (units are in inches).

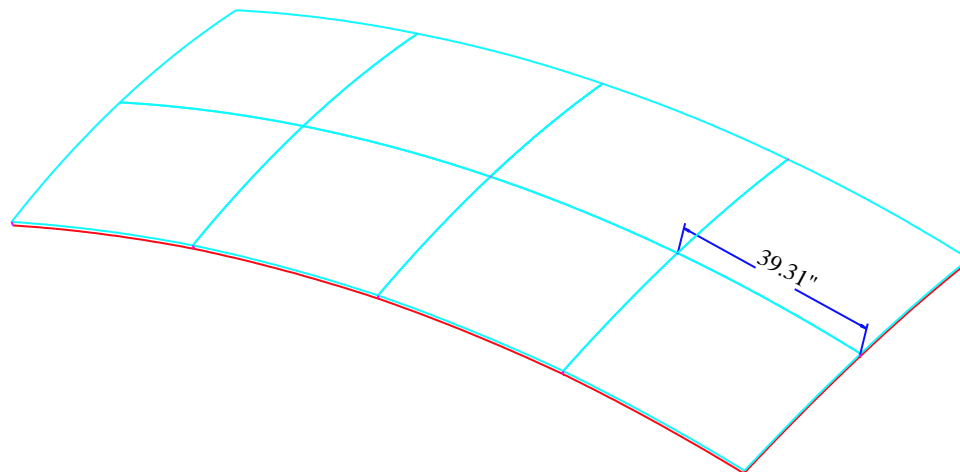


Figure 5.11: Sketch of one-half of the CMA proposed mirror array (units are in inches).

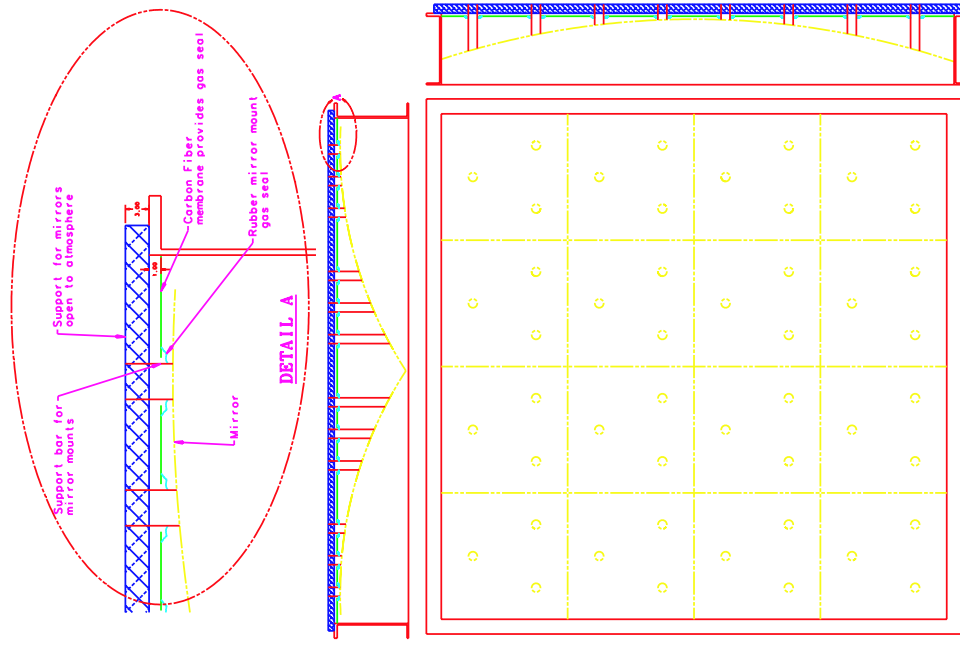


Figure 5.12: Drawing of the mechanical support for the CMA mirrors.

### 5.3.5 Photodetector Planes and Tank Structure

The size, optimal position and orientation of the photodetection surface for the  $C_4F_8O$  Cherenkov photons were determined using a ray tracing Monte Carlo. Even though the true focal plane of a spherical mirror is not planar, non-planar surfaces do not improve the resolution significantly and are difficult to realize in practice. We therefore use a flat photodetector plane whose position and tilt (442 mrad) was optimized using simulation. Since the actual emission point along the track for Cherenkov photons is unknown, the Cherenkov angle reconstruction assumes emission at mid-point of the RICH vessel. The emission point error, which contributes to Cherenkov angle resolution, is magnified by the mirror tilt from 0.2 mrad to 0.53 mrad. This error imposed by geometrical considerations sets the scale for the other two major contributions to the Cherenkov angle resolution: chromatic error and photodetector segmentation error (called also photon position error) to be discussed in Section 5.3.6.1.

The photons generated in the liquid radiator ( $C_5F_{12}$ ) pass through the quartz window and enter the  $C_4F_8O$  gas volume. Most of the photons reach the sides of the RICH gas containment box. The sides, top, and bottom of the box are instrumented with arrays of 3" diameter photomultipliers to detect these photons. The tilt of the PMTs is also determined by simulation.

The photodetectors for each system (MAPMT or HPD for gas system, and PMT for liquid system) are each shielded using a mu-metal tube to minimize the impact of the main dipole's fringe field on the performance of the tubes. Additional external shielding of the

magnetic field will be needed for the MAPMTs (or HPDs) and is provided by the steel-walled enclosure. The major detector elements (front and back windows, liquid radiator, mirrors and photodetector boxes) will be attached to the tank superstructure, which consists of massive beams (see Fig. 5.13), which will also support the tank walls and acrylic windows which seal the gas volume in front of the photodetectors. The superstructure is segmented to decouple mechanical loads due to the different components.

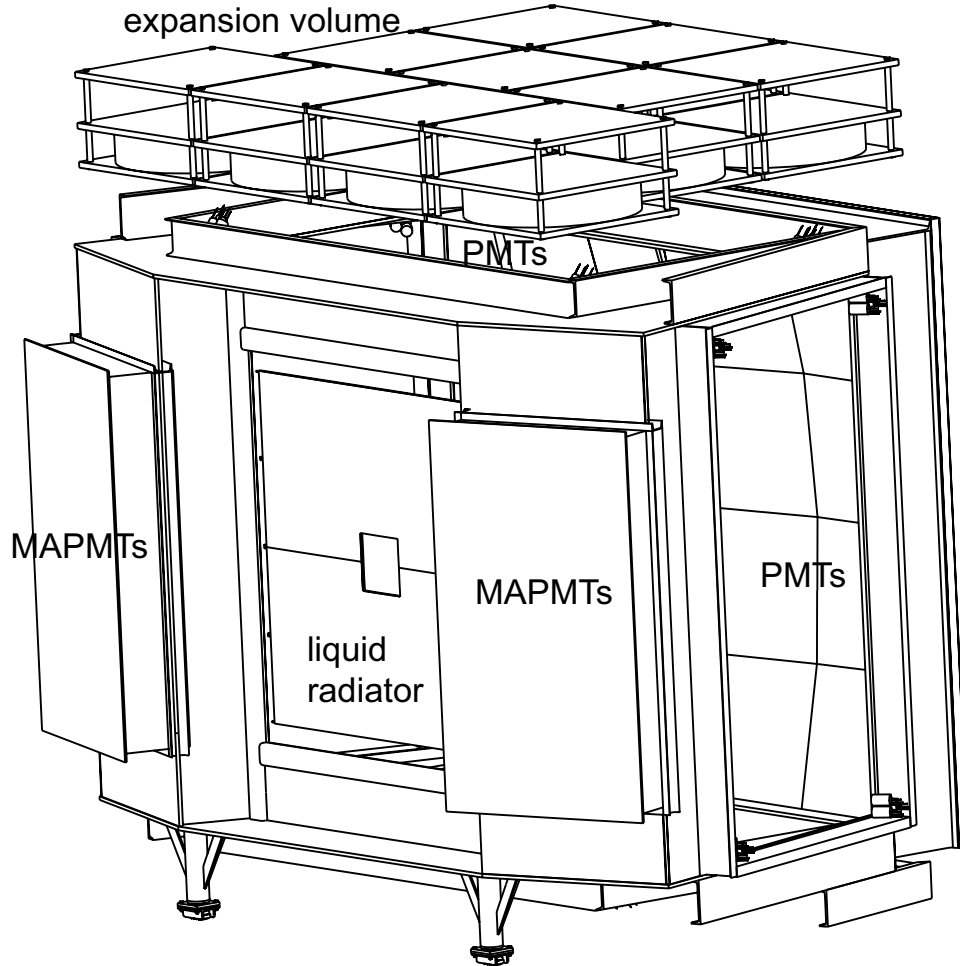


Figure 5.13: Tank support beams and location of the major components. The PMTs arrays are not shown except for their locations.

### 5.3.6 Photodetectors for the $C_4F_8O$ radiator

We choose to work in the visible wavelength region above 280 nm to minimize chromatic aberrations that arise because the index of refraction varies with wavelength. Because of the open geometry of the forward spectrometer and the availability of space to install shielding to

protect detection elements from the fringe field of the BTeV analysis magnet, arrays of multi-anode photomultipliers (MAPMT) or hybrid photo-diodes (HPD) can be used. Currently the MAPMTs are the baseline solution with the HPDs being a viable alternative.

### 5.3.6.1 MAPMT Photodetectors

Mult-Anode Photo-Multiplier Tubes are the baseline choice for the photon detector of the gas radiator system. In a MAPMT, the dynode structure is transversely segmented creating many independent channels within a single PMT enclosure. The initial R5900 multi-anode tubes developed by Hamamatsu were 30 mm  $\times$  30 mm in cross-section and were segmented into four (R5900-M4), sixteen (R5900-M16) or sixty-four (R5900-M64) separate anodes. The main drawback of these tubes was a large dead area around the photocathode. The active area of these tubes was only about 36%. Some type of light focusing system in front of the PMTs was needed to recover the dead area. The R5900-M16 and R5900-M4 tubes were used in the HERA-B RICH detector [2]. The HERA-B system used a two-lens system providing a demagnification by a factor of two. In the HERA-B solution the tubes are not closely packed, reducing the cost of the detector but allowing the segmentation error to dominate the achievable resolution. Furthermore, the photon yield is reduced due to reflective losses at each lens surface. The LHCb group, which is considering MAPMTs as a back-up system for their own version of PP0380 HPDs<sup>1</sup>, developed a different demagnification system consisting of a single convex-plano lens [6] to work with a closely packed array of R7600-M64 tubes. These tubes are 26 mm  $\times$  26 mm in cross-section, as the outer flange was eliminated increasing the active area to about 48%. The light recovery factor by the lens is 1.55 [12], resulting in an effective active area of 74%. Our initial modeling of the MAPMT system consisting of closely packed R7600-M16 tubes with convex-plano lenses showed somewhat worse performance than HPDs [13].

Hamamatsu has recently developed a new multi-anode tube - R8900. The focusing of the photo-electrons onto the first dynode was redesigned to provide a much larger active area of 85% in a 26 mm  $\times$  26 mm form-factor. Consequently, no lens system is needed. Moreover, the square geometry minimizes the geometrical losses, except for a possible magnetic shield. In bench studies, we have determined that the R8900 tubes can be adequately shielded from the fringe fields of the BTeV dipole magnet (see Section 5.4.1) using a 250  $\mu$ m thick mu-metal shield. We have simulated a system of MAPMTs assuming a 1 mm gap between tubes and find a geometrical acceptance of 79% (compared to 62% for the HPDs). The quantum efficiency of MAPMTs is likely to be at least 15% higher than for HPDs since photo-cathode quality is easier to control over the small area. While photo-electron collection efficiency is very high for HPDs, about 1/3 of the photo-electrons are expected to be lost in R8900 tubes, failing to multiply on the first dynode. Putting the geometrical, quantum and collection efficiencies together we expect to obtain about the same photon yield from both the MAPMT and HPD systems (see Tables 5.1 and 5.6). The R8900-M16, with 6 mm  $\times$  6

---

<sup>1</sup>Finer pixels and faster readout are required in LHCb, thus the readout electronics had to be integrated with the diode chip.

Table 5.1: Expected performance of BTeV RICH system. The photon yield and the resolution per track given here do not take into account any reconstruction losses due to overlap of Cherenkov rings from different tracks in the same event. The gaseous RICH performance given here corresponds to the baseline option (MAPMTs). The HPD solution produces very similar numbers (see Table 5.6).

|                        | $C_4F_8O$ , $n = 1.00138$ | $C_5F_{12}$ , $n = 1.24$ |
|------------------------|---------------------------|--------------------------|
| emission point error   | 0.50 mrad                 | 0.4 mrad                 |
| segmentation           | 0.51 mrad                 | 5.3 mrad                 |
| chromatic error        | 0.49 mrad                 | 3.7 mrad                 |
| total error per photon | 0.83 mrad                 | 6.2 mrad                 |
| number of photons      | 52                        | 12.4                     |
| total error per track  | 0.11 mrad                 | 1.8 mrad                 |

mm anode pixels (Fig. 5.14), has the right segmentation for our application producing the segmentation error which is well matched to the emission point and the chromatic errors (see Table 5.1). The tubes are equipped with a standard bialkali photocathode on a borosilicate glass window. A UVT acrylic will be used to separate the gas and the MAPMT volumes. Wavelength coverage of the borosilicate glass and of the UVT acrylic are very similar (see Fig. 5.43). Since MAPMTs require a single  $\sim 1$  kV voltage to operate and provide a gain of  $10^6$ , the technical aspects of the readout and HV distribution are much easier to manage than for the HPDs. The current price of R8900 tubes is lower per unit area than that of the PP0380AT HPDs from DEP (described in Section 5.3.6.4). Therefore, the MAPMT system is used for the baseline design and the HPD system is maintained as a viable alternative.

A system with 9016 MAPMTs approaches the full geometrical coverage limit. With 16 pixels per tube, the detector would have 144,256 electronic channels.

The first two R8900-M16 prototypes have been tested at Syracuse (see Section 5.4.1), and we have received 52 more tubes that are undergoing tests and will be used in the test beam in Summer 2004. The test beam box we have designed is capable of accommodating either an MAPMT array or HPD array, and both will be tested at that time.

### 5.3.6.2 MAPMT Readout Electronics

To minimize development cost and error, MAPMT readout is closely related to the HPD readout electronics, which is described in Sec. 5.3.6.5. Since a single photoelectron produces as many as 1,000,000 electrons in the MAPMT (vs. 5,000 in the HPD), gain of the VA\_BTEV chip originally developed for the HPD (see Sec. 5.3.6.5) is reduced and noise requirements are less stringent. Design of the digital part is shared with the HPD hybrid. The MAPMT tubes will plug into a mating board, which will contain HV divider and connectors to the MAPMT hybrid board. Unlike for the HPD option, no flex-rigid technology is required making the



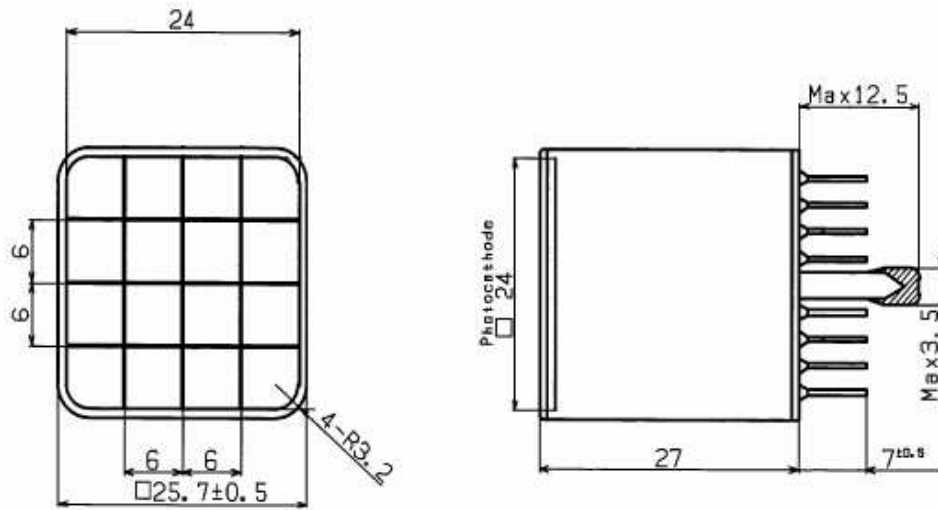


Figure 5.14: Dimensions of the prototype R8900-M16 MAPMT from Hamamatsu.

MAPMT hybrid board cheaper and more reliable. The layout of the first prototype MAPMT VA\_BTeV front-end hybrid is shown in Fig. 5.15. One hybrid has 2 VA\_BTeV chips and serves 8 MAPMTs (128 channels).

The first MAPMTs hybrids were recently tested at Syracuse and performed very well. More MAPMT hybrids will be soon characterized and later used in the Summer 2004 test beam.

### 5.3.6.3 MAPMT Mechanical Support

The mounting arrangement for the MAPMTs is sketched in Fig. 5.16. Conceptually the detector plane is segmented vertically into groups four tubes high. The tubes are plugged into circuit boards containing the bases that are attached to a box channel beam which runs across the entire width of the detector. The MAPMTs are cabled to hybrid boards attached to box channel via standoffs. Each hybrid has 128 channels and is cabled to 8 tubes. The hybrids then go to a multiplexer board as shown. The box channels which provide the mechanical strength are screwed in at the ends to a rigid frame. Cooling lines are attached to the box channel.

### 5.3.6.4 HPD Photodetectors

HPDs are commercially available from DEP (Delft Electronic Products B.V.) in the Netherlands. For BTeV, we have collaborated with them in developing a 163-channel HPD with an outer diameter of 81 mm (PP0380 tube, see Fig. 5.17) The active diameter of the HPD is about 74 mm. A photon entering this device is focused by a spherical quartz window onto a photocathode deposited on the inner surface of the window. Photoelectrons are then



Figure 5.15: Photograph of the first MAPMT hybrid board. Compare with the HPD hybrid board shown in Figs. 5.19-5.20.

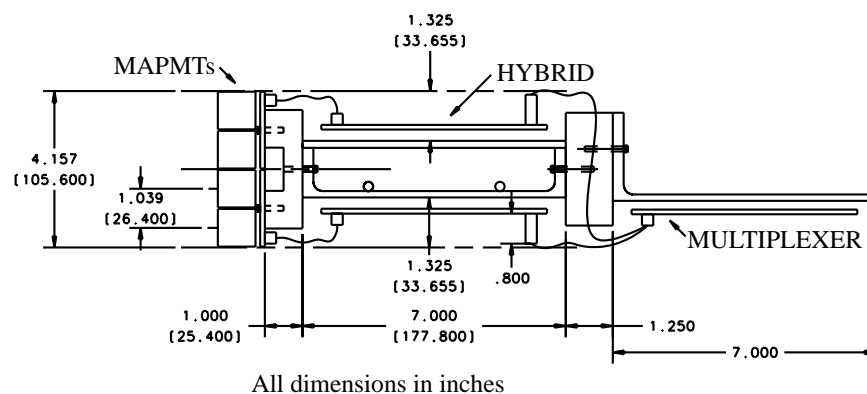


Figure 5.16: Drawing of prototype mounting scheme of MAPMTs.

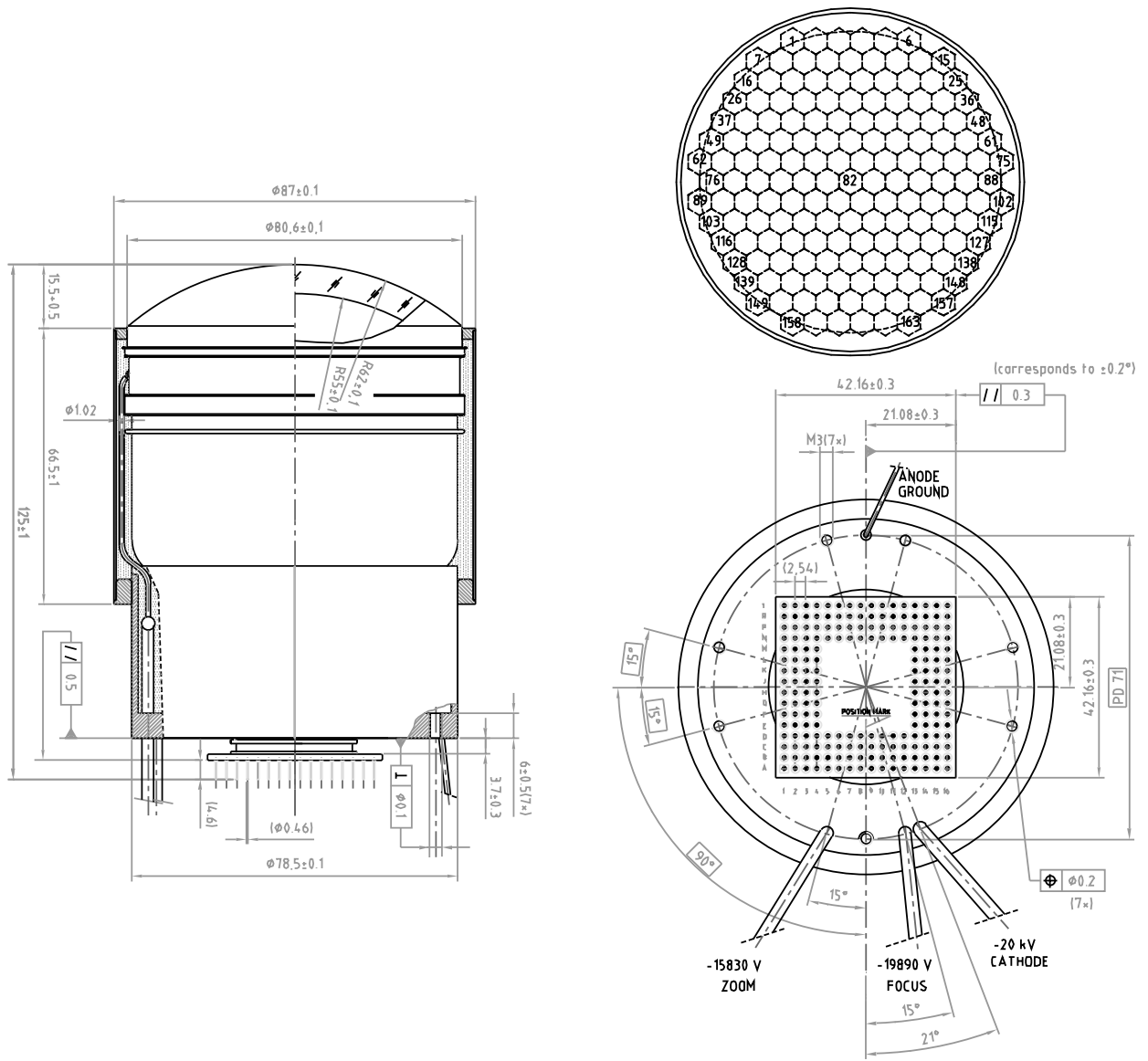


Figure 5.17: BTeV HPD (DEP PP0380AT). The outer dimensions are outlined on the left. The bare tube diameter is 83 mm. The insulated tube diameter is 87 mm. Silicon pixels (163 channels) on the cathode are shown in the upper right drawing. Pin layout is illustrated in the lower right picture.

accelerated by  $-20$  kV through a drift region with electrostatic focusing onto a segmented silicon diode where they produce a signal of  $\approx 5000$  electrons. In addition to  $-20$  kV, the HPD requires voltages of  $-19.89$  kV and  $-15.83$  kV for focusing and demagnification onto the silicon pixel array. The charge collection time from the silicon depends on the bias voltage and is well below 100 ns. The focusing used in the PP0380 HPDs was developed by DEP in collaboration with the LHCb group [8]. The segmentation of the diode array into pixels has been adjusted to match our spatial resolution requirements. The effective pixel size at the HPD front-face is 5.7 mm side-to-side, corresponding to a photon position error of 0.45

mrad, which is slightly smaller than the 0.53 mrad contribution from the emission point uncertainty. A 163 pin-grid array connects the pixel elements to readout electronics residing outside the tube.

About 80% of the bare tube area is active. However, the HPDs require 2 mm thick insulation and 2 mm thick magnetic shields which add to the inactive area. Closely-packed tubes cover 91% of the area they occupy. Thus the overall geometrical light collection efficiency is  $\sim 62\%$ .

The last major factor impacting the RICH performance is the wavelength coverage, which is determined by the photo-cathode and window material. The wavelength sensitivity determines chromatic error and is a major factor in the number of Cherenkov photons detected per track. Quartz windows are a standard feature in the HPD tubes as they can easily sustain the high voltage on the photo-cathode. High quality quartz extends the wavelength coverage from the visible range down to 160 nm. Such a large wavelength coverage results in a large chromatic error of 1.4 mrad per photon and in a large number of detected photons per track ( $\sim 162$ ). When the wavelength coverage is limited, the photon yield drops but the chromatic error per photon improves. These two effects offset each other. The simulations show that a shallow optimum in Cherenkov resolution per track is reached when the wavelengths are limited to about 280 nm. UVT acrylic used in the vessel window will produce such a wavelength cut-off. This results in a chromatic error of 0.50 mrad per photon with a photon yield of  $\sim 50$  photons per track. The total intrinsic Cherenkov angle resolution is therefore 0.84 mrad per photon and 0.11 mrad per track, which is comparable to the MAPMT performance (see Table 5.6). A system with 944 HPDs approaches the full geometrical coverage limit. With 163 pixels per tube, the detector would have 153,872 electronic channels.

We have received 15 BTeV-HPDs that are being extensively tested [9]. They will be used in our Summer 2004 test beam run.

### 5.3.6.5 HPD Readout Electronics

A single photoelectron, when accelerated through 20 kV, produces a signal of about 5000 electrons in silicon. In collaboration with IDE AS Norway, we have developed low noise electronics to operate with the HPD. The Syracuse group previously worked with this company on development of a custom-made ASIC called VA\_RICH and its associated front-end hybrid boards that were used in reading out the CLEO-III RICH detector. The pulse-height spectrum for the PP0380AT HPD obtained with VA\_RICH electronics is shown in Fig. 5.18. Peaks due to one, two, and three photo-electrons are easily seen.

In BTeV, the RICH readout will be binary. The readout must also be much faster than with VA\_RICH. Therefore, a different adaptation of the VA chip family has been produced for the BTeV HPD. We refer to this new ASIC as VA\_BTeV. The VA\_BTeV chip comprises 64 processing channels, including an analog section, a comparator and a digital section. The analog section consists of a RC-CR preamplifier-shaper unit with gain tuned to the low expected signal. It has a fast peaking time of 72 ns that is substantially shorter than the Tevatron bunch crossing time of 396 ns. The fall time is 200 ns, so the process signal is

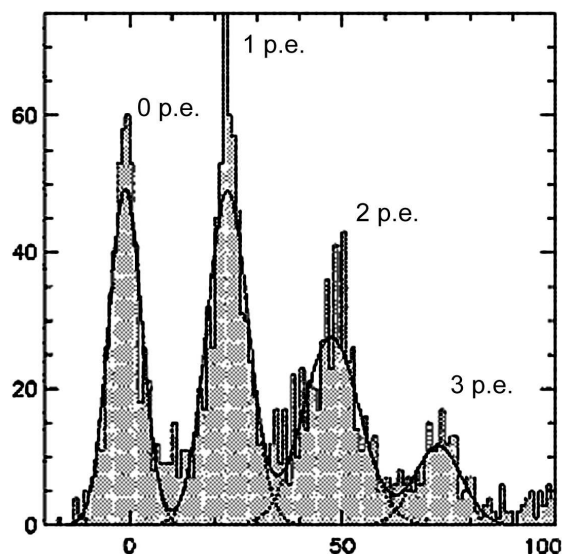


Figure 5.18: Pulse-height spectrum obtained for a single channel of the BTeV HPD with VA\_RICH readout. The pedestal peak is positioned at zero. The subsequent peaks corresponds to one, two and three detected photo-electrons. The peaks are separated by  $\sim 5000 e^-$ .

completely finished by the time of the next bunch crossing. If the Tevatron were to go to 132 ns crossing time there would be a small loss of hits due to the low overall occupancy. An optional gain stage that can be switched off is included to enable it to operate at slightly higher thresholds. The chip architecture features parallel input and parallel output for fastest delivery of the output information. Since each chip has 64 channels, a front-end board will house three ASICs. They will be connected to the HPD output pins via a small mating board. This analog part of the front-end hybrid will be well-isolated from the digital part for the best signal to noise performance. Binary signals for each channel are fed in parallel into the digital part housing an FPGA, which serializes the output, encodes the channel address and attaches a time stamp.

The layout of the first prototype VA\_BTeV front-end hybrid is shown in Fig. 5.19. The first prototypes were tested on a bench using the DAQ system which will be used in the RICH test beam. Satisfactory noise performance was obtained. The next iteration of the design features a flex circuit to make a right angle bend between the analog part (mounted directly on the HPD end) and the digital part to allow for closely packed arrays of HPDs. A number of improvements to the hybrid design have also been implemented (see Fig. 5.20). A batch of 16 hybrids have been procured and detailed tests are currently underway at Syracuse. These boards will be used for the test beam run in Summer 2004.

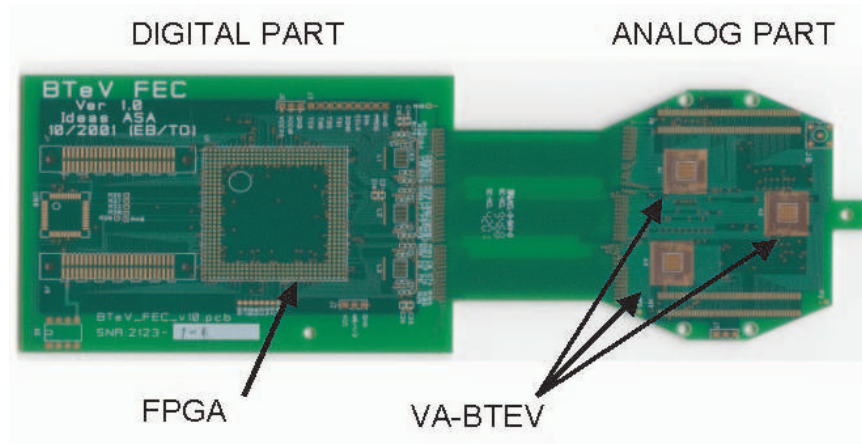


Figure 5.19: Layout of the first prototype of the BTeV RICH front-end hybrid board.

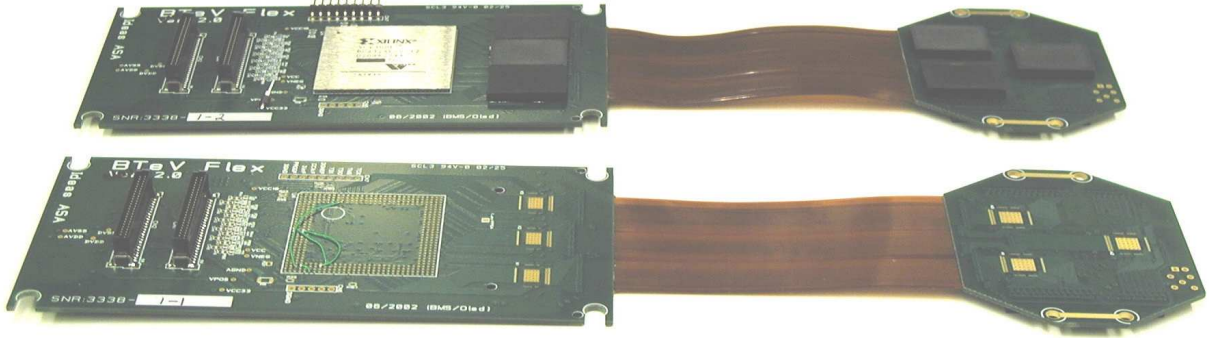


Figure 5.20: Photograph of the new flex hybrid board which will be used to read out an HPD.

#### 5.3.6.6 HPD Mechanical Support

The mechanical support of the HPDs and their electronics is illustrated in Fig. 5.21. Each tube is supported on three mounting rods screwed into the HPD back flange. The mounting rods for six HPDs, together with the support frame for their readout electronics create a single mechanical unit, called a “hexad”, which can slide in and out of the mu-metal tubes. This allows modular replacement, as well as testing, of the HPDs. The mating board with a ZIF socket attaches to the HPD pins. The analog part of the front-end hybrid plugs into the mating board with the help of connectors. The flex part of the front-end board creates a 90 degree angle. The digital part of the front-end electronics rests on one of the support plates.

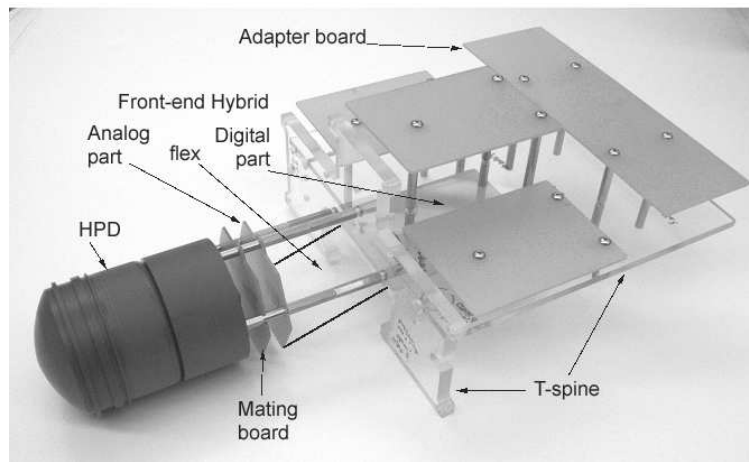
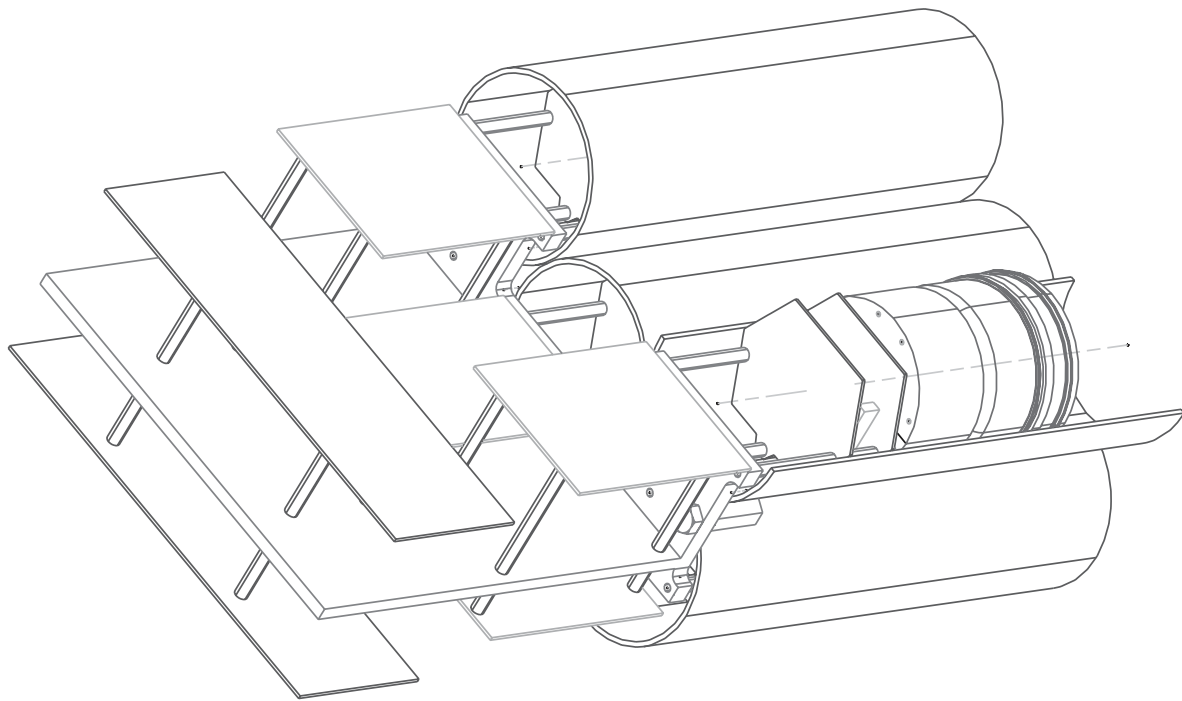


Figure 5.21: Mechanical support of HPDs and their electronics. Drawing of one mechanical unit(“hexad”) with 6 HPDs inserted into magnetic shielding tubes is shown in the upper part. Photograph of a mechanical mockup of such unit is shown in the lower part.

### 5.3.7 Photodetectors for the $C_5F_{12}$ Liquid Radiator

Cherenkov photons generated in the 1 cm thick liquid radiator pass through the quartz window, undergoing refraction at the liquid-quartz and quartz-gas interfaces, and travel at large angles towards the PMT arrays. The PMTs are tilted to match the average angle of incidence of the radiated photons. The Cherenkov images at the PMTs are not simple rings since they are distorted by light refraction at the interfaces of the various media and by the orientation of the RICH's walls. The chromatic error for  $C_5F_{12}$  is 3.7 mrad per photon. The emission point error is negligible. The photon position error is determined by the size of the photomultiplier tube. Three inch PMTs produce a photon position contribution to the Cherenkov angle resolution of 5.3 mrad. The total error is then 6.2 mrad. Two inch PMTs improve the resolution by about 20%, however they approximately double number of tubes and cost of the PMT array. The current design has about 5000 3" PMTs covering the most illuminated portions of the two RICH side walls, as well as the top and bottom walls. While most of these tubes will be equipped with a borosilicate glass window, 500 PMTs located in radiation hot-spots (see Sec. 5.4.5) will have UV glass windows for increased radiation hardness. With this system, we expect to detect 12.4 photoelectrons/track, resulting in a per-track resolution of 1.76 mrad (see Table 5.1). Since at 9 GeV/c, kaon and proton Cherenkov angles differ by 5.34 mrad, the separation would be about 3 standard deviations. Separation improves substantially for lower momentum tracks.

Several manufacturers produce 3" tubes which satisfy our requirements. Further details on these tubes are discussed in Section 5.4.4.

### 5.3.8 Power Supplies

The MAPMTs require a 1 kV power supply. We plan to use the same power supply as adopted for the pixel detector (CAEN A 152N). The same power supplies can be also used for the PMTs in the liquid radiator RICH subsystem.

The power supply system for the backup HPD option is more complicated, since it requires much higher voltages (-20 kV, -19.89 kV and -15.8 kV). Because of the low level signal from the HPDs ( $\sim 5000 e^-$ ), it is very sensitive to any noise on its high voltage lines. We plan to use three separate power supplies, instead of using a voltage divider. Groups of tubes will be ganged together to reduce the number of power supplies. The peak-to-peak ripple on each supply is required to be less than 10 mV. On a test bench, we have used a power supply from Acopian with a  $\sim 1$  V p-p ripple combined with a HV RC filter close to the tube. Noise studies were performed with VA\_RICH readout electronics (see Sec. 5.4.2.8) and the performance was found to be satisfactory. This extra filtering close to the detector may not be practical due to limited space near/in the HPD enclosure. Furthermore, the stored energy in the 20 kV capacitors may be a safety concern.

We have also acquired 3 Matsusada power supplies (PS), each capable of delivering up to 30 kV with a p-p ripple of  $\sim 5$  mV. These PS are currently being used in bench tests of the HPD (using VA\_BTeV electronics). Their noise performance is excellent. They require a control and monitoring system to set the high voltage and to monitor the high voltage and



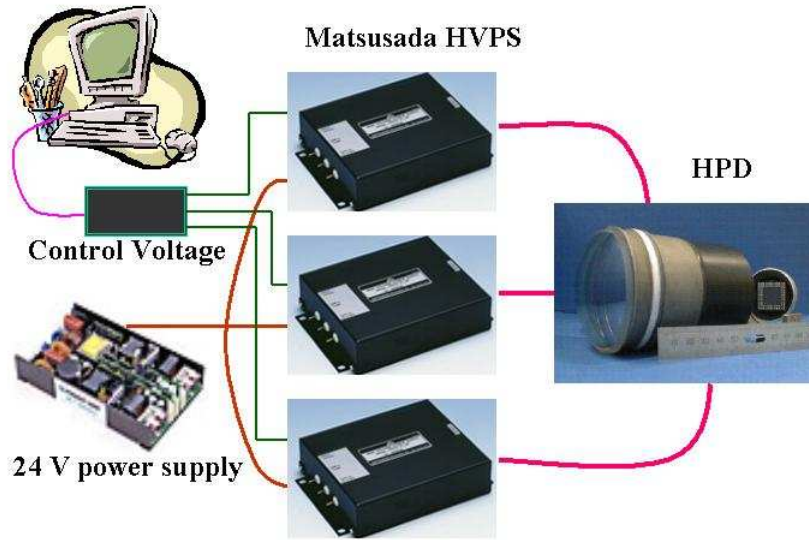


Figure 5.22: Block diagram of the HPD high voltage distribution system.

the current output. The HV control system is shown schematically in Fig. 5.22. A prototype system with remote control through Labview has been developed and is being used in bench tests of the HPD system.

Other options which are being explored includes the acquisition of a CAEN SY1527 universal HV mainframe and a CAEN SY3527 HV supply to be used with the MAPMT sensor configuration. This will give us the opportunity to experiment with the CAEN HV supplies and control software which are considered a candidate for the integrated implementation of the high voltage distribution system for BTeV.

Finally, we are planning to acquire a Wiener low-ripple low voltage supply to benchmark the low voltage implementation in our system. In addition to the three high voltage supplies, the HPD also needs a power supply of  $\sim 60$  V to bias the silicon pixels.

All high voltages (20 kV and 1-2 kV) and low voltages ( $\sim 60$  V) will be controlled by setting the voltage of an individual channel or group of channels. Each channel will provide power to a group of HPDs or MAPMTs. The power supply grounds are floating and defined locally at the detectors that are being powered.

The applied voltages and current draws are monitored for every channel by the RICH monitoring system. Ranges of acceptable values for each power supply will be determined. Voltages or currents which fall outside the prescribed range will send a warning/alarm to the fast control system (*i.e.*, a PLC) and the slow control system (such as iFix).

### 5.3.9 Monitoring

The windows and container vessel of liquid and gas radiator can be broken or deformed if the proper pressure is not maintained. The monitoring system will watch the temperatures

and pressures at various points in the gas and liquid volume. Depending on the condition, a fast response can be provided by a PLC, or a warning provided by the slow control system. Other properties that will be monitored include: the purity of gas and liquid which could also affect the index of refraction, the temperature of each front end electronics hybrid, and the humidity inside and outside the MAPMT enclosure.

The critical sensors will be watched by a commercial PLC, and will provide a fail-safe shutdown in extreme cases and an alarm or warning in other non-critical cases. All monitored sensors will also be interfaced to the slow control system (iFix) which also can produce alarms, historical data collection and retrieval, and graphical displays. Fermilab has a great deal of experience with iFix, which is being used throughout the lab for slow controls.

## 5.4 Completed R & D

In this section, we discuss the R&D progress on the various RICH detector components.

### 5.4.1 Development of MAPMT System for the Gas Radiator

Multi-anode PMTs provide an excellent technology for detection of Cherenkov photons with fine segmentation in visible wavelengths. We have recently received prototypes of the 4×4 segmented tube, the R8900-M16, and have studied various features of these redesigned tubes (see Section 5.3.6.1). An outline of the tube is shown in Fig. 5.14. Particular attention was directed toward studying the most important features of the device, namely, the pulse height spectra from individual channels, the effective area, and the magnetic field sensitivity. These aspects were studied by illuminating the MAPMT using a pulsed LED source connected to an optical fiber. The optical fiber was a single-mode fiber which produced a spot size of  $\approx 100 \mu m$  on the face of the MAPMT. The test setup allowed us to look at the pulse height spectrum from individual channels as well as the integrated number of counts above a set threshold. Signal distributions were obtained by taking the difference between readings with light on and off. A photograph of the test setup is shown in Fig. 5.23.

A preliminary design of the MAPMT mounting system has just been finished and a prototype is being made for the test beam box. The support is rather simple having the tubes plug into sockets mounted on circuit boards and supported by a box channel running the length of the array.

#### 5.4.1.1 Pulse Height Spectra

For each channel, we measured the pulse height spectrum using the system described above. The pulse height distribution (in ADC counts) for each of the 16 channels in one tube is shown in Fig. 5.24. We find the distributions to exhibit well defined single photon peaks. The variation in gain from channel to channel is of order  $\pm 20\%$ , which is acceptable, since we are only interested in whether the channel had a hit or not (binary readout).

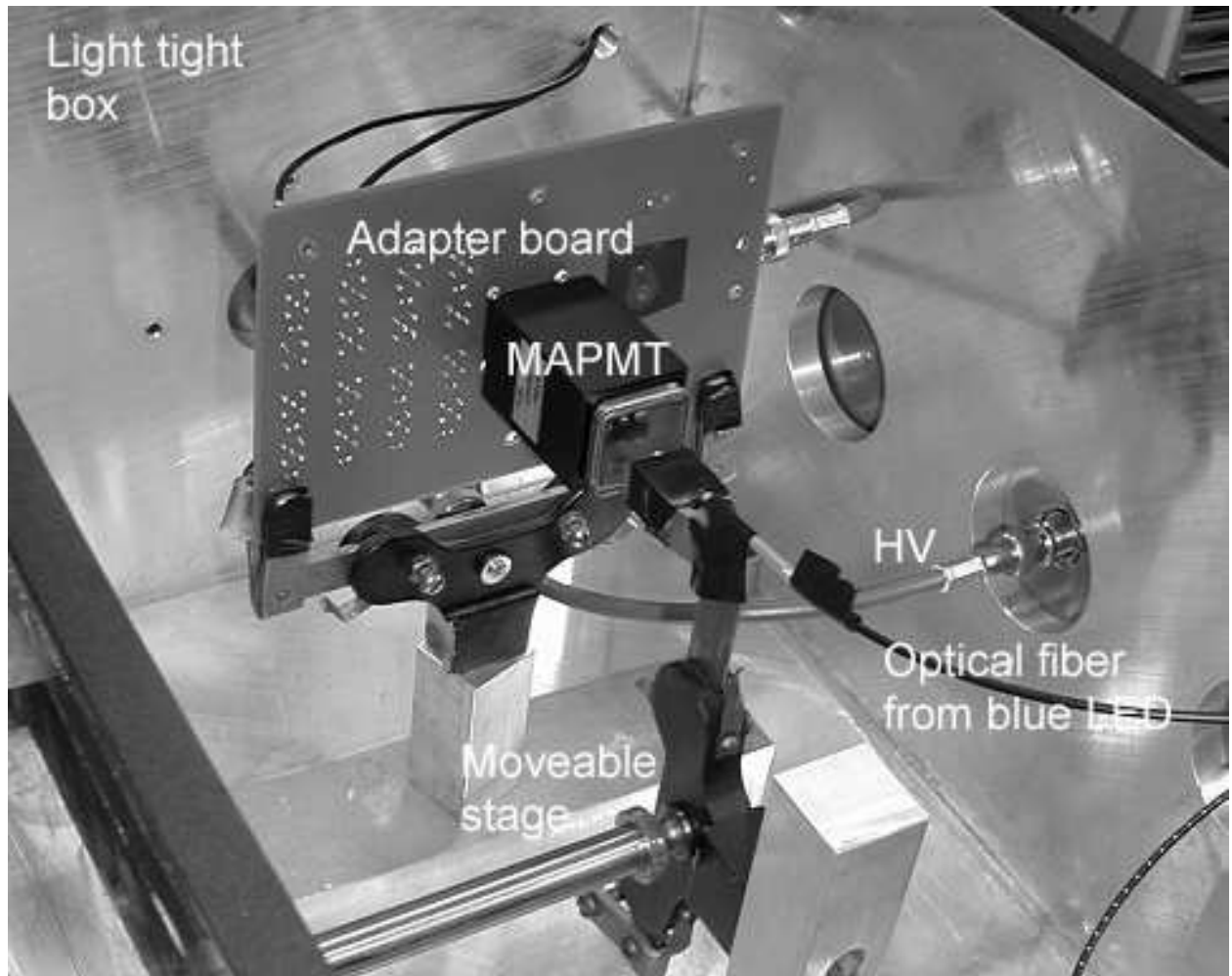


Figure 5.23: Photograph of the MAPMT test set-up at Syracuse. The prototype R8900-M16 tube from Hamamatsu is illuminated here by blue LED light which is delivered by a single-mode optical fiber. The optical fiber is mounted on a movable stage.

#### 5.4.1.2 Active Area Measurement

For this measurement, we scanned the face of the MAPMT in steps of  $\approx 300 \mu\text{m}$ . We scanned through the center of the rows and columns, going beyond the end of the physical device in order to measure the drop-off in active area at the periphery of the tube. Figure 5.25 shows the results of the scan across the four columns. In each of the four plots, we show the total signal count (solid curve) and the contributions from the individual cells (dashed) in each column. The cell numbers are provided at the top of each figure. Several observations are made from these data.

- The relative response is roughly flat across the face of the tube

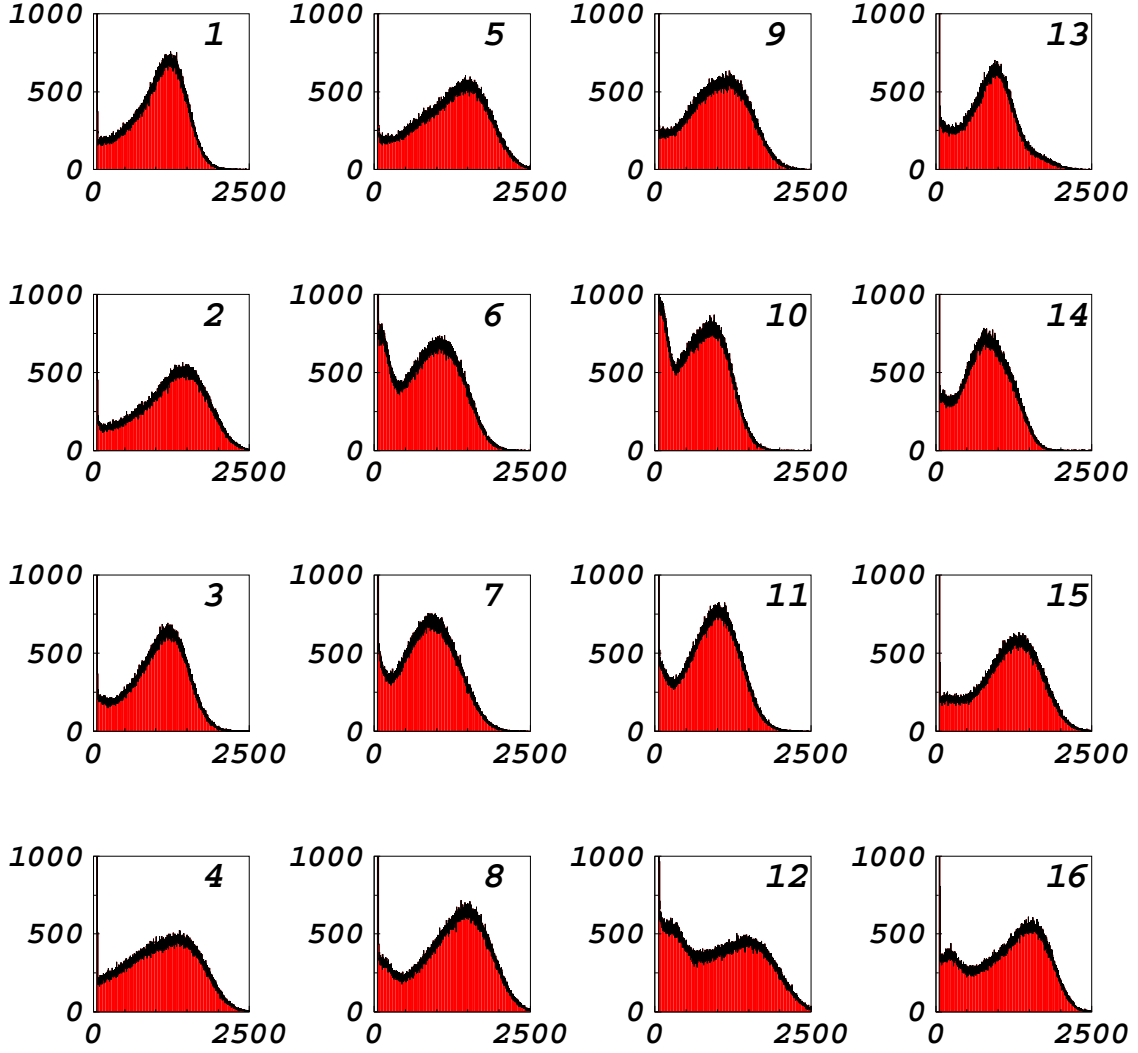


Figure 5.24: Pulse height distributions for the 16 channels of one of the prototype R8900-M16 MAPMTs. The number inset in each plot is the MAPMT channel number. The layout on this page is the same as viewing the tube head-on.

- There efficiency near the edges of the tubes begins to falloff at approximately 1.5 mm from the physical edge.
- The effective area of a cell has Gaussian-like tails which extend beyond the physical dimension of the cell. This *broadening* of the cells effective active region was one of the tradeoffs in achieving a larger total active area for the MAPMT.

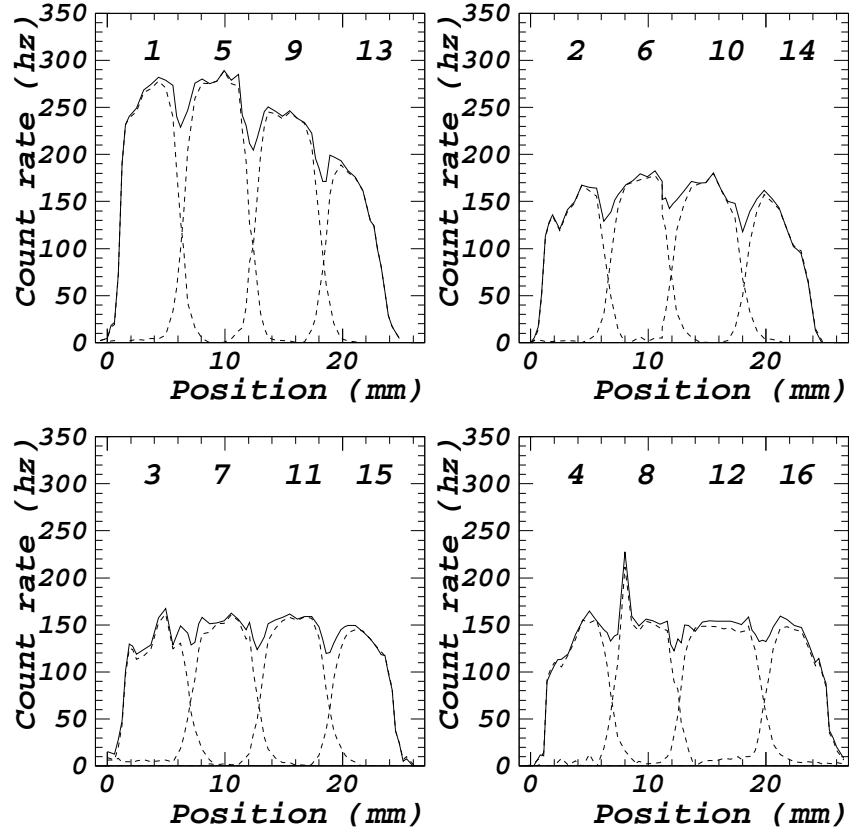


Figure 5.25: Scan along the four columns of the MAPMT using a blue LED and an optical fiber. Shown are the background-subtracted count rates as a function of position for each cell along columns (dashed), and the sum of all four cells (solid).

In Fig. 5.25, it is observed that cells 1, 5 and 9 have a higher relative response than the other three columns. Because this study was primarily concerned with measuring the active area, the thresholds were not tuned to account for gain differences between channels. We have also studied in detail the falloff of efficiency in the corners of the MAPMT, and find that the falloff begins about 2 mm from the corner along the diagonal. The test performed here on this device, as well as on a second MAPMT, suggest that Hamamatsu has indeed been

successful in producing a MAPMT with large active area. Using these data, and defining the width as the point at which the efficiency drops off by 50%, we find that  $\approx 22.5$ -23 mm of the maximum 24 mm is active. A detailed simulation of a photon detector consisting of MAPMTs has been carried out. The details of the simulation are discussed in Section 5.7.1.2.

#### 5.4.1.3 Magnetic Field Studies

Another important aspect of the tube is its resistance to magnetic fields. The photon detectors will be located just outside the main dipole analysis magnet where a non-negligible fringe field exists. The photon detectors will be in an iron/mu-metal box which is required to reduce the magnetic field inside the box to a maximum of 10 Gauss. Since it is difficult to predict the direction of the field inside the box, we require that the photon detectors do not suffer a significant loss of efficiency in either a longitudinal or transverse magnetic field of 10 Gauss.

To test the performance of the tube, we placed the MAPMT in a solenoidal magnetic field such that field was aligned either in the longitudinal or transverse direction with respect to the direction of the dynode chain. The performance of the tube was first studied without a shield, and then with a 250  $\mu\text{m}$  thick mu-metal shield extending a distance  $d$  beyond the edge of the tube. In the transverse field configuration, we found that the metal casing of the MAPMT provided sufficient attenuation of the field (loss in average efficiency less than 5%). On the other hand, the longitudinal field ( $B_{LONG}$ ) produced a significant loss in collection efficiency and thus the MAPMT must be shielded. To effectively shield the longitudinal component of the field, we found that the shield must extend about 1 cm beyond the front face of the MAPMT. In Fig. 5.26 we show the collection efficiency as a function of the applied longitudinal field. The vertical axis has been normalized to the response at  $B_{LONG}=0$ . We show the effect on three of the four corner channels (ch#1, #13, and #16), one edge channel (ch #3) and one center channel (ch#10). The corner channels are observed to be more sensitive to longitudinal fields than the other channels. In fact, we observe that for some of the channels, the relative collection efficiency actually improves, whereas for one of the corner channels (ch#13) the collection efficiency is degraded by  $\approx 20\%$  with respect to  $B_{LONG}=0$ . We have confirmed that indeed ch#13 was the worst channel in this geometrical configuration. If the tube is rotated by  $90^\circ$  (about the  $B_{LONG}$  direction), the worst channel becomes a different corner channel, but the magnitude of the efficiency loss is about the same for the “new” worst channel. Averaging over all 16 channels, we find that the net loss in efficiency is  $<5\%$ , for the case where the full field is longitudinal, which is unlikely to be the case. If part of the field is transverse, the average loss in collection efficiency is lower.

#### 5.4.1.4 MAPMT Electronics

We have been working with IDE AS to produce a modified version of the VA.BTeV chip/hybrid which will accommodate the MAPMT signal of  $\sim 10^6$  electrons. The chip is required to have a large dynamic range ( $10^5$  -  $10^7$  electrons). A 2-chip hybrid with a new analog front end tuned to the expected MAPMT signal has been produced and delivered to

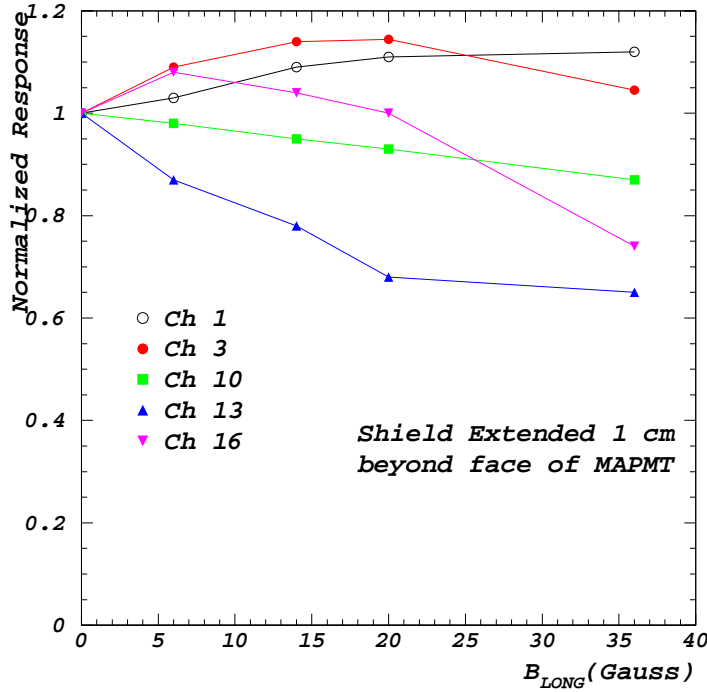


Figure 5.26: Relative collection efficiency for a prototype R8900-M16 MAPMT as a function of the applied longitudinal magnetic field. The vertical axis is normalized to the value at  $B_{LONG}=0$ .

Syracuse. It has been tested and works well. An additional benefit of this modified chip is that in addition to the normal digital channels, there is a dummy channel with an analog output. This aids in the testing of this readout chip. These hybrids will be used in the Summer 2004 test beam run.

#### 5.4.2 Development of HPD System for the Gas Radiator

Hybrid Photo-Diodes provide a competitive technology to the MAPMTs for detection of Cherenkov photons with fine segmentation. We have developed a 163-channel HPD together with DEP which meets our specifications on position resolution. A picture of this redesigned HPD is shown in Fig. 5.17. Two initial tubes of this type were manufactured by DEP and successfully tested at Syracuse. We have also recently received 15 additional tubes which will be used in the 2004 testbeam run. The pulse-height spectrum for one of the HPD channels, obtained with low intensity LED light and VA\_RICH readout electronics (adopted from the CLEO III RICH) is shown in Fig. 5.18. Peaks due to one, two, and three photoelectrons reaching the same pixel within the integration time are observed, demonstrating good single

photoelectron detection capability (in RICH operations we will detect one photoelectron at a time). A number of other baseline tests have been performed and are discussed below.

#### **5.4.2.1 Measurements of the Active Area**

An important parameter of the HPD is the active area of the tube, as presented to the incident Cherenkov radiation. The active area of the HPD has been measured, by scanning a collimated light source across the diameter of the HPD using a linear motion stage. The LED light source had a beam spot of 1 mm diameter at the HPD window, and was pulsed to produce an average of one photoelectron during the integration time of the electronics. The mean number of photoelectrons was determined as a function of radius. An active area diameter of 74 mm was obtained, consistent with the DEP specs of a 72 mm photocathode deposition and the expected refraction through the spherical quartz window.

#### **5.4.2.2 Measurements on the Electrostatic Focusing**

As discussed previously, the HPD electrostatically focuses photoelectrons produced in the photocathode onto a pixelated silicon detector. Measurements were made to determine the best electrostatic focus of the HPD. Using a collimated LED light source, the position and RMS of the spot was determined as a function of the three voltages, UK (cathode), UF (focus), and UZ (zoom). The results were consistent with electrostatic simulations made by DEP, for the optimum high voltage setting. Of practical importance, it was found that the focus has a weak dependence on the values of UK and UZ, but a strong dependence on UF. Consequently, the value of UF should be set to nominal within 10 V (i.e., 0.05%).

#### **5.4.2.3 Relative Quantum Efficiency**

The previous tests also yield a measurement of the efficiency of the HPD across the tube face. This is a relative measurement, referenced to the quantum efficiency of the tube at the center of the window. We find a reduction in efficiency as a function of radius, with a maximum loss of about 10% at the very edge of the active area of the tube. This is consistent with expectations based upon discussions with DEP.

#### **5.4.2.4 Shielding of HPDs from Magnetic Field**

Measurements by the LHCb group [10] showed that the PP0380 HPD shielded by 0.9 mm mu-metal tube can be exposed to fields up to 30 Gauss, but would require software corrections due to significant distortions of the photoelectron trajectories. Our goal is to reduce the field inside the HPD to a level at which no software corrections will be needed.

Measurements of magnetic field effects on HPD performance were made by placing the HPD in a pair of Helmholtz coils, having better than 5% field uniformity in the central region. The point spread function (PSF) is the image of a LED through a pinhole in a screen placed at the window of the HPD. The pinhole was moved to various locations and



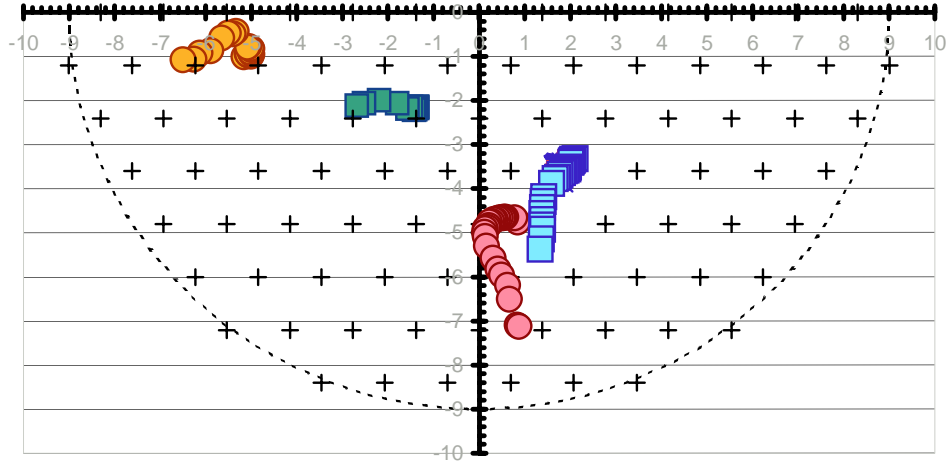


Figure 5.27: Images of the pinhole light source in the plane of the HPD diode (series of circles or squares). The scale is in mm. The crosses indicate the centers of individual hexagonal pixels. Different points within the series show displacement of the image under the influence of the magnetic field. The HPD was shielded as described in the text. The external magnetic field was longitudinal and it was varied from 0 to 55 Gauss.

the position of the PSF spot was reconstructed by a centroid method. The photoelectron trajectories are distorted by the applied field, thus the centroid moves across the pixel array, as illustrated in Fig. 5.27. The HPD was shielded by a tube of CO-NETIC AA foil, arranged in four layers of 0.25 mm each, with the HPD recessed 5 cm inside the tube. Both transverse and longitudinal applied fields were varied. Typical results for the displacement are shown in Fig. 5.28. The applied field required to displace the PSF a single pixel is about 45 Gauss for longitudinal field, and a factor of two higher for transverse field.

ANSYS calculations of the fringe field from the BTeV dipole analysis magnet predict that the field in the HPD region will be in the range of 50-150 Gauss. By surrounding the HPDs and their electronics with a shielding box (0.25" iron + 0.25" air gap + 0.125" mu-metal) the total field is reduced to a maximum of 10 Gauss. Even if this field is mostly longitudinal, such fields will result in image distortions which are a fraction of the pixel size as illustrated in Fig. 5.28.

A beehive of magnetic shields to be used in the beam test box is under construction. Unlike in the final detector, these prototypes are made of Aluminum, since magnetic shielding is not necessary for the test beam. The procedure for constructing the beehive has been established, using a mechanical jig to precisely align the shields. Since the hexads must be interchangeable, the corresponding sets of shields in the beehive must be well aligned in position and angle. Relevant thermal and mechanical tests of the various components have been carried out.

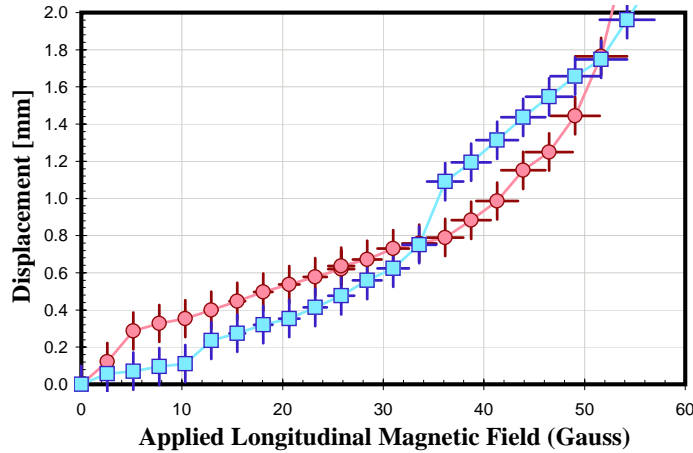


Figure 5.28: Typical displacement of the images in the plane of the HPD diode under the influence of longitudinal magnetic field. The pixel size is 1.4 mm. The two curves correspond to the outer image locations from Fig. 5.27.

#### 5.4.2.5 HPD Insulation

In the initial design, the upper electrodes of the PP0380 HPD were not insulated and the 20 kV voltage was supplied by a lead wire running along the tube (see Fig. 5.17). Such HPDs work well when operated at a sufficient distance away from any other metal objects. However, we discovered that we could not operate them reliably inside magnetic shields, which, for practical reasons, must be grounded. Painting the HPD with corona-suppressant material and using layers of kapton did not cure the HV breakdowns. We were able to eliminate them only by potting the entire gap with insulating material. This led to a slight redesign of the HPD. All tubes are now required to have an insulating layer to cover the upper part of the HPD. The 20 kV wire is completely encased inside the insulator layer. Fifteen tubes with this encapsulation have recently been delivered to Syracuse University and tests show that the potting has eliminated the HV breakdown. These tubes will be used in the beam test of the HPD system (in Summer 2004).

#### 5.4.2.6 Characterization of HPDs

A total of 15 HPDs have been delivered to Syracuse University. Each HPD delivered has been tested for high voltage behavior, pixel diode performance, mechanical tolerance, and optical characteristics. A characterization database is kept on all HPDs, which includes the DEP measurements of quantum efficiency and leakage current per pixel. All HPDs are tested at 20 KV, in contact with a magnetic shield, as required by the system design. All HPDs are flashed by an LED light source at two intensities to confirm basic pixel operation (no dead channels have been found). The mechanical dimensions are also measured. All HPDs are within specification except for the outer diameter which is slightly larger than specified

due to the eccentricity in the insulation material. This has been compensated for in the mechanical design of the mu-metal shields.

#### 5.4.2.7 High Voltage Distribution

See Section 5.3.8 for details on the HV system design.

#### 5.4.2.8 HPD Front End Readout

We have obtained 15 VA\_BTTeV hybrids for the test beam in Summer 2004. Their basic functionality has been tested. The intrinsic noise of the ASIC is also within specifications, as indicated by a pulse height scan of the channels (see Fig. 5.29). We have also performed initial tests where we pulse the HPD with an LED light source which is tuned to produce an average of 1 photo-electron per pulse. The response of the tube indicates that it is sensitive to single photons. Additional studies of the hybrid are in progress.

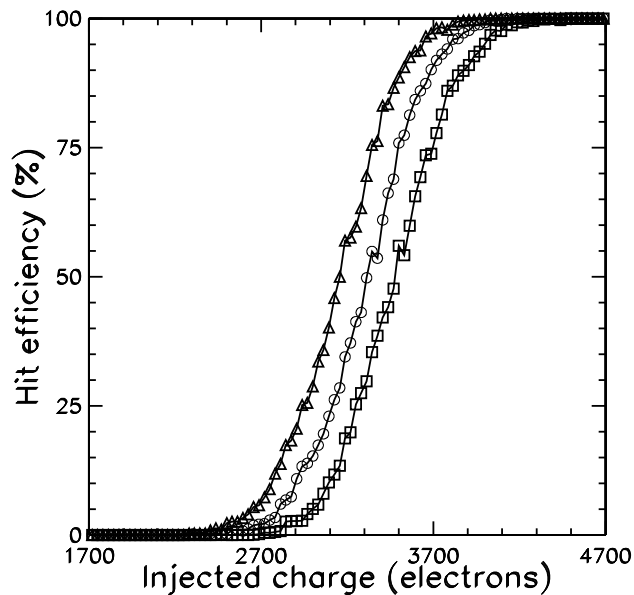


Figure 5.29: Threshold scan with the calibration pulse of one of the channels on the first BTTeV RICH front-end hybrid board. The three curves correspond to three different settings of the discriminator threshold. From these curves we measure the electronic noise to be  $\sigma = 300$  electrons.

### 5.4.3 Mirrors

We have developed techniques for investigating the optical qualities of mirror segments. We have obtained two mirror prototypes, each with a diameter of 60 cm and a radius of curvature of 660 cm, which is similar to the required radius for the BTeV RICH. One of the mirrors is made out of 6 mm thick Simax glass (4.7% of  $X_0$ ) and the other one of a thinner 2.2 mm glass substrate reinforced by two carbon fiber shells with a foam core (2.4% of  $X_0$ )<sup>2</sup> (see Fig. 5.30). These mirrors were studied at Syracuse, and both mean radius and spot size measurements were performed. The details of these measurements are discussed below.

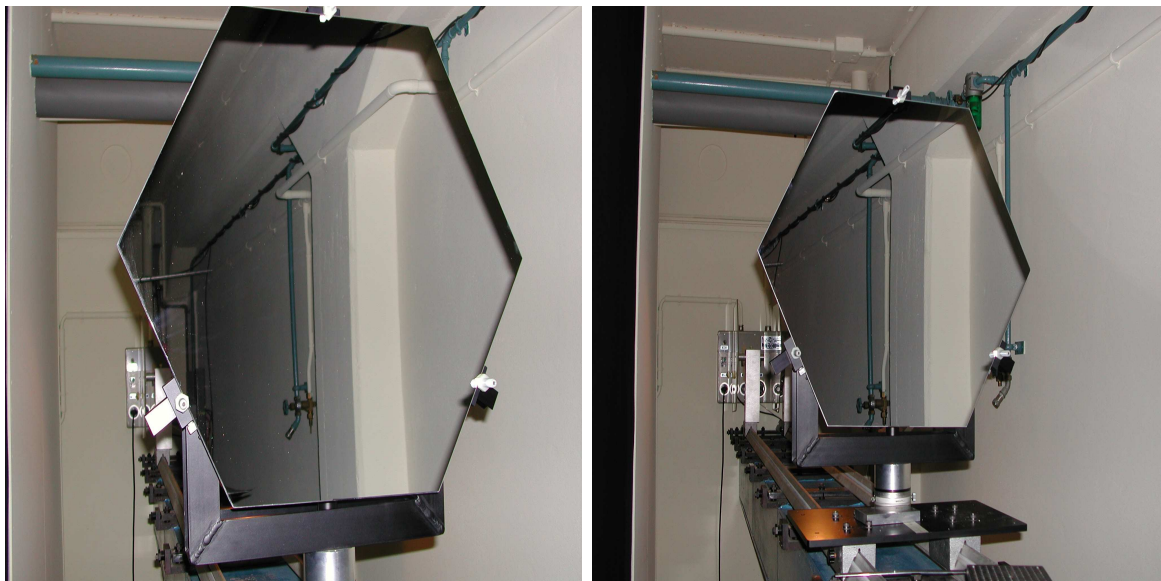


Figure 5.30: Two photographs, side-by-side, of the Turnov mirror prototypes (60 cm in diameter, 6.6 m in radius). The glass mirror is shown on the left. The glass-carbon fiber mirror is shown on the right. These mirrors will be used in the RICH beam test next spring.

#### 5.4.3.1 Measurement of Radius of Curvature and Spot Size

The mean mirror radius can be measured using the basic optical equation for the spherical mirrors, which is given in terms of the radius of curvature  $R$ , mirror-object distance ( $s$ ) and the mirror-image distance ( $s'$ ):

$$\frac{2}{R} = \frac{1}{s} + \frac{1}{s'}, \quad (5.1)$$

A test-stand which included an optical bench, a three-point mirror holder, and a point light source, was developed to measure the radius of curvature and spot size. The point

---

<sup>2</sup>The foam width is irregular and goes from 0 mm (at the edge) to 20 mm (in the center).

source illuminated the mirror and the reflected light was collected by a digital camera. To facilitate the measurements, the camera and the point source were put on the same plane perpendicular to the optical axis (see Fig. 5.31).

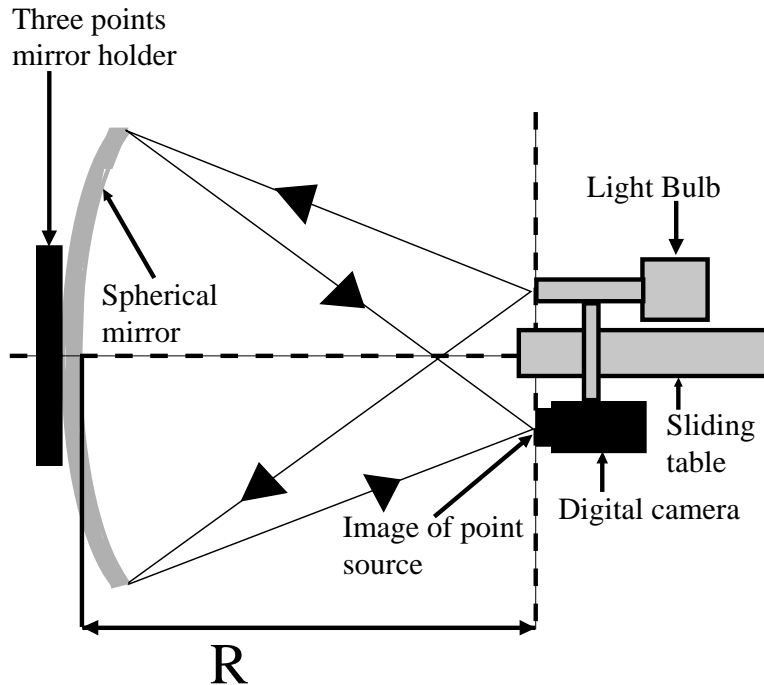


Figure 5.31: Procedure to measure the spot size.

To measure the mean radius  $R_{mean}$ , we adjust the separation between the point source and camera until the spot image is at its minimum size. At this point, the mean radius  $R_{mean} = s = s'$ . The minimum size of the spot image is called the spot size. Figure 5.32 shows the spot image for the glass mirror.

The intensity  $I(x, y)$  (in ADC counts) detected in each of the  $N_x \times N_y$  pixels is used to construct a quantity,  $P_D$ , defined as the percentage of the reflected light into a circle of diameter  $D$  with respect to the total measured light. The radius of the image at which  $P_D = 0.95$  is the aforementioned spot size, hereafter referred to as  $D_{95}$ . The center of the image is computed using an intensity weighted average of the  $x$  and  $y$  pixels' positions (the so-called "center of gravity").

Neither the center of gravity nor the spot size can be determined reliably if the pixels are saturated. The pixels saturate when the light intensity is too high. On the other hand, it is necessary to have sufficient intensity in order to accurately measure the tails of the intensity distribution. To account for saturated pixels, we developed an algorithm to merge four spot images taken at different light intensities into a single image.



Figure 5.32: Spot image from the glass mirror. The visible diameter is  $\sim 3$  mm.

We have applied this technique to both prototype mirrors. Here we show the results for the glass mirror only. Figure 5.33 shows the contribution of each one of the four images to the total one (left), and pixel values distribution across one row (right). Figure 5.34 shows the percentage of the focused light as a function of the spot diameter  $D$ . This method of merging the four images was demonstrated to converge by taking a fifth image at a higher intensity and merging it with the other four images. The resulting  $D_{95}$  value came up consistent with the previous measurement using four images.

Using this measurement process, we studied the glass and CF mirrors by measuring the mean radii and spot sizes. The results are summarized in Table 5.2.

The spot-image of the composite mirror (CF) showed 6 spikes (see Fig. 5.35), which are an odd feature not observed with the glass mirror. These spikes could be removed by masking off an  $\sim 5$  cm annulus near the edges of the mirror. Thus, we concluded that the mirror edges had been distorted.

Table 5.2: Mirror test results.

| Firm         | Spot size (mm) | Mean radius (cm) |
|--------------|----------------|------------------|
| IMMA (Glass) | 2.97           | 659              |
| IMMA (CF)    | 4.10           | 648              |

Similar tests were also performed at a test setup developed by the CERN-TA2 group. The measurements for the glass mirror agree very well, however, for the composite mirror, there seems to be some defects which developed either through some aging effect or through

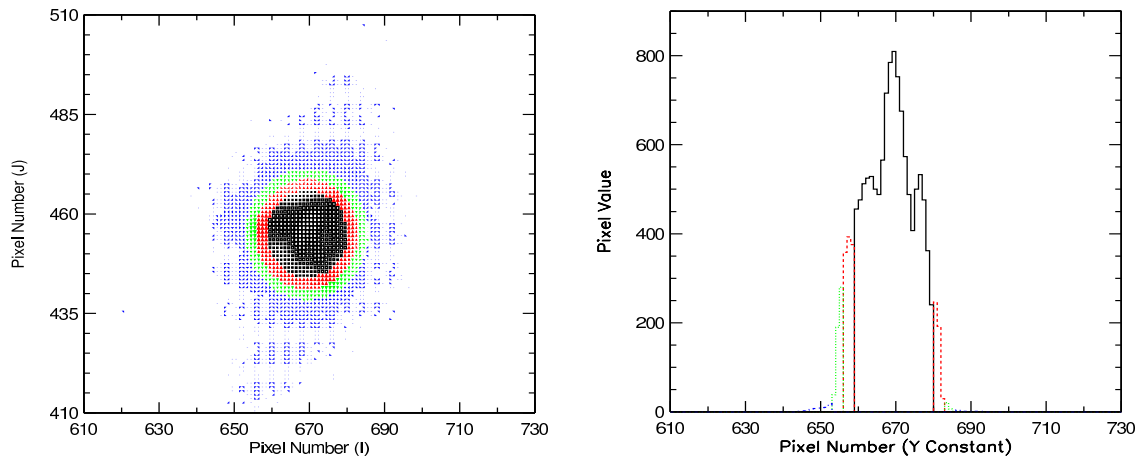


Figure 5.33: Four images merged into one. Two-dimensional spot image (left), pixel value distribution across one row (right). The different images are shown with different line styles.

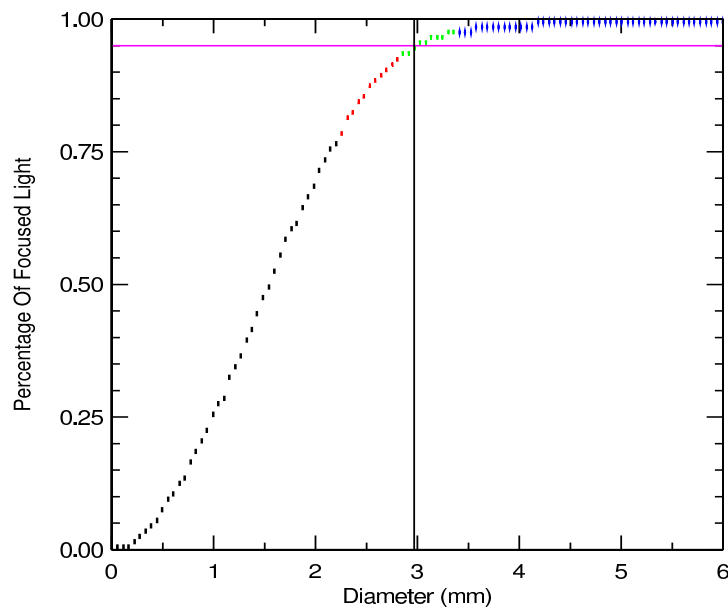


Figure 5.34: Percentage of focused light ( $P_D$ ) as a function of spot diameter..

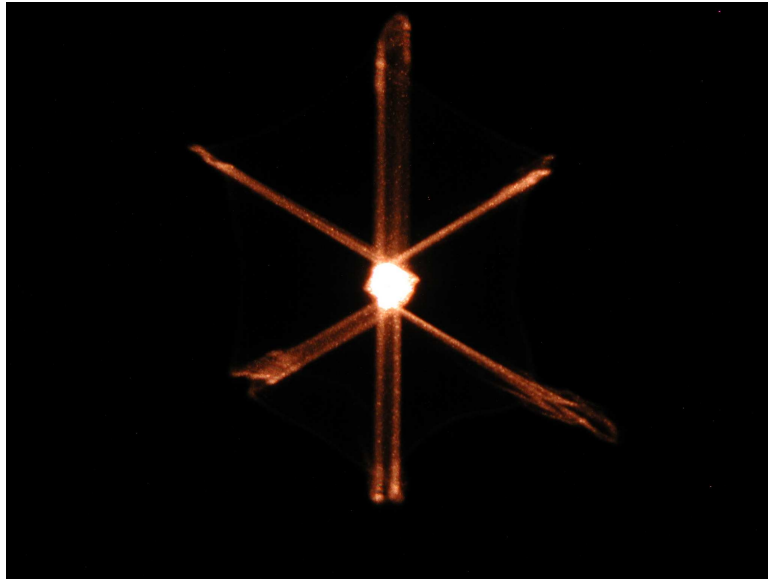


Figure 5.35: Spot image from the composite mirror without hiding the edges.

the mishandling of the mirror. Some changes had already been noticed even before their shipment to Syracuse. These mirrors will be used in the test beam in Summer 2004.

#### 5.4.3.2 Mirror Mechanical Support

We currently plan to attach the mirrors to a panel using three kinematic mounts attached to three points. One of these points will be a fixed mount, a second will act as a free mount, and the third will allow pivotal motion (see Fig. 5.36). Table 5.3 shows the composition of each mount.

Table 5.3: Basic mirror mount information.

| Components                | Material      | Fixed Mount | Free Mount | Pivot |
|---------------------------|---------------|-------------|------------|-------|
| Spherical bearing housing | Polycarbonate | ✓           | ✓          | ✓     |
| Spherical bearing         | Polymer       | ✓           | ✓          | ✓     |
| Threaded rod              | Aluminum      | ✓           | ✓          | ✓     |
| Nuts                      | Aluminum      | ✓           | ✓          | ✓     |
| Fixed tap insert          | Polycarbonate | ✓           | x          | x     |
| Pivot block               | Polycarbonate | x           | x          | ✓     |
| Split pivot block housing | Polycarbonate | x           | x          | ✓     |
| Dowel pin                 | Polycarbonate | x           | x          | ✓     |



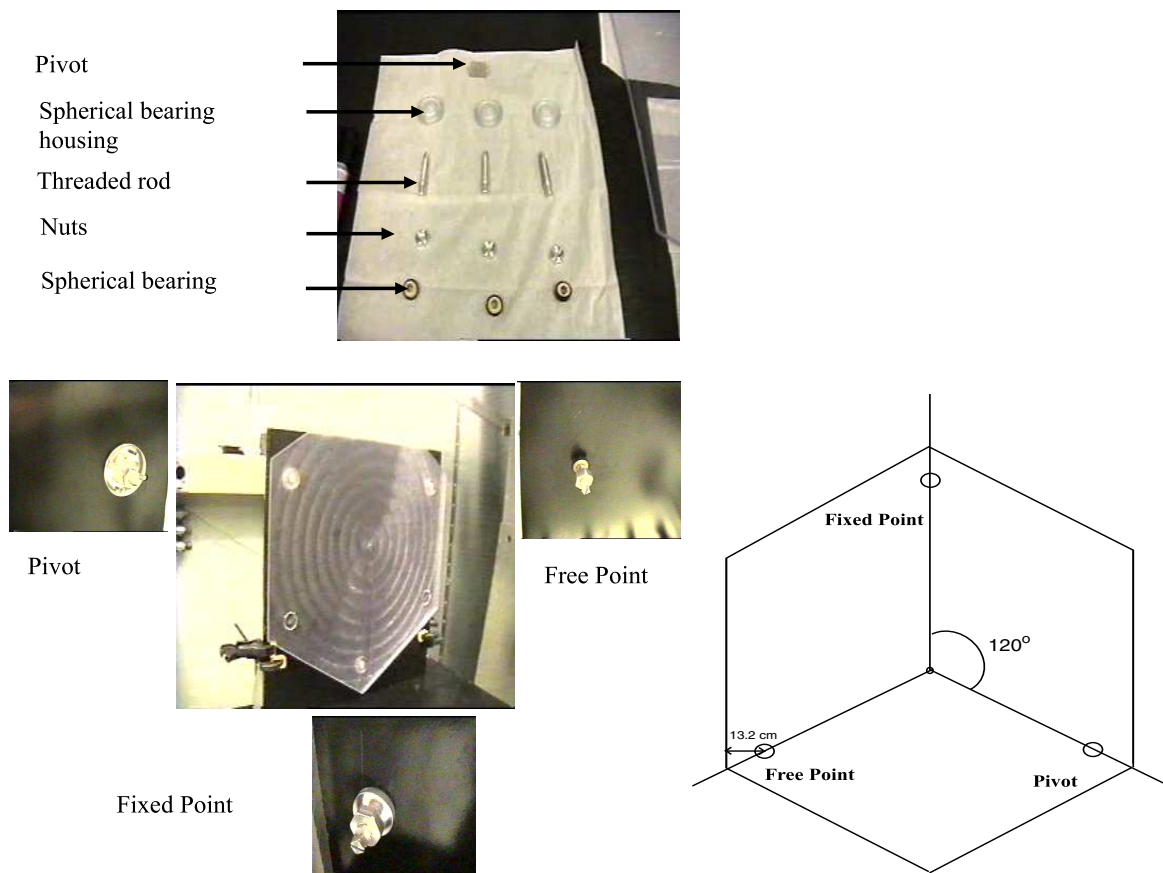


Figure 5.36: Mirror mount components and locations.

Prototype mirror mounts have been machined at Syracuse and tests have been done to check the adjustment of all three mounts. We have checked that the positions can be adjusted to the required level of 0.004" and that there is minimal cross-talk. That is, when adjusting one mount point, the other two do not migrate significantly from their set position. A summary of the tests performed is given in Table 5.4. The uncertainty on the mirror mount adjustments and the cross-talk measurements is of the order of the dial indicators precision.

Table 5.4: Tests performed on the prototype mirror mount.

|                            | Pivot (A)       |                | Free Mount (B) |                | Fixed Mount (C) |                 |
|----------------------------|-----------------|----------------|----------------|----------------|-----------------|-----------------|
| Adjustment to 0.004"       | ✓               |                | ✓              |                | ✓               |                 |
| Cross-talk ( $10^{-3}$ " ) | Move A by 0.24" |                | Move B by 0.3" |                | Move C by 0.28" |                 |
|                            | $\delta B=3$    | $\delta C=2.2$ | $\delta A=3.5$ | $\delta C=1.2$ | $\delta A=-6.0$ | $\delta B=-7.0$ |

### 5.4.3.3 Ronchi Test Of The Test Beam Mirrors

To probe the mirror quality, we performed a Ronchi test. We used a point source, placed approximately at the center of curvature of the spherical mirror, and a Ronchi grating of 50 lines/inch was used. It was positioned near the focus and in the path of the reflected light. The outcome of this test is a combination of fringes with a shape dependent on the mirror aberrations. These fringes would appear straight if the mirror were perfectly spherical. Any deformations of fringes is the result of deviations from an ideal spherical shape. This test was done for both testbeam mirrors, where the recorded pictures are shown in Fig. 5.37. For the glass mirror, the image shows clear zonal features (concentric rings), presumably associated with the grinding and polishing of the mirror. Aside from the zonal features, spherical aberration and possibly coma seem to be predominant. For the composite mirror, the aberrations seem to be somewhat irregular with the edge not clearly defined (odd features near the edges are also apparent when looking at the spot image). A spherical aberration is the most likely explanation for this observed Ronchi pattern.

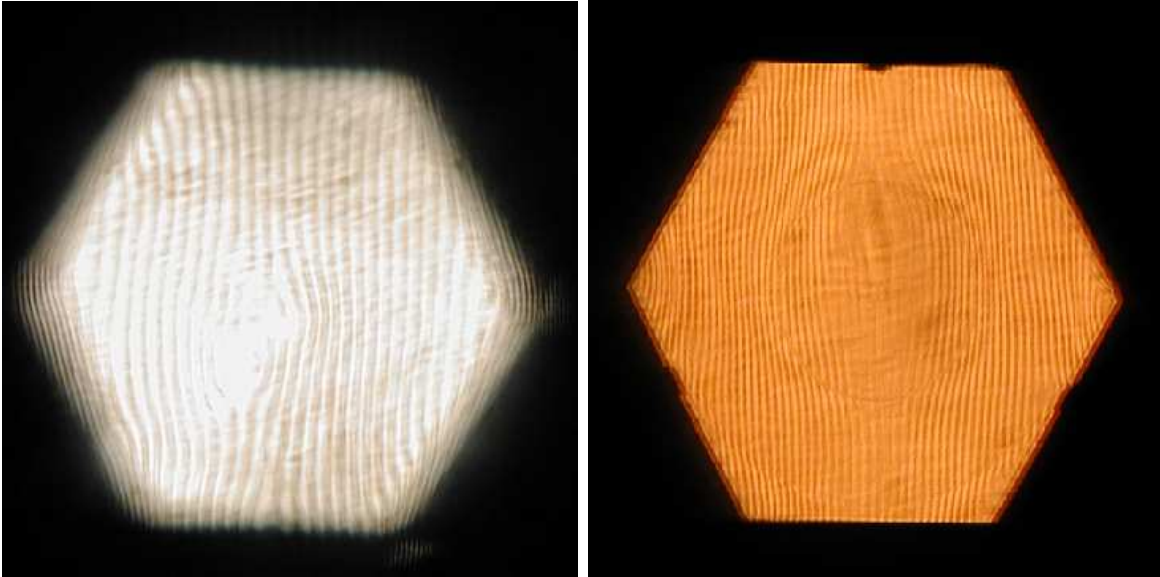


Figure 5.37: Ronchi test for the CF composite mirror (left) and the glass mirror (right).

## 5.4.4 Liquid Radiator

### 5.4.4.1 Liquid Radiator Versus Aerogel Radiator

As discussed in Section 5.3.1, we have determined from a detailed simulation that an aerogel radiator provides poor separation of kaons from protons below kaon radiation threshold (9 GeV/c). The initial simulations of the aerogel radiator neglected backgrounds from minimum bias events and from photon conversions in the BTeV detector components (beam pipe, tracking system, RICH radiators). While an aerogel radiator has been successfully used

in the HERMES experiment, their events typically contain only  $\sim 1$ -2 charged tracks as compared to  $\approx 80$ , on average, for the BTeV RICH. Thus, the positive experience with an aerogel radiator in HERMES was found not to carry over into the BTeV event environment. We therefore replaced the aerogel radiator with a  $C_5F_{12}$  liquid radiator. Photons are detected using conventional 3" PMTs which cover the side walls and top and bottom of the vessel (see Fig. 5.1). It should be noted that although some liquid photons do reach the mirror (about one third), they are imaged outside the instrumented area of the MAPMT planes and therefore do not contaminate the gas ring images.

To determine whether a  $C_5F_{12}$  liquid radiator system could provide adequate  $K/p$  separation, we simulated a RICH consisting of a 1-cm thick radiator and 3" PMTs on the side, top and bottom walls. Simulations of the liquid radiator performance for a sample of low momentum ( $< 9$  GeV/c) kaons and protons are compared to the simulations of the aerogel radiator in Fig. 5.38. For aerogel (top picture) the distribution of protons in the particle identification variable (see Section 5.7.2) is essentially indistinguishable from the distribution obtained for kaons. For the same sample of events and tracks, the liquid radiator (bottom picture) produces a meaningful separation of these two particle species.

We also simulated 2" diameter PMTs which would improve the photon position resolution, but would cost  $\sim 50\%$  more with only a 20% improvement in the total Cherenkov angle resolution per track (5.3 mrad for 2" tube versus 6.0 mrad for a 3" tube). Since the separation is  $\geq 3$  standard deviations using the 3" tubes, they are taken as our baseline choice.

#### 5.4.4.2 Selection of PMT Manufacturer

Because of the large number of PMTs needed, minimizing the cost per PMT is essential. The cheapest PMTs with single photoelectron capability are conventional head-on tubes, with an 8-stage box dynode structure which are produced in large quantities for use in medical applications (Gamma Cameras). With a HV around 1 kV, their gain is on the order of a few times  $10^5$  and they have a collection efficiency well above 90%. A standard alkali photocathode with a borosilicate glass window provides a peak quantum efficiency around 30%. The dark count rate is orders of magnitude below the level that would impact RICH performance.

At present, we are in contact with four different manufacturers which make such phototubes in a 3" size: Burle, Electron Tubes, Photonis and Hamamatsu (for examples see Fig. 5.39). We have tested sample PMTs from these manufacturers in order to establish single photoelectron detection capability and efficiency loss in a weak magnetic field. All tested tubes showed good separation of the single photoelectron peak from the pedestal in the pulse-height distribution, as illustrated in Fig. 5.40.

A possible mounting scheme using injection-molded fixtures to position a PMT inside the mu-metal shield is shown in Fig. 5.41. We are also considering integration of the mounting fixture with the HV divider board.

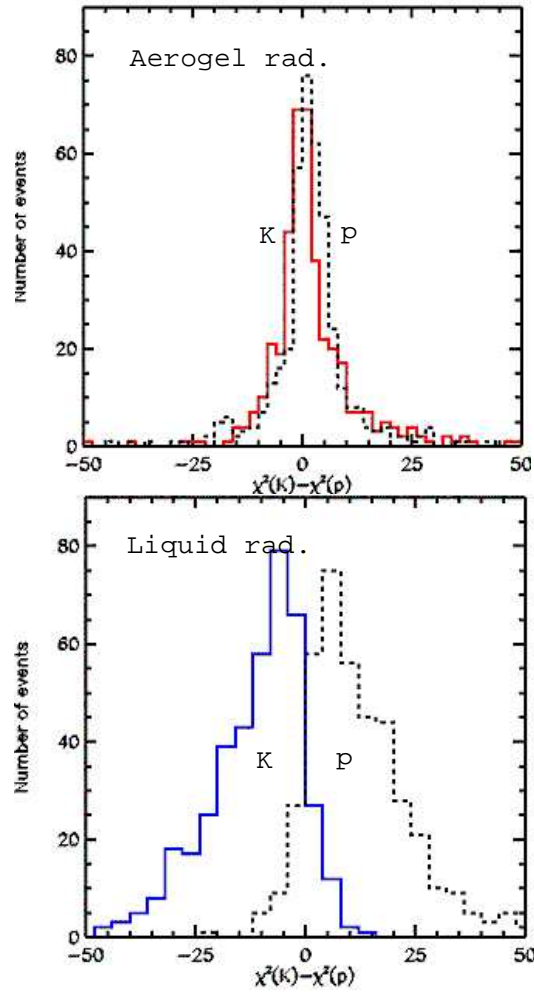


Figure 5.38: Performance of the RICH detector with an aerogel (top) and liquid  $C_5 F_{12}$  (bottom) radiator on a sample of low momentum (4-9 GeV/c) tracks. The events include one  $b\bar{b}$  event and an average of two minimum bias events. Solid histograms show the kaon distribution and dashed histograms show the proton distributions.

Calculations of the fringe magnetic field of the BTeV dipole analysis magnet predict fields up to 14 Gauss in the PMT region. The transverse component of the magnetic field can be easily suppressed by placing the PMTs inside 1 mm thick mu-metal tubes. Shielding of the longitudinal component is more difficult. Simulations were used to determine that we can extend the shielding tubes only as far as 2 cm beyond the photocathode without substantial light loss. Some tubes show more sensitivity than the others, as illustrated in Fig. 5.42. Since cross-calibration of the counting rates between different PMTs has not been done yet, we are not ruling out use of any of these tubes at this point.

It will be important to compare various PMT models in their single photon counting efficiencies, which factor in the quantum and the collection efficiencies. Since tube-to-tube



Figure 5.39: Photograph of 3" 8-stage PMTs from Hamamatsu and Burle.

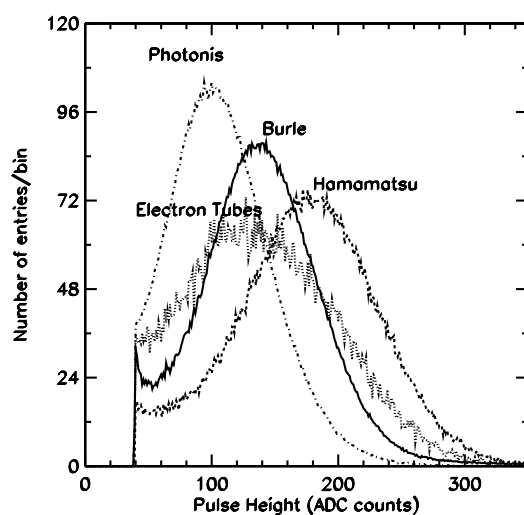


Figure 5.40: Pulse-height spectra obtained with various 8-stage 3" PMTs which are exposed to an attenuated LED light source. The single photoelectron peak is clearly visible for each, with a good peak-to-valley ratio.

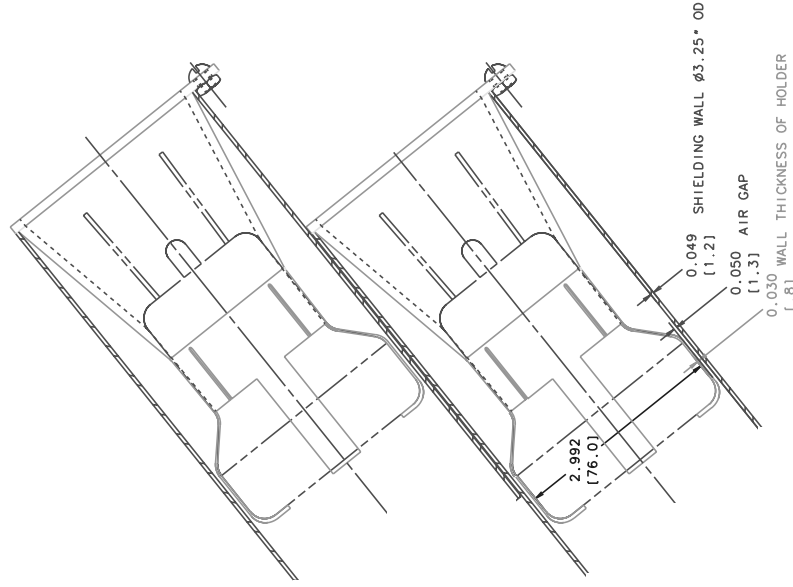


Figure 5.41: Possible mounting scheme for 3" PMTs in their magnetic shields.

variation is expected even from a single manufacturer, such studies need to be performed on a large sample of phototubes. We plan to order about 16 PMTs from each vendor, test them on a bench, and later, construct an array that together with the liquid radiator prototype will be studied in a test beam.

We are also exploring with the manufacturers various options for the PMT package. In one scenario, PMTs would be delivered with flying leads. We would develop our own HV divider boards and mechanical support mechanism. It is likely, however, that we will have the manufacturer deliver the tubes already integrated and tested with the HV divider boards. Another possibility is that the mechanical support would be built into these boards. More interactions with the manufacturers are needed to determine the most cost effective solution, which may be different for different vendors.

#### 5.4.4.3 PMT Readout Electronics

Since the output signals from the liquid radiator PMTs and the MAPMTs considered for the gas radiator will be very similar, we plan to adopt the MAPMT readout architecture (see Sec. 5.4.1) to readout the PMTs as well. One front-end board is likely to serve 64 PMTs, with signal cables soldered on both ends (to minimize costs associated with connectors). A different layout of the input traces to the analog part, or a dedicated interface board will need to be developed.

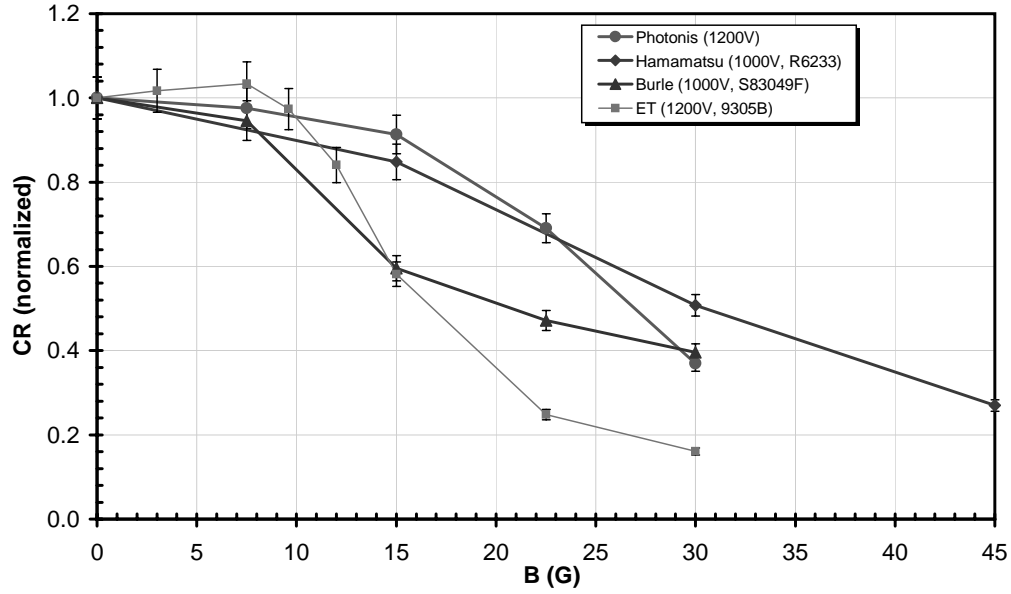


Figure 5.42: Dependence of the counting rate of 3" 8-stage PMTs from various manufacturers on the longitudinal magnetic field, shielded by 1 mm mu-metal tubes extending 2 cm beyond the photocathode. All counting rates were normalized to 1 for no magnetic field applied.

### 5.4.5 Radiation Damage Studies

The photon detectors and their readout electronics are situated beyond the aperture of the detector, and therefore are shielded from the interaction point by the dipole magnet elements. Our simulations indicate that the flux of slower particles bent by the magnet onto the PMT array will produce a delivered dose of up to 1 krad/year in the hottest spot. Radiation levels in the HPD area will be lower by a factor of 20. We are conducting our own radiation damage studies for PMT windows and materials that we are considering for the gas vessel window (e.g. UVT acrylic). Transmission curves measured at Syracuse for various materials provided by prospective vendors are shown in Fig. 5.43 (solid lines). The samples were exposed to a radiation dose of 10-15 krad by spray from the Tevatron Booster. This dose is equivalent to about 10 years of PMT exposure in the hottest locations (200 years for MAPMT arrays). The spray consists of a mix of moderate energy (an MeV to a few GeV) protons, neutrons and gammas. The transmission curves have been remeasured (dashed lines). The borosilicate glass shows a few percent loss of light (the sample developed a visible tint). A smaller deterioration is observed for the UV glass (the sample from Hamamatsu). No change in transmission properties of UVT acrylic have been detected. The quartz also shows no deterioration, as expected. The samples will be exposed to a higher radiation dose and their transmission will be again remeasured.

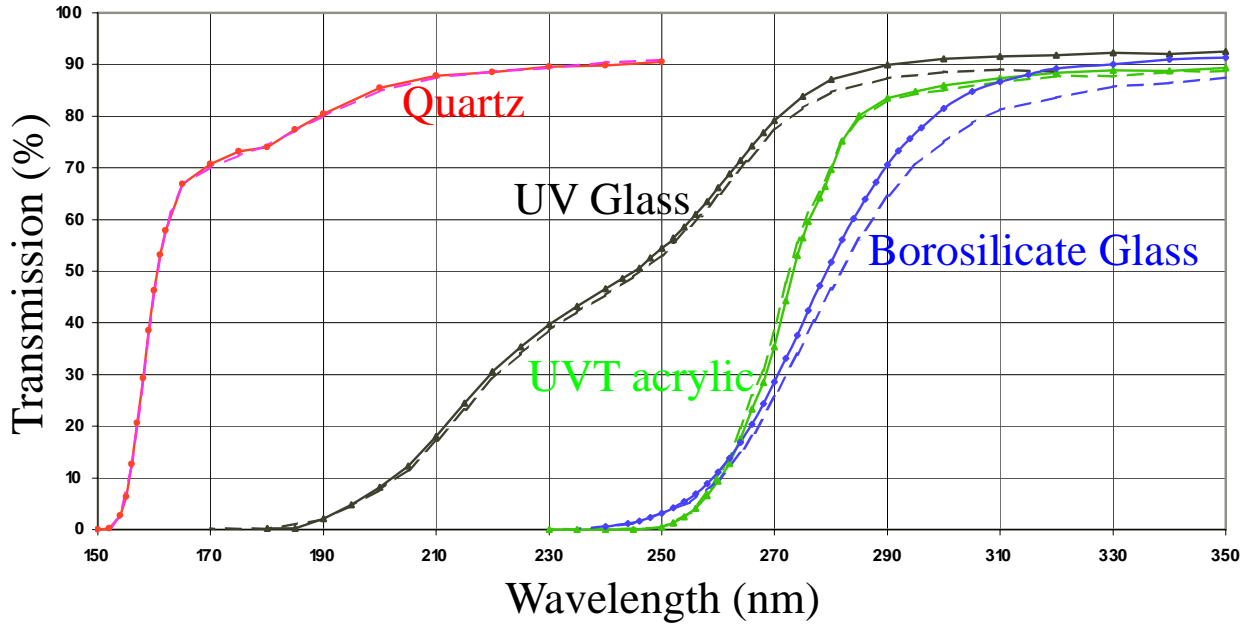


Figure 5.43: Transmission measurements for various samples of window materials for photodetectors before (solid lines) and after (dashed lines) 10-15 krad of radiation. The quartz sample was supplied by Electron Tubes. The UV glass and borosilicate glass window samples came from Hamamatsu. The borosilicate glass from Burle and Photonis gave similar results (not shown).

## 5.5 Planned R&D

Many of the technical challenges of the RICH have been addressed over the last several years through extensive R&D. Individual components and subsystems of the RICH have been tested and function in accordance with design specifications. We are now at the phase where all subsystems must be integrated to demonstrate that they function together as a single system and that we are able to achieve the required Cherenkov angle resolution. The planned R&D is focused on demonstrating these aspects of the RICH design. To that end, we are planning for a beam test of the gas radiator system starting in June 2004. A beam test of the liquid radiator system is expected to occur within a year after the gas system beam test has been performed.

### 5.5.1 Beam Test of Photodetection Systems

A beam test of the gas RICH system, including the gas radiator, a mirror tile and photodetectors is planned to begin in June 2004. The beam test has three goals: to prove that MAPMTs and HPDs can be operated in a closely-packed array under realistic beam conditions, and to verify our calculations for the expected light yield and Cherenkov angle



resolution. A drawing of the mechanical design of the RICH prototype is shown in Fig. 5.44. It consists of a full length radiator volume, with a single mirror tile at its end, tilted with respect to the beam by the nominal angle. The enclosure is required to be both light tight and gas tight. The mirror will focus Cherenkov rings onto a photodetector array. We plan to have two independent and interchangeable photodetector arrays, one filled with MAPMTs and the other filled with HPDs. The MAPMT array consists of 54 MAPMTs, which form a ring at the proper radius to detect the Cherenkov photons. An event display showing the geometry of the MAPMTs and many overlapping Cherenkov rings is shown in Fig. 5.45. The HPD array consists of 15 HPDs. The corresponding event display is shown in Fig. 5.46. In each case, only locations along the Cherenkov ring are filled with photodetectors. The arrays are enclosed in a gas volume that accommodates the magnetic shield beehive, structural supports, readout electronics, and cabling. It also provides electronic shielding. This enclosure has the same mechanical design as the final design, and will test our ability to close-pack the MAPMTs (and HPDs) in an operational detector, with regard to competing mechanical, electronic, high voltage, power, optical, and cooling issues.

The test box will be mounted on adjustable jacks to translate the box horizontally and vertically with respect to the beam. This will allow us to scan different parts of the mirror with the Cherenkov radiation. As long as the beam is parallel to the axis of the radiator, Cherenkov light will be focused on the instrumented area of the MAPMT/HPD array. All of the test beam parts are in the process of being fabricated at Syracuse. The box will be pre-assembled at Syracuse before being shipped to Fermilab.

### 5.5.2 Beam Test of the Liquid Radiator

The Syracuse group has dealt with liquid radiators in the R&D work for the CLEO III RICH. Some equipment and radiator prototypes from that work will be adopted for initial studies of the  $C_5F_{12}$  liquid.

The design of the liquid radiator is discussed in Section 5.3.2. One module of the liquid radiator (Sec. 5.5.2) and an array of PMTs (Sec. 5.4.4.2) will be exposed to a test beam in 2005. They need to be connected by a light-tight arm, which does not need to be hermetic since the medium inside can be air. A test box which will support the liquid radiator and the PMTs will need to be designed. The readout electronics will use the same architecture as the MAPMTs, except for the details of the lead connections from the PMTs to the analog front end of the readout chip. These aspects will be addressed in the upcoming year.

In addition to the nominal separation and orientation of the radiator and the PMT array, we will also investigate much larger lever arms to confirm the size of the chromatic effects. Since the test array will contain a much smaller fraction of the Cherenkov image than the full size PMT array, Monte Carlo methods will be used to extrapolate the test beam results to the full detector design.

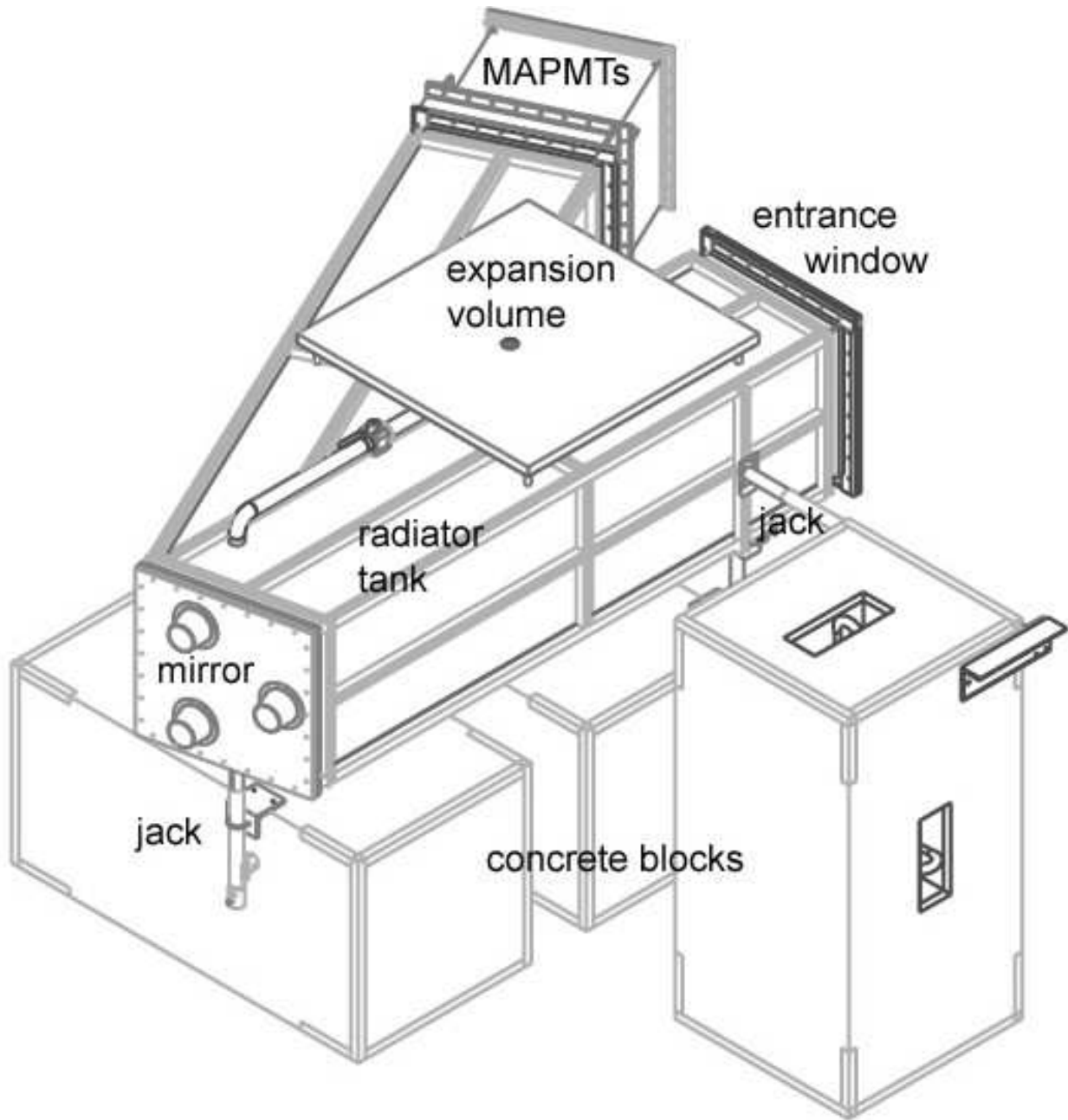


Figure 5.44: Drawing of MAPMT/HPD test beam RICH prototype.

# Cumul Evt Disp BTeV-RICH MAPMT BeamTest

09/22/2003

19:23

RUN ID: 12321

Evs = 1001

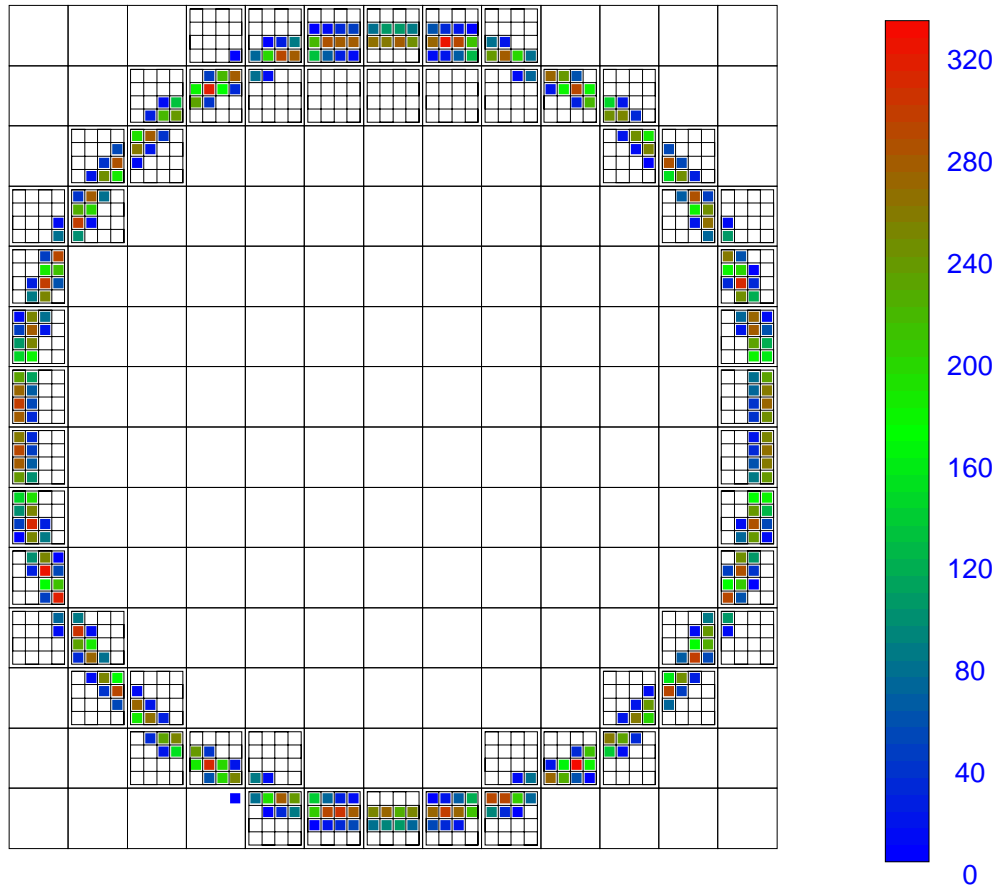


Figure 5.45: Cumulative display for many simulated events for the test beam. Individual pixel location for the deployed MAPMTs are shown. Filled pixels represent light intensity integrated over a large number of overlapping Cherenkov rings from beam particles.

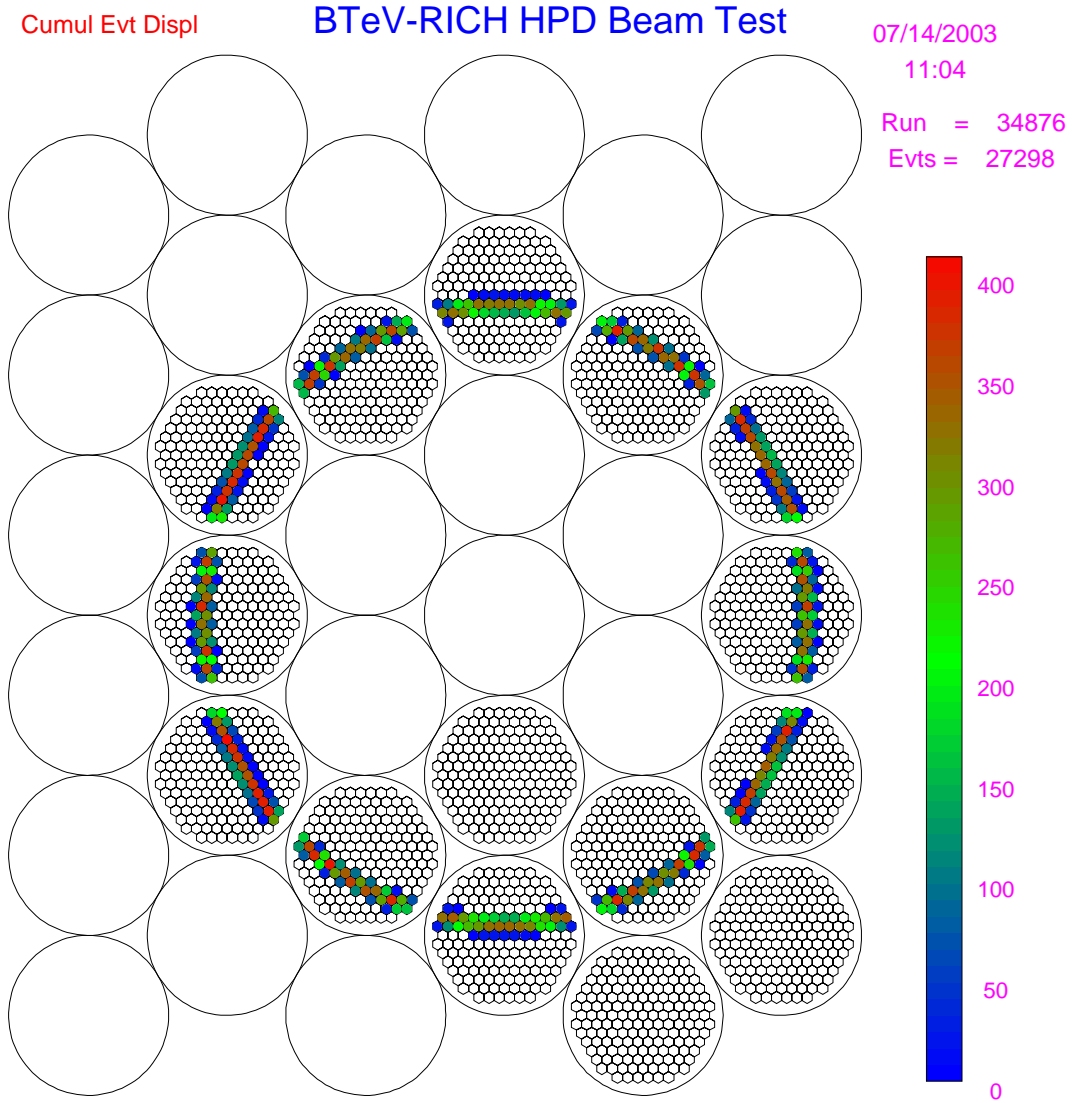


Figure 5.46: Cumulative display for many simulated events for the test beam. Individual pixel location for the deployed HPDs are shown. Filled pixels represent light intensity integrated over a large number of overlapping Cherenkov rings from beam particles.

### 5.5.3 R&D on Mirrors

The design and specifications for the RICH mirrors are discussed in Section 5.3.4. As part of our R&D effort, we are investigating various technological choices. One relatively cheap and well established technology choice is to use a glass mirror. Typical glass mirrors would introduce about 5% of a radiation length ( $X_0$ ) in front of the EM calorimeter. They would also require a heavy support structure. We are therefore investigating alternative mirrors which use lower radiation length materials, such as carbon fiber. Carbon fiber mirrors as thin as 0.8% of  $X_0$  can be built [14].

To this end, we have recently contacted several US companies (CMA, COI, Hextek, Opticon, GMO) and International companies (St Petersburg Research Institute for Space Optics (Russia), IMMA (Czech Republic)) which are well known to produce both composite mirrors and/or glass mirrors. We are in the process of obtaining price quotes for the full mirror system from each of these companies. The decision of which technology choice will be driven by cost and tests performed on sample mirrors obtained from competing vendors. The tests include the spot size and radius of curvature measurements, a Ronchi test, reflectivity, and response to humidity. We will also expose the sample mirrors to radiation at levels of 1 times and 5 times the their expected dose, and repeat the above tests.

### 5.5.4 Mirror And MAPMT Plane Alignment

Proper alignment of both mirrors and detection plane is a complicated task which is important to achieve the required Cherenkov angle sensitivity. In the current design, we have two arrays of spherical mirrors each one having 19 full hexagons (64.2 cm side-to-side), 4 half hexagons and 7 hexagons missing one edge-triangle. These segments will be attached to individual support panels using three kinematic mirror mounts (see Section 5.4.3).

There are two aspects which need to be considered with respect to alignment. First, there is the initial alignment of the mirror array when the detector is installed, and the second is the continuous monitoring of the alignment during the life of the experiment. The initial alignment will depend on whether the pixel system and the straws upstream of the RICH are already installed in the spectrometer. If they are not, we will be able to locate the mirrors in the RICH vessel and align them in their final position. If the upstream detector components are installed prior to the RICH, alignment in place is more difficult.

For the initial alignment, we first mount the mirror array and allow the system to settle (due to its own weight). The LHCb RICH group observed that the main relaxation of their system, especially the screws, occurs during the first 5 days. Of course this depends on the rigidity of the system and if heavy glass or lightweight carbon fiber mirrors are used. The position of the array can be monitored to see when it has finished settling. After it has settled, we first perform a visual alignment of each individual segment followed by a fine adjustment. We envisage two scenarios depending on when the RICH would be installed.

If the RICH is installed prior to the pixel system and upstream straws, the mirror-to-mirror alignment can be done by placing a collimated light source at the interaction point and minimize the spot image off to the side of the magnet. A layout showing the ray optics is

shown in Fig. 5.47. Two rays segments, originating from the interaction point, and focused at the radius of curvature, are indicated in the figure. Once the detection plane is installed we can do a global alignment and fine adjustment after installing the monitoring system which is described later in this section.

If the RICH is installed after the pixels and straws, we will likely have to perform the mirror-to-mirror alignment outside the C0 hall inside the RICH box, and then perform a global alignment after moving the whole structure to the C0 hall. In this case the mirror will be put in a thin mylar bag to keep them dry. The fine mirror adjustments can be done after installing the monitoring system, which is described later in this section. For the mirror-to-mirror alignment, we have considered two possible alignment schemes. Both require roughly 7 meters perpendicular to the mirror plane. The first method requires a point source and a CCD camera. These two will be used for mirror quality testing prior to the installation. As shown in Fig. 5.48, a theodolite will be employed to determine the desired center of curvature of the mirror to be aligned. The center of the point source and the CCD camera are then sited at this point. If the mirror is perfectly aligned, the image of the laser point source will be at the center of the CCD screen. By visual inspection, one can determine the displacement to the order of 1 mm, corresponding to a tilt angle of the mirror of about 0.1 mrad. The alignment can be greatly improved by using an online program which computes the center of gravity of the image. This method provides a continuous view during adjustment. It also allows for monitoring over longer periods of time to check for any possible long-term migration.

The second method is to use a theodolite directly with the function of “auto-collimation” as shown in Fig. 5.49. This method was used by the COMPASS experiment [15]. The auto-collimation function is for the perpendicular alignment of a plane mirror. It works in a similar fashion for a spherical mirror, since we can place the theodolite at the desired center of curvature. The observer brings a projected reticule into alignment with the standard reticule. Misalignment of the mirror causes the reticules to be displaced with respect to one another. The method could provide much superior precision than the first method.

Because the alignment of the mirror system is a critical to achieving the required Cherenkov angle resolution, the mirror positions will be monitored throughout the life of the experiment using an online monitoring system.

We can use collimated light sources for each mirror segment and the reflected light can be read out using the MAPMTs (or HPDs). From an optical point of view, the best position of the light source would be at the entrance window. On the other hand we have to minimize the radiation length of material in the detector volume. Another possibility is to attach optical fibers on the corners of the mirrors, and have them directed toward the MAPMT plane so that they mimic reflected photons.

Figure 5.50 shows a possible better solution. This solution entails mounting collimated light sources on the top and bottom of the front window. Simulations show that it is possible to place these LED’s in predefined positions and directions so that mirror tiles can be aligned individually. The light source could be an array of LEDs with suitable collimators. The collimation could be achieved using a set of holes drilled into a plate and the angles of the

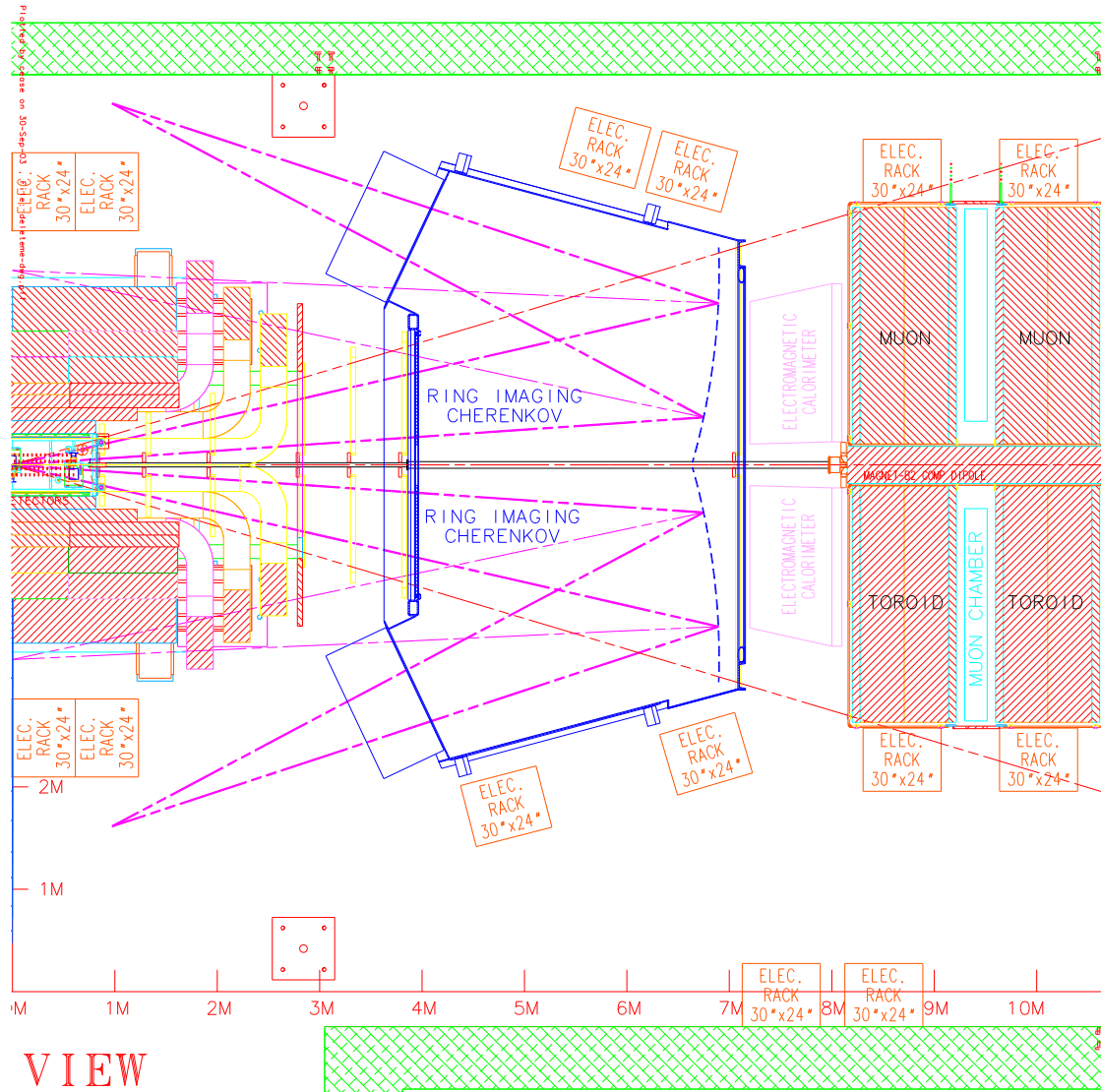


Figure 5.47: Plan view of detector showing optical ray traces which can be used to align each mirror tile.

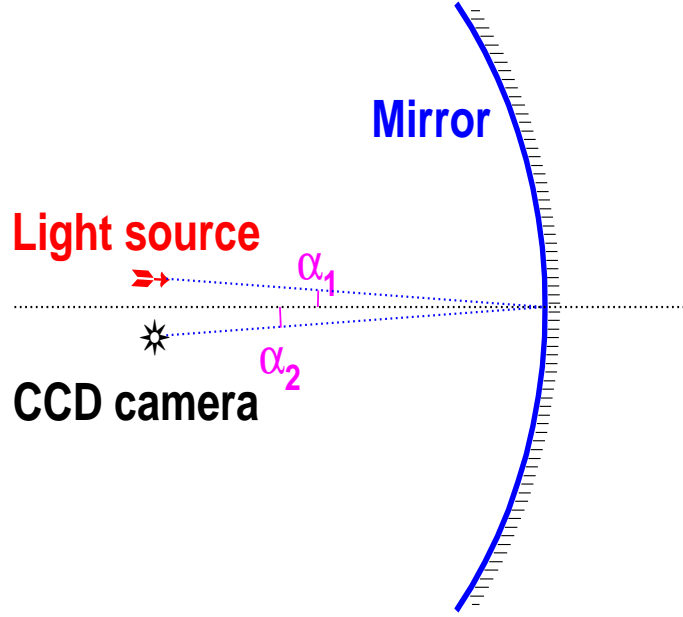


Figure 5.48: Mirror alignment using point light source and CCD camera.

holes could be chosen to illuminate specific mirrors. The hole could be made relatively small to create a relatively narrow beam of photons. In this model, the light hits the mirrors at more of a glancing angle.

Using the readout from the photodetectors, one can track changes in alignment of both the mirrors and MAPMT's. To determine which system has moved (in the case that a relative motion is detected), we can have separate light sources for monitoring the MAPMT arrays position. Alternately, we can rely on alignment of the MAPMT plane with the same method as alignment monitoring of support structure described above. The main difficulty of this method is to ensure the direction of the light source is as stable as the detector.

## 5.6 Production Quality Assurance and Testing

The RICH detector is a critical component of the BTeV detector, and it is important that all the major components are thoroughly tested. In some cases, components will be tested at several stages in the fabrication process. In this section we describe the quality assurance and testing which will be done for the primary components of the RICH. In particular, we discuss:

- Photon Detectors for gas system (MAPMTs or HPDs)



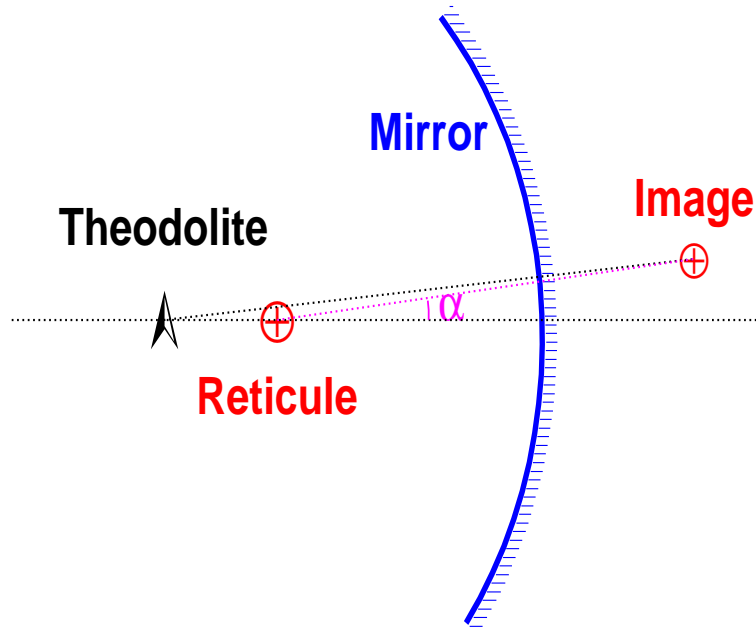


Figure 5.49: Mirror alignment using a theodolite.

- Photon Detectors for liquid system (PMTs)
- Readout Electronics
- Mirror Tiles and Array
- Liquid and Gas Radiators
- Power Supplies
- Cabling
- Cooling System

### 5.6.1 Photon Detectors for Gas System

The single most costly item for the RICH are the photon detectors, and it is therefore critical to ensure their long-term success. In the RICH design, we will be prepared to use either Multi-anode Photomultiplier Tubes (MAPMTs) or Hybrid Photodiodes (HPDs) for detecting photons from the gas radiator. We therefore present both scenarios below. The QA program will progress from basic functionality tests toward a configuration which resembles

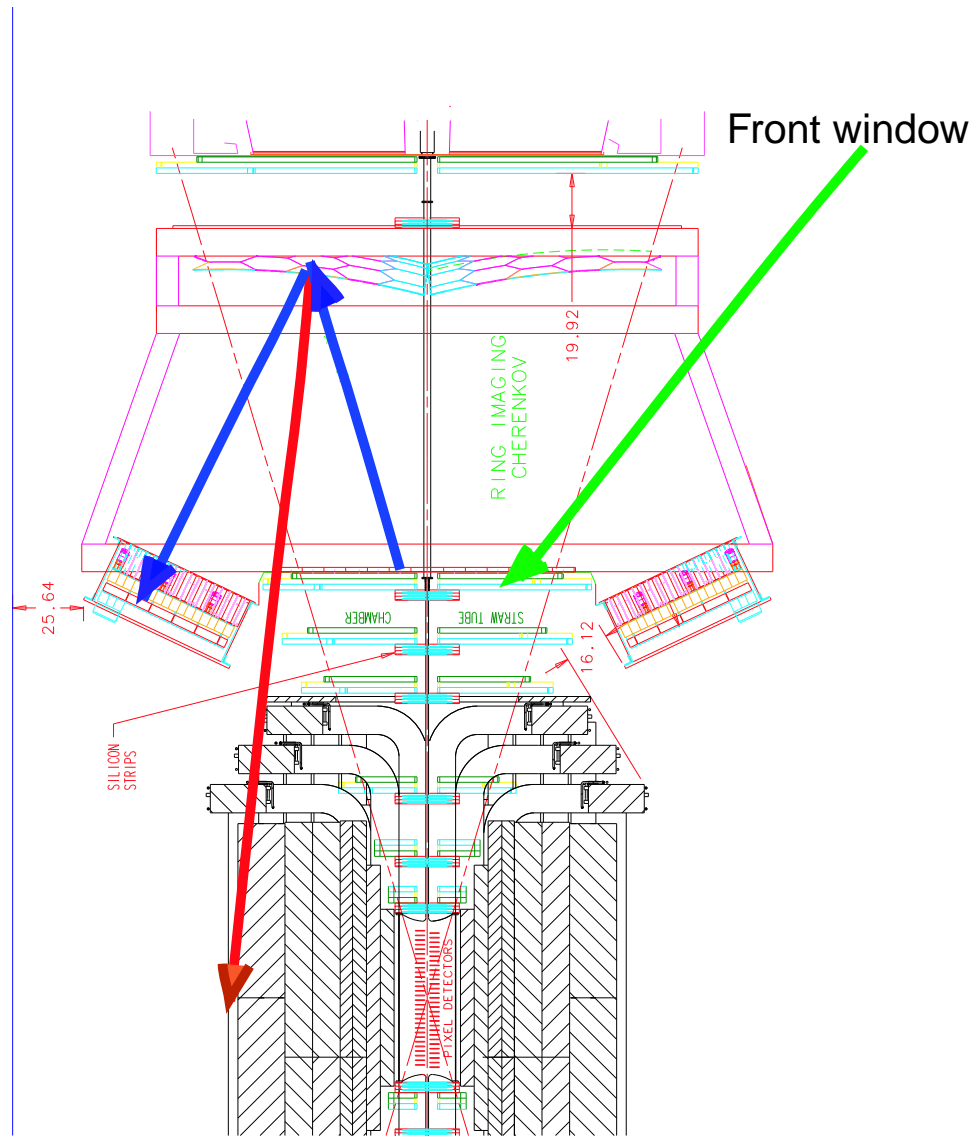


Figure 5.50: Alignment scheme using collimated light sources mounted on the top and bottom of the front window. The arrow originating from the front window represents a focused LED ray which reflects off a given mirror segment and is detected in the photodetection plane.

true detector operation. The tests will be performed at Syracuse University, which has four areas equipped with small to large dark-boxes which will be used for these tests. If necessary, additional test-stands can be constructed and commissioned within a matter a few weeks.

#### 5.6.1.1 HPD Testing

The initial tests of the HPD will be performed on each device as a single unit. The data from each step will be recorded in an electronic logbook for ease of tracking the testing history for

each tube. The electronic logbook will also contain a mapping which identifies the locations of each tube in the photo-detector array. The initial tests on the HPD include:

- High Voltage and Silicon Bias Checkout: In this first test, the HPDs will be placed in a mu-metal shield and the 3 high voltages (20 kV, 19.89 kV and 15.8 kV) and the silicon bias voltage will be applied. The current draw on each supply will be monitored to make sure it's stable and within specification. The HV supplies are expected to draw almost no current, and the silicon bias typically draws 10 nA of current, and should not exceed 20 nA.
- Photocathode Sensitivity Test: Here, we check that the photocathode is indeed producing photoelectrons at approximately the correct rate. We will illuminate the HPD face with a LED located precisely 6 in. from the front face and centered at radius  $R=0$  with respect to the center of the tube. The current through the LED will be set to a predetermined value and the current drawn on the silicon bias supply will be recorded. This test will be repeated for three wavelengths in the sensitive region of the photocathode.
- Focusing Test: The goal here is to demonstrate that the electrostatic focusing is working properly. This test will consist of an XY scan of the face of the HPD using a blue LED and optical fiber. For each position, we pulse the LED at a light level expected to produce a single photoelectron, on average, and measure the positions of the detected photoelectrons. A program will read in this data, and use it to infer the position of the light source on the face of the HPD. The inferred position must be consistent with the true position. The program will also compute the RMS spread in positions of hits and this should be consistent with the expected spread.

The aforementioned tests will be carried out in the Quality Assurance Test Station shown in Fig 5.51. A block diagram of the setup for the XY scan is shown in Fig. 5.52.

Once the tubes have passed these single tube tests, a HEXAD, consisting of six HPDs in a hexad structure will be produced and tested (see Fig 5.21). The hexad will be in its mu-metal beehive mounting structure by this point. The hexad is mounted in the burn-in test box. The burn-in test-stand will be equipped with the VA\_BTTeV readout electronics and read out using LabView. The six HPDs will be each pulsed with a blue LED and read out. This test will run continuously for 1 week, and we will monitor the following quantities:

- Current through each LED
- silicon bias current
- current draw on HPD high voltages
- Count rate per pixel
- RMS variation in count rate per pixel



Figure 5.51: Quality Assurance Test Station.

The data for these runs will be stored in a file which will be retrievable through the electronic logbook.

#### 5.6.1.2 MAPMT Testing

We first test a single tube, or perhaps a small batch of four tubes for basic functionality. We then form long-term tests in the burn-in box. The tests are described in what follows:

- **Plateau each Tube:** For each of the 16 MAPMT channels, we will measure the background-subtracted count rate versus applied voltage. We require that all channels plateau by -975 V.
- **Photocathode Sensitivity:** Illuminate face of MAPMT with an LED and measure current draw through the dynode chain. We repeat this for 3 different wavelengths in the range of 450 - 650 nm. The current draw should be consistent from tube-to-tube.
- **Relative Efficiency:** Perform an XY Scan of the face of MAPMT with a blue LED for a fixed live time. At each point, store the number of hits above threshold with and without the light source. A program reads in the data and generates an XY profile of the relative response of the tube. The LED will be tuned to produce 1 photo-electron, on average. We will require that the relative efficiency of the tube exceed a minimum specified value.

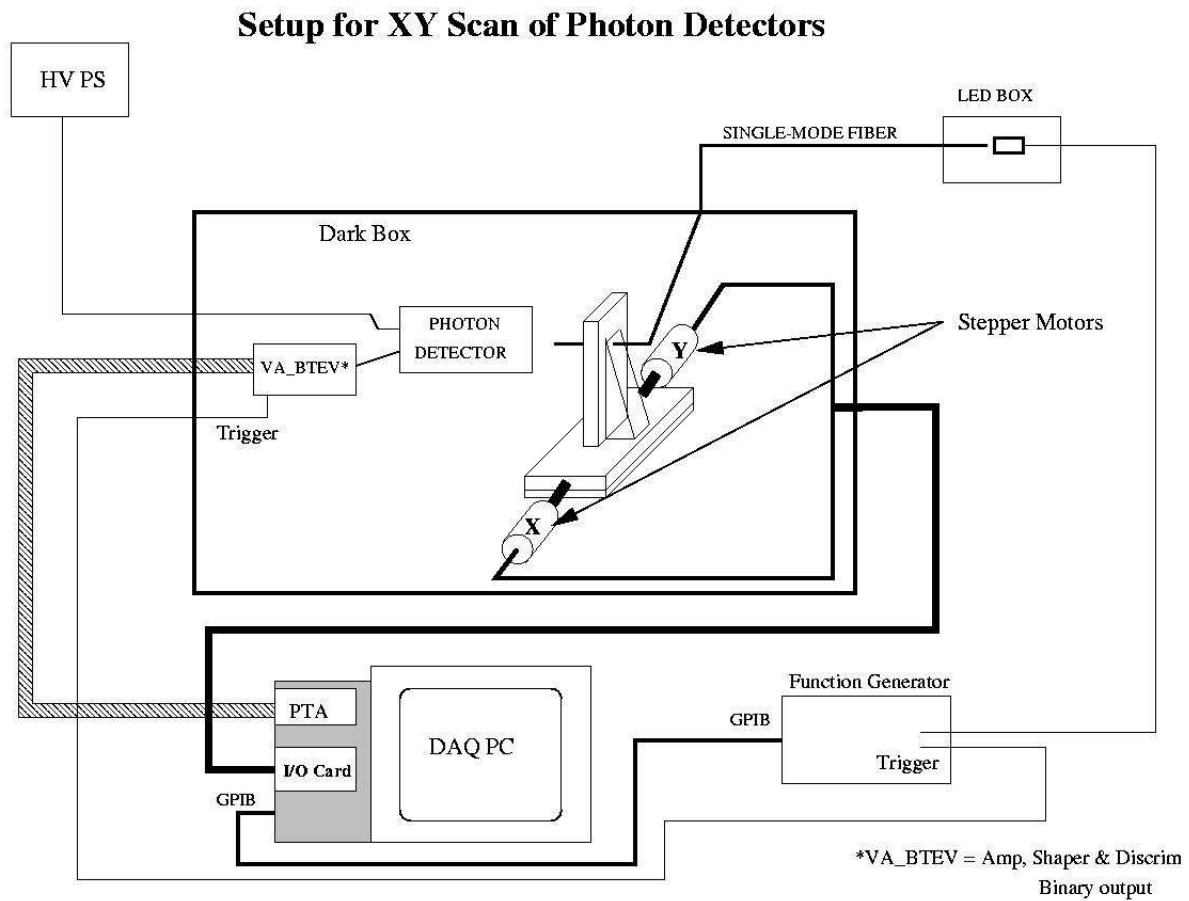


Figure 5.52: Setup for XY scanning of photon detectors. The photon detector may be either an HPD, MA-PMT or a single-anode PMT. The DAQ PC controls the stepper motors as well as the readout of the photo-detector.

- Magnetic Field Immunity: We will test the first 10-20 tubes of each batch to ensure that they suffer no more than 5% loss of efficiency at 30 Gauss longitudinal field. We will also randomly test several tubes throughout the batch.

The longer burn-in tests will be analogous to the HPD tests. A set of MAPMTs will be mounted in their mu-metal structure and connected to their readout chips. Each tube will be pulsed with a blue LED source for a period of one week. During this time, we will monitor:

- Total current draw for the MAPMTs
- Current draw through the dynode chain
- Count rate/pixel
- RMS Variation in count rate

We require that all monitored values are within expectations and steady over time.

### 5.6.2 Single Anode PMTs

The single anode PMTs are used for the liquid radiator system. The QA tests are analogous to the MAPMT tests, The main difference is the size which may require a larger darkbox.

### 5.6.3 Readout Electronics

The Syracuse group is responsible for developing the front-end readout for the photo-detectors, up to, but not including, the data combiner board. The Syracuse group has been collaborating with IDE AS Norway to produce readout chips for the MAPMTs and HPDs. The readout electronics have gone through two iterations of development, and it is likely that this version of the hybrid will satisfy our needs. Each board received from IDE AS Norway will undergo a set of functionality tests at Syracuse. The tests will be performed at clocking rates of 132, 264 and 396 ns, corresponding to three possible bunch spacings of the Tevatron. A database will be established which holds the information on all the boards/channels in the system ( $\sim 165,000$  channels). A photograph of the electronic test station is shown in Fig. 5.53

The QA tests for MAPMT (or HPD) and PMT electronics include:

- Noise test: Each board will be connected to a spare photo-detector and we will measure the count rate per channel at the nominal threshold when no signal is applied. The noise rate will be required to be less than 1% at this threshold.
- Dead channels: For each board, we will determine how many channels are dead and which ones. The number of dead channels is required to be less than 2%. The list of dead channels for each board will be stored in the electronic logbook so that we can track each board's history.
- Threshold scan: For each board, we will perform a threshold scan. The results should be consistent with expectations that each channel becomes 100% efficient at the nominal threshold.

### 5.6.4 Mirror Tile testing

The critical tests of mirror quality are that the radius of curvature and spot size are within specifications. A description of these tests are given in section 5.4.3. The mean radius of all mirror tiles must lie  $697 \pm 3$  cm, and the maximum shift of any tile from the mean is allowed to be within  $\pm 3$  cm. We also demand that the spot size is less than 2.5 mm. Simulations show that with this spot size requirement, the loss in Cherenkov angle resolution is less than 5%. For each mirror, we will also perform a Ronchi Test, as described in section 5.4.3. As shown in Fig. 5.37, an undistorted mirror will yield an image of the mirror with a vertical pattern. Lines bowing inward or outward indicate that the mirror is parabolic or too flat. A visual inspection of the Ronchi pattern will be performed and a digital image will be

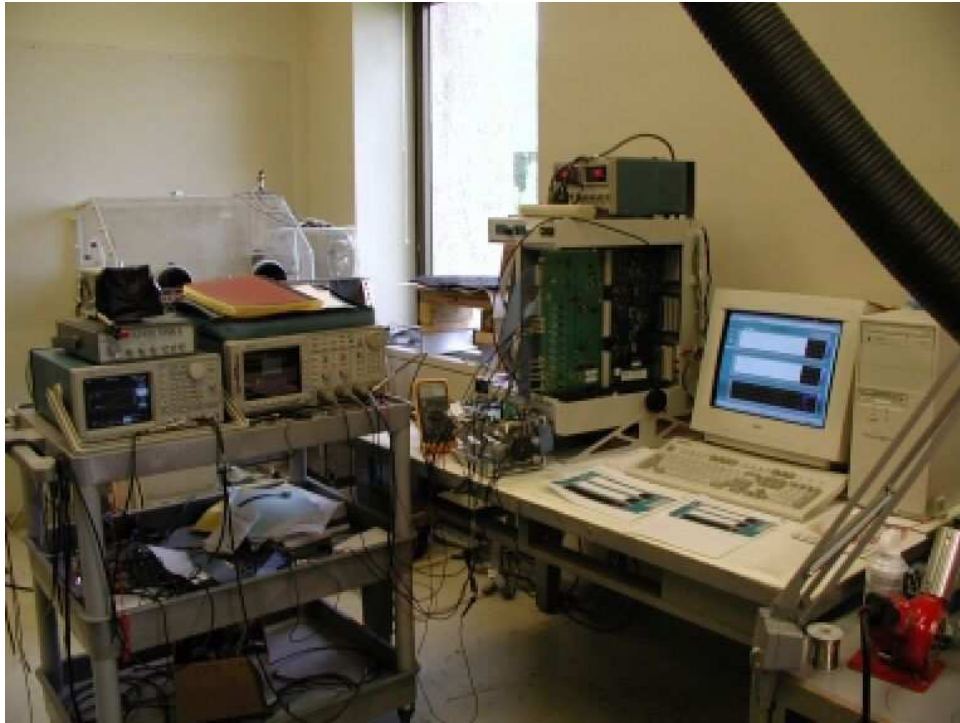


Figure 5.53: Test-stand at Syracuse University for testing front-end electronics.

recorded for each mirror tile and stored in an electronic database. We may also choose to perform a Shack Hartman test on each tile, which can be used to measure the small mirror distortions. In our request for quotations, we have asked that each mirror tile be tested using a Shack Hartman sensor. These measurements can then be used in RICH simulations and Cherenkov angle reconstruction.

We also require that the mirror to have an average reflectivity of  $\geq 90\%$ . The average reflectivity will be measured by scanning a collimated light source over the surface of the mirror and comparing the light yield collected by a PMT to the value obtained in the absence of the mirror.

### 5.6.5 Liquid and Gas Radiators

Syracuse University and Fermilab will be responsible for the design, procurement, assembly and testing of the gas and liquid radiators. This includes all the accessories, including monitoring devices and controls. Syracuse will be responsible for all aspects of transmission tests on samples from several vendors. Syracuse University has available a spectrophotometer which is capable of transmission measurements down to  $\sim 150$  nm, well below our sensitive region (see Fig 5.54). The custom-built system consists of a Hamamatsu Deuterium lamp,



Oriel chopper, McPherson monochromator, Varian vacuum pump, vacuum-tight sample volume with provision for x-y movement of the sample and readout electronics. The system is driven by a Labview-based DAQ. Fermilab will provide the necessary engineering expertise for design of the vessels and the recirculation systems. The system will be reviewed by physicists and engineers from Fermilab.

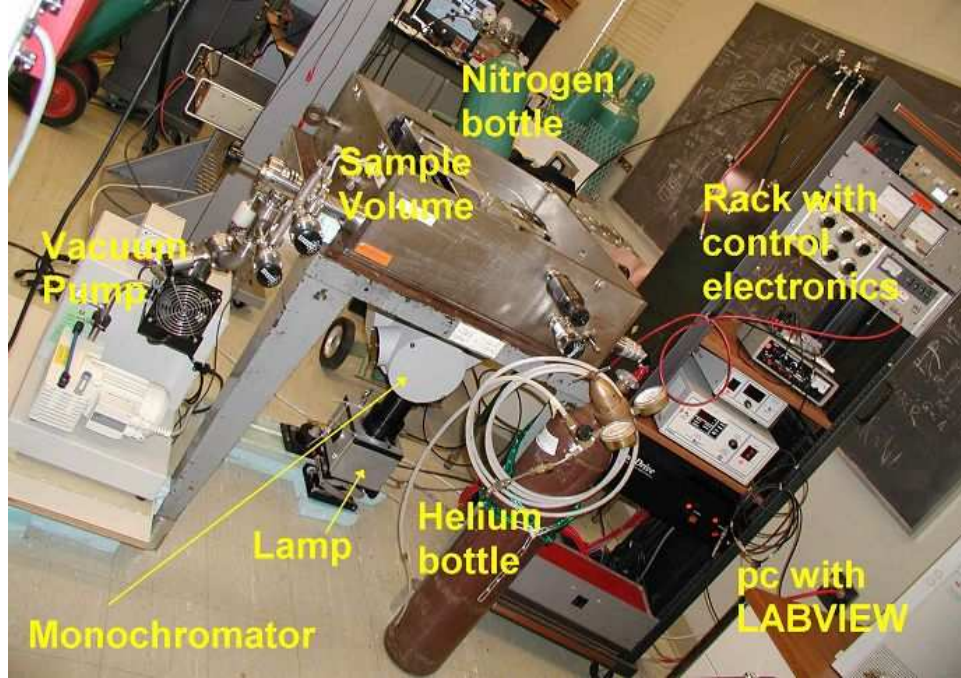


Figure 5.54: Transmission measurement setup.

### 5.6.6 Testing of High and Low Voltage Power Supplies

The power supplies will also need to be put through some rudimentary tests to ensure their reliable operation. The power supplies will be tested using a passive-load board which will provide resistive loads which are comparable to the loads they will experience during data taking. Separate boards will be produced for the low voltages ( $\sim 5\text{V}$ ), the MAPMT/PMT voltages ( $\sim 1000\text{V}$ ), and the HPD high voltages if necessary ( $\sim 20\text{ kV}$ ). These board will have jumpers or switches which will allow for different loads to be connected to the power supply. Two additional resistors,  $R_{\text{alarm}}$ , and  $R_{\text{trip}}$ , will be used to provide loads which, in the first case, should cause the power supply to go into an alarm state, and in the second, cause a power supply (PS) trip. The following tests will be performed:

- Measure the actual voltage versus the set voltage. Confirm that  $V_{\text{set}} = V_{\text{actual}}$ .



- Confirm that the readback (monitored), voltage ( $V_{mon}$ ) also agrees with  $V_{set}$ .
- Measure the current as a function of applied voltage (confirm that it's linear over the full range of the PS), *i.e.*, no sagging of the PS.
- Measure the readback (monitored) current  $I_{mon}$  as a function of the actual current ( $I_{actual}$ ).
- Confirm that the PS alarm circuitry is working properly by connecting in  $R_{alarm}$ .
- Confirm that the PS trip circuitry is working properly by connecting in  $R_{trip}$ .
- Check that the PS reset circuitry is operating properly. The reset circuitry re-enables the PS so that it may be turned back on after a trip.
- For silicon bias supply (HPD option only), measure the ripple on the 60V PS and make sure it is within specifications.
- Check that the PS is floating. The power supplies will likely be required to be floating with an optional jumper to connect the V- to ground.
- Confirm that the power supplies ramp up to the set voltage properly.
- Check that the ripple on the HPD 20 kV PS is within specification.
- Each PS will then be connected to a load board for 1 week and the output voltages and currents will be monitored for stability. The PS voltages and currents are required to be stable within specification.

### 5.6.7 High and Low Voltage Cables

- Low voltage Cabling: The primary concerns are shorted or broken lines. After terminating the cables, we will have an automatic cable-tester which indicates open or shorted lines.
- High Voltage Cabling: After cables ends are terminated we will test them at 125% of operating voltage. We will make sure there is no current draw on the cable when it is unterminated at the far end.

### 5.6.8 MAPMT and PMT Electronics Cooling System

The VA\_BTeV electronics generate enough heat that water cooling will be necessary. For MAPMTs, the voltage dividers will also need to be cooled. The single anode PMTs will also need to be water cooled. Syracuse University and Fermilab will be responsible for the design, procurement, assembly and testing of the cooling system and all the accessories,

including monitoring devices, cooling lines, and insulation. Fermilab will provide the necessary engineering expertise. The system will be reviewed by physicists and engineers from Fermilab.

## 5.7 Expected Performance of the RICH

Detailed simulations were performed to determine specifications of various detector components as well as the expected physics performance. These various simulations are discussed below.

### 5.7.1 Detector Simulations

Simulations play an important role in developing specifications for various detector components. Both the mirror system and the photodetector systems have used a simulation of the RICH detector to develop specifications and determine the expected performance. Simulation of events are generally handled using a version of GEANT (BTeVGeant) which incorporates the BTeV geometry [19]. The RICH simulation takes from GEANT the list of particles produced and generates photon hits in the photodetectors. The RICH simulation accounts for geometrical losses due to acceptance, photo-conversion and collection efficiencies of the photodetectors, optical characteristics of the radiating medium, and reflectivity of the mirrors.

Results from this simulation were used to determine that an aerogel radiator would fail to provide acceptable  $K/p$  separation, whereas a  $C_5F_{12}$  liquid radiator provides  $\geq 3\sigma$  separation (see Section 5.4.4.1). Here we discuss the usage of this simulation in developing specifications for the mirror system as well as its use in comparing different photodetector options.

#### 5.7.1.1 Mirror Simulations and Specifications

The Cherenkov angle resolution which will ultimately be achieved will depend critically on the mirror system. Each of the mirror tiles need to be uniform at a level such that all the tiles together truly focus to at the focal plane. Any errors introduced as a result of the mirrors being imperfect must not contribute significantly to the Cherenkov angle uncertainty.

The requirements on the mirror radius have been investigated by simulating an imperfect mirror system. In particular, we simulate the effects of variations in the mirror radius within a given mirror tile, as well as variations in radii between neighboring tiles. In the latter case, differences in radii can be mostly corrected for in the reconstruction by using the track's momentum and the photon's hit position to determine the most likely mirror from which a photon reflected. By using this particular mirror's radius of curvature in the particle ID likelihood (see Section 5.7.2.1), we in part take out mirror-to-mirror radius variations. Large differences in radius from the nominal value will cause the photons to be imaged in front of or behind the photodetection plane. These effects have been studied using the RICH

simulation. In the results presented here, unless otherwise noted, we use the “most likely” mirror radius in the Cherenkov angle reconstruction.

In the first study, we changed the radius of curvature to a fixed value that differs from the nominal value by an amount  $\pm\delta R$ . Figure 5.55 shows the effect on the Cherenkov angle resolution as  $\delta R$  is increased from 1 to 10 cm. The degradation in Cherenkov angle resolution does not become an issue until  $\delta R \geq 3$  cm because  $\sim 75\%$  of the time we are able to determine the correct mirror from which the photon was reflected and assign the correct radius of curvature. Beyond 3 cm, the degradation worsens because the photodetector is far from the focal plane of the mirror. These simulations lead to the requirement that the variation in mirror radii is less than  $\pm 3$  cm. A 4 cm shift variation in the nominal radius produces about a 5% change in the Cherenkov angle resolution per track.

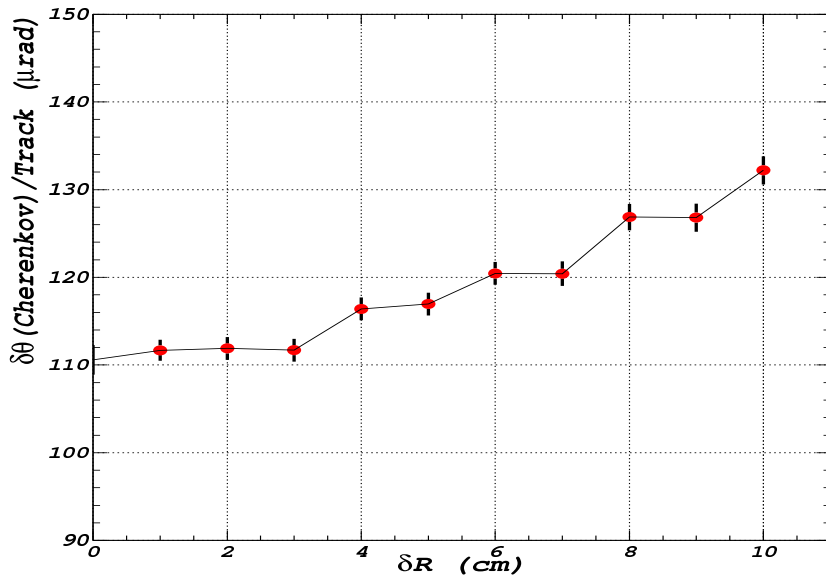


Figure 5.55: Dependence of the Cherenkov angle resolution per track on deviations of the radius of curvature  $\delta R$  from the nominal radius of 697 cm.

The effect on the Cherenkov angle resolution due to variations between neighboring tiles has also been investigated using two different methods. In the first method, we uniformly distribute tracks in a circle of radius 58 cm, so that Cherenkov photons are shared among 7 tiles (based on the default value of the hexagon side) as shown in Fig. 5.56. We then simulate random variations in mirror radii by randomly varying, event by event, the radii of the struck tiles within  $\pm\delta R$ . The effect on the Cherenkov angle resolution is shown in Fig. 5.57.

The worst case scenario occurs, when a track radiates photons which are shared by three mirrors. To probe this case, we generated tracks which pass through one of the corners of mirror #1 (corner A) as shown in Fig. 5.56. We then set the mirror radii as follows:

- Mirror #1 is held at the nominal radius  $R_{nom}$ .

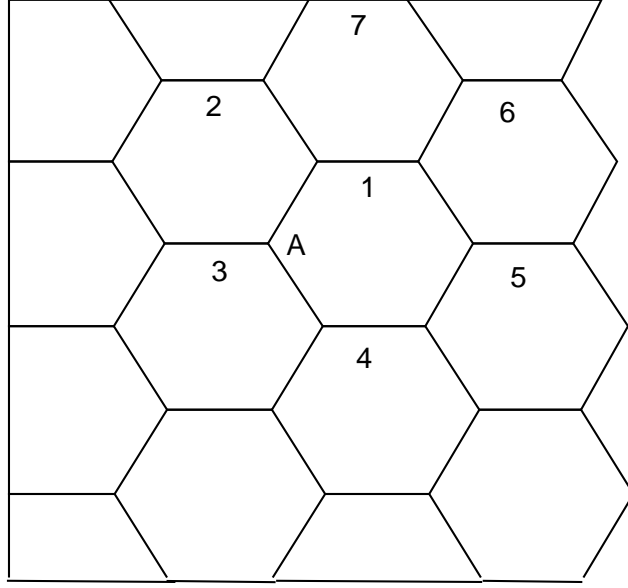


Figure 5.56: The mirror configuration used in the simulation.

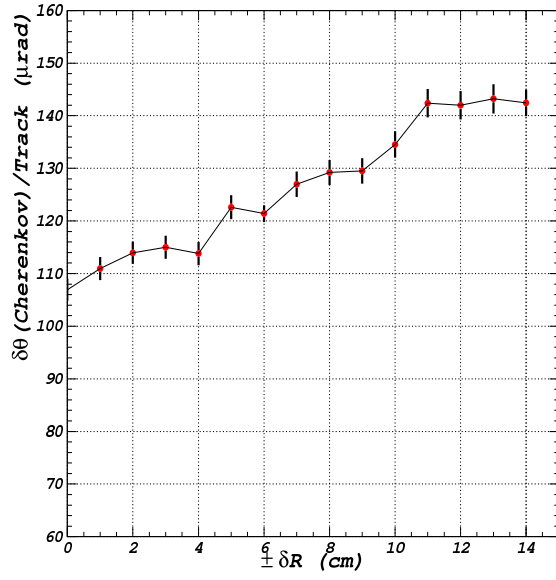


Figure 5.57: Variation of the Cherenkov angle resolution per track for a random variation of the radii of curvature for the 7 tiles.

- Mirror #2 is held at  $R_{nom} + 1$  cm.
- We vary the radius of mirror #3 by the amount  $+\delta R$ .

The effect on the Cherenkov angle resolution is shown in Fig. 5.58 (left). The first curve (squares) shows the variation of the Cherenkov angle resolution when varying the radius by an amount  $+\delta R$ , but assuming the nominal radius in the reconstruction. The second curve (circles) shows the same variation when we use the radius of the mirror which was determined by ray-tracing. It is clear that using the proper radius is extremely important.

To understand how quickly the resolution degrades when a track shares its photons with 3 mirror tiles with different radii, we simulated more extreme variations among the mirror tiles. In particular, we simulated the following configurations:

- Variation #1 (see Fig. 5.58 (right))
  - Mirror #1 is held at the nominal radius  $R_{nom}$ .
  - Mirror #2 is held at  $R_{nom} \pm 3$  cm.
  - We vary the radius of mirror #3 by the amount  $+\delta R$ .
- Variation #2 (see Fig. 5.59 (left))
  - Mirror #1 is held at the nominal radius  $R_{nom}$ .
  - Mirror #2 is held at  $R_{nom} \pm 4$  cm.
  - Radius of mirror #3 is varied by the amount  $+\delta R$ .
- Variation #3 (see Fig. 5.59 (right))
  - Mirror #1 is held at the nominal radius  $R_{nom}$ .
  - Mirror #2 is held at  $R_{nom} \pm 5$  cm.
  - Radius of mirror #3 is varied by the amount  $+\delta R$ .
- Variation #4 (see Fig. 5.60 (left))
  - Mirror #1 is held at the nominal radius  $R_{nom}$ .
  - Mirror #2 is held at  $R_{nom} \pm 6$  cm.
  - Radius of mirror #3 is varied by the amount  $+\delta R$ .
- Variation #5 (see Fig. 5.60 (right))
  - Mirror #1 is held at the nominal radius  $R_{nom}$ .
  - Mirror #2 is held at  $R_{nom} \pm 7$  cm.
  - Radius of mirror #3 is varied by the amount  $+\delta R$ .

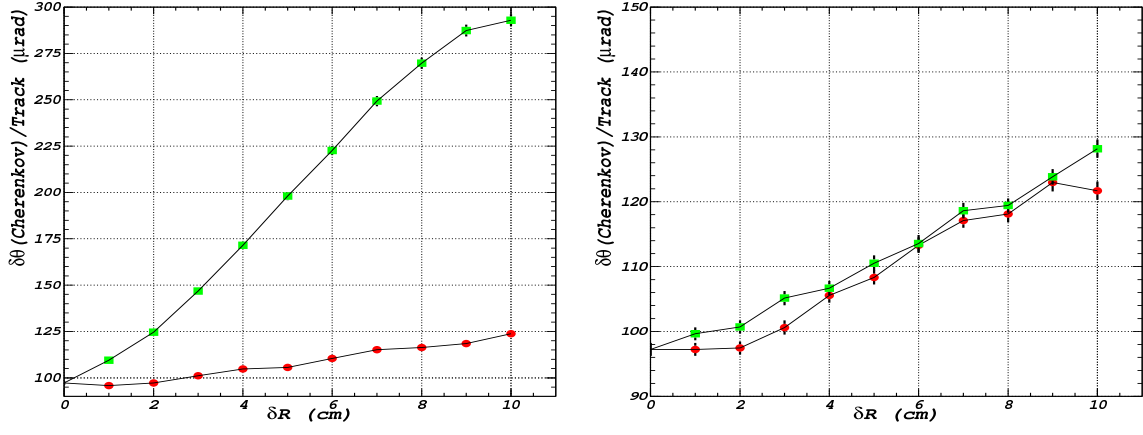


Figure 5.58: Left plot shows the variation of the Cherenkov angle resolution per track for different radii of Mirror#3. Squares show the results if we use the nominal radius (697 cm), and circles show the results when we use the inferred radius of the struck mirror tile. The right figure shows a comparison in the Cherenkov angle resolution for +3 cm (circles) and -3 cm (squares) shifts in the nominal radius (but using radius of inferred mirror tile in the reconstruction).

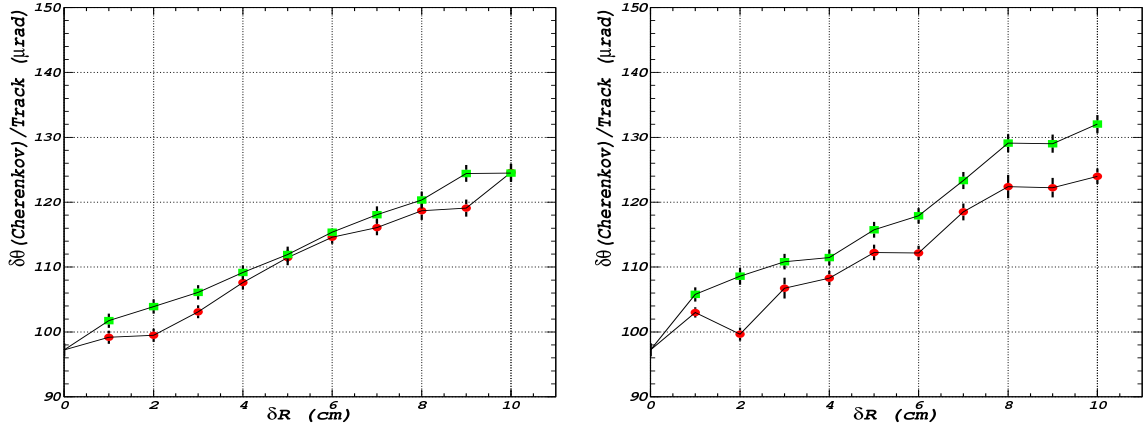


Figure 5.59: Same as in Fig. 5.58 (right), except we shift mirror #3 by  $\pm 4$  cm (left) and  $\pm 5$  cm (right).

In each of these cases, we use the radius of the mirror inferred by ray-tracing in the particle ID likelihoods. Based upon these studies, we require that all the mirror tiles have an average radius of curvature which within  $\pm 3$  cm of the nominal value.

We also investigated requirements on the *spot size*. The spot size is defined to be the diameter of the circle in which 95% of the light reflected from the entire mirror is focused. Unfortunately, a requirement on the spot size may not guarantee that the mirror's distortions can be neglected. In particular, the effect on the Cherenkov angle resolution will depend on whether the distortions are random or correlated. For instance, point-to-point correlations

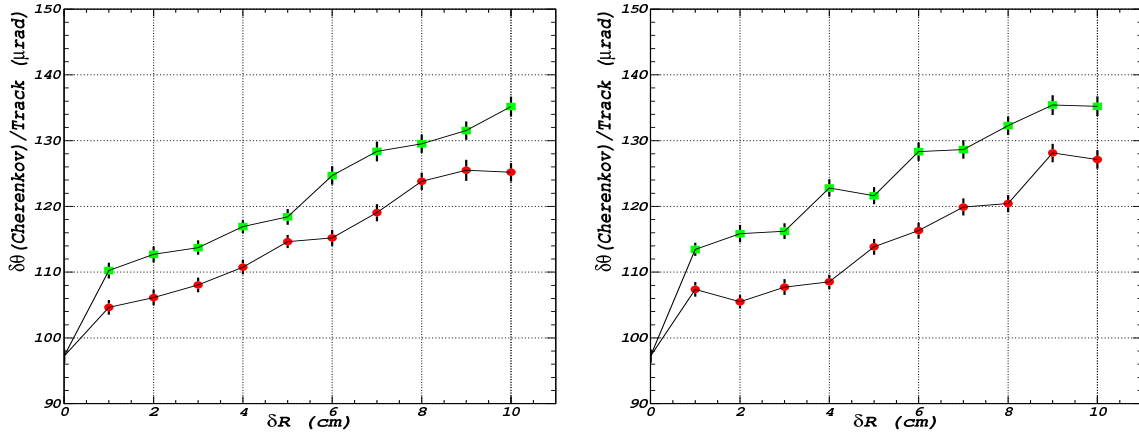


Figure 5.60: Same as in Fig. 5.58 (right), except we shift mirror #3 by  $\pm 6$  cm (left) and  $\pm 7$  cm (right).

may degrade the Cherenkov angle resolution more than similar magnitude random variations. We therefore have studied how various aberrations contribute to the spot size. In this study, we simulate the spot size the same way we measure it, that is, on-axis. The effect of the aberration is then propagated off-axis to simulate the effect on the Cherenkov angle reconstruction.

We generate a spot image using a wavefront expansion,  $W(x_m, y_m)$ , which is defined to be the difference between the real surface and the perfect spherical surface, in terms of Zernike polynomials. If we define the normalized coordinates,  $x_m$  and  $y_m$ , of the photon hit on the mirror as shown in Fig. 5.61, the deviations  $\Delta X_D$  and  $\Delta Y_D$  (see Fig. 5.62) of the photon hit on the detection plane from its ideal position (if the mirror surface was perfect) are then proportional to the derivatives of the wavefront  $W(x_m, y_m)$  via the following equations:

$$\begin{aligned}\Delta X_D &= -d \cdot \frac{\partial W(x_m, y_m)}{\partial x_m}, \\ \Delta Y_D &= -d \cdot \frac{\partial W(x_m, y_m)}{\partial y_m}.\end{aligned}\tag{5.2}$$

Here,  $d$  is the distance between the detection plane and the mirror. These deviations are used to measure both the spot size and the Cherenkov angle resolution.

The generation of the spot image using this wavefront can be done either as a random variation of the reflection angle or as a function of some specific aberrations. Figure 5.63 shows the variation of the Cherenkov angle resolution per track for different spot sizes. For random variations (filled points), there is a nearly linear correlation between Cherenkov angle uncertainty and spot size. We also show in Fig. 5.63 the simulation results of the first few Zernike terms that have non-negligible contribution to the Cherenkov angle resolution per track, see table 5.5 for a list of the Zernike terms. Shown are the effects from (mis)focusing



where,  $0 < \rho < 1$   
 $0 < \theta < 2\pi$

Figure 5.61: Definition of the normalized photon hit coordinates on the mirror.



Figure 5.62: The deviations,  $\Delta X_D$  and  $\Delta Y_D$  from the ideal image position as a result of an imperfect spherical mirror.



and spherical aberration (top left), effects of coma (upper right) and secondary astigmatism (bottom). It is observed that these correlated aberrations degrade the Cherenkov angle resolution per track more than random variations. In each figure we also show the effect of random variations. We therefore conclude that for a given spot size, random variations generally give an optimistic Cherenkov angle uncertainty. Correlated aberrations produce a significantly larger error in the Cherenkov angle for a given spot size. Although other aberrations contribute to the spot size, their effect on the Cherenkov angle resolution per track is found to be negligible. To ensure that the correlated aberrations do not degrade the Cherenkov angle resolution by more than 5%, we require that the spot size is below 2.5 mm. If the spot size is larger than 2.5 mm further analysis is required to understand the types of aberrations which exist and their contributions to the spot size. This can be done by analyzing the wavefront and determining the magnitudes of the Zernike coefficients.

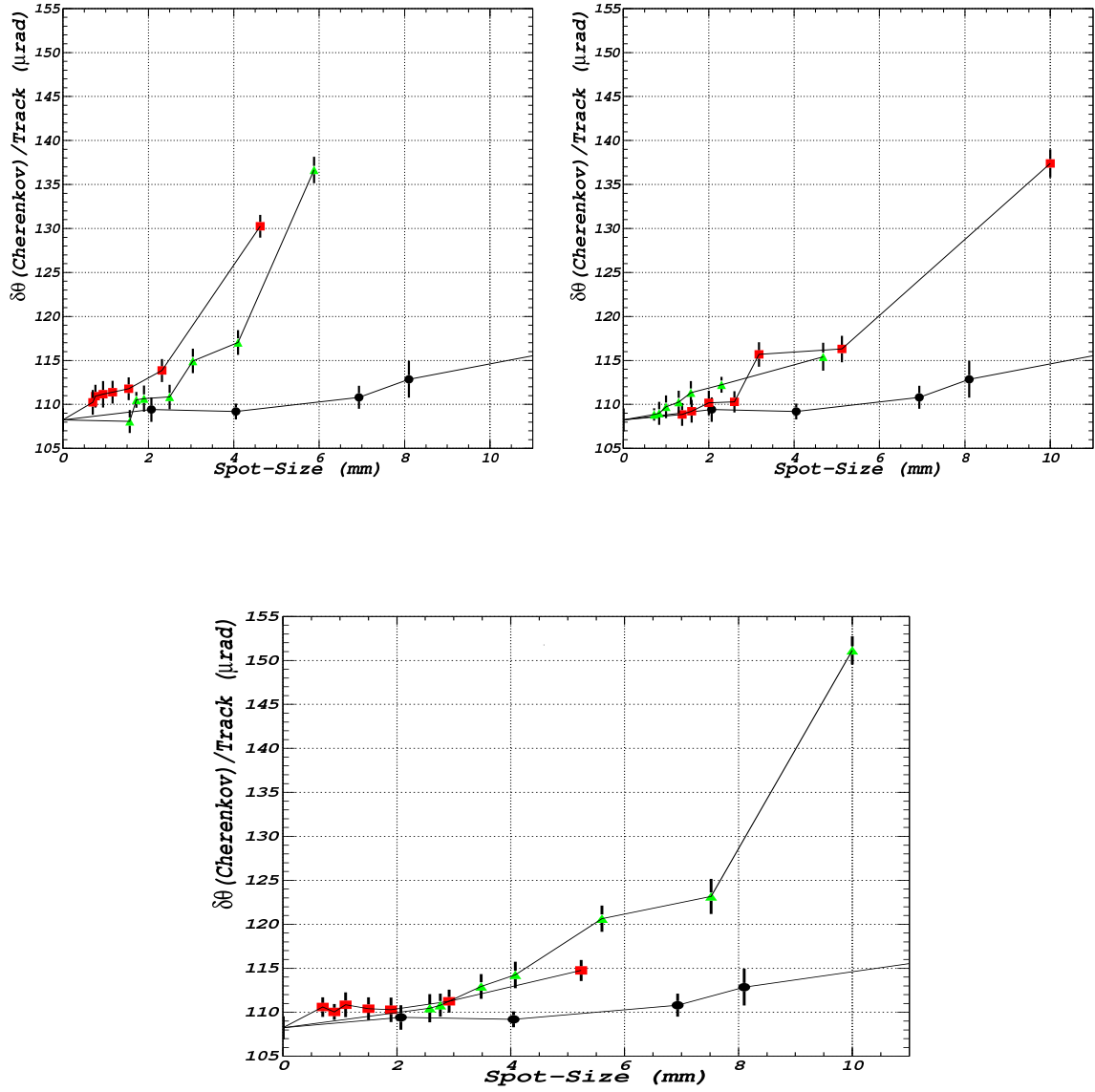


Figure 5.63: Variation of the Cherenkov angle resolution per track for different spot sizes (mm) and different aberrations. The upper left plot shows the effects of the focus term  $Z_4$  (squares) and primary spherical aberration term  $Z_9$  (triangles). Upper right plot shows the effects of the coma<sub>x</sub> term  $Z_7$  (squares) and coma<sub>y</sub> term  $Z_8$  (triangles). Bottom plot shows the effects of the secondary astigmatism<sub>x</sub> term  $Z_{12}$  (squares) and secondary astigmatism<sub>y</sub> term  $Z_{13}$  (triangles). In all plots, the circles correspond to random variations.

### 5.7.1.2 Photon Detector Simulations

The choice of photodetector (MAPMT or HPD) depends very much on performance, ease of implementation, and cost. Because of the significant improvement in the active area of MAPMTs from Hamamatsu, we have reconsidered their use for the RICH. We have simulated the BTeV RICH using both MAPMT and HPD photodetector configurations. The simulation includes all geometric effects, quantum efficiency, transmission and reflection. The simulation does not include any possible additional loss due to the imperfect magnetic shielding, but studies on this indicate that the loss will be less than 5%. In addition to simulating both the MAPMT and HPD systems, we also consider using or not using an acrylic window in front of the photon detectors. The acrylic window absorbs UV photons which would otherwise pass through the HPD's quartz window. Since UV photons suffer from large chromatic error, this degrades the resolution per photon. Even though the Cherenkov resolution per track is compensated by the increase in the number of detected photons, the pattern recognition becomes more difficult, so it is advantageous to reject the large number of poorly measured UV photons. Table 5.6 shows that the two systems provide comparable Cherenkov angle resolution (bottom line of the table).

### 5.7.1.3 Occupancy of the gas RICH photon detectors

The RICH electronic readout has to be designed keeping in mind the expected data rates in the different regions. In particular, we need to be able to read out the expected high rate of data in the most intense regions close to the beam pipe. This puts strong demands on the electronics and the speed of the readout. In the following, we simulate the expected number of photons in the HPDs for beam crossings containing 1  $b\bar{b}$  event and either 2 or 6 minimum bias events per crossing. Since the pixel size and the readout granularity are similar for the HPD and for the MAPMT options, the results are representative for the baseline choice as well. These number of minimum bias events correspond to the mean number expected at an instantaneous luminosity of  $2 \times 10^{32} \text{ cm}^{-2} \text{ s}^{-1}$  for 132 ns and 396 ns operation of the Tevatron.

Figures 5.64(a) and 5.64(b) show the mean number of hits per bunch crossing for each HPD in the HPD array. Each tower corresponds to a single HPD. The real HPD array is of course a hexagonal close-packed array but this representation is chosen for ease of display.

Figures 5.65(a) and 5.65(a) show the distribution of the number of hits in a bunch crossing summed over the 10 hottest HPDs in the HPD array. The HPDs have a mean of 17.5 photons per bunch crossing with an RMS of 16.6 and a maximum of 97 photons, when the luminosity corresponds to 2 interactions per bunch crossing. The same numbers at a luminosity corresponding to 6 interactions per bunch crossing are 51.2, 23.9 and 130 photons per bunch crossing.

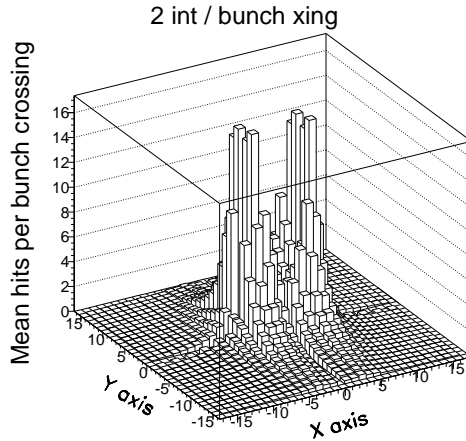
Figures 5.66(a) and 5.66(a) show the distribution of the number of hits in a bunch crossing summed over the 10 HPDs in the HPD array with “medium” activity. Here, we define “medium” as an average of one-third the mean activity of the hottest 10 HPDs. These HPDs have a mean of 5.9 photons per bunch crossing with an RMS of 7.2 and a maximum

| Zernike Coefficients | Radial   | Angular         |
|----------------------|--|-----------------|
| $Z_1$                | 1.0  | 1.0             |
| $Z_2$                | $\rho$   | $\cos(\theta)$  |
| $Z_3$                | $\rho$   | $\sin(\theta)$  |
| $Z_4$                | $2\rho^2 - 1$  | 1.0             |
| $Z_5$                | $\rho^2$   | $\cos(2\theta)$ |
| $Z_6$                | $\rho^2$   | $\sin(2\theta)$ |
| $Z_7$                | $(3\rho^2 - 2)\rho$                                      | $\cos(\theta)$  |
| $Z_8$                | $(3\rho^2 - 2)\rho$                                      | $\sin(\theta)$  |
| $Z_9$                | $6\rho^4 - 6\rho^2 + 1$                                  | 1.0             |
| $Z_{10}$             | $\rho^3$   | $\cos(3\theta)$ |
| $Z_{11}$             | $\rho^3$   | $\sin(3\theta)$ |
| $Z_{12}$             | $(4\rho^2 - 3)\rho^2$                                    | $\cos(2\theta)$ |
| $Z_{13}$             | $(4\rho^2 - 3)\rho^2$                                    | $\sin(2\theta)$ |
| $Z_{14}$             | $(10\rho^4 - 12\rho^2 + 3)\rho$                          | $\cos(\theta)$  |
| $Z_{15}$             | $(10\rho^4 - 12\rho^2 + 3)\rho$                          | $\sin(\theta)$  |
| $Z_{16}$             | $20\rho^6 - 30\rho^4 + 12\rho^2 - 1$                     | 1.0             |
| $Z_{17}$             | $\rho^4$   | $\cos(4\theta)$ |
| $Z_{18}$             | $\rho^4$   | $\sin(4\theta)$ |
| $Z_{19}$             | $(5\rho^2 - 4)\rho^3$                                    | $\cos(3\theta)$ |
| $Z_{20}$             | $(5\rho^2 - 4)\rho^3$                                    | $\sin(3\theta)$ |
| $Z_{21}$             | $(15\rho^4 - 20\rho^2 + 6)\rho^2$                        | $\cos(2\theta)$ |
| $Z_{22}$             | $(15\rho^4 - 20\rho^2 + 6)\rho^2$                        | $\sin(2\theta)$ |
| $Z_{23}$             | $(35\rho^6 - 60\rho^4 + 30\rho^2 - 4)\rho$               | $\cos(\theta)$  |
| $Z_{24}$             | $(35\rho^6 - 60\rho^4 + 30\rho^2 - 4)\rho$               | $\sin(\theta)$  |
| $Z_{25}$             | $70\rho^8 - 140\rho^6 + 90\rho^4 - 20\rho^2 + 1$         | 1.0             |
| $Z_{26}$             | $\rho^5$   | $\cos(5\theta)$ |
| $Z_{27}$             | $\rho^5$   | $\sin(5\theta)$ |
| $Z_{28}$             | $(6\rho^2 - 5)\rho^4$                                    | $\cos(4\theta)$ |
| $Z_{29}$             | $(6\rho^2 - 5)\rho^4$                                    | $\sin(4\theta)$ |
| $Z_{30}$             | $(21\rho^4 - 30\rho^2 + 10)\rho^3$                       | $\cos(3\theta)$ |
| $Z_{31}$             | $(21\rho^4 - 30\rho^2 + 10)\rho^3$                       | $\sin(3\theta)$ |
| $Z_{32}$             | $(56\rho^6 - 105\rho^4 + 60\rho^2 - 10)\rho^2$           | $\cos(2\theta)$ |
| $Z_{33}$             | $(56\rho^6 - 105\rho^4 + 60\rho^2 - 10)\rho^2$           | $\sin(2\theta)$ |
| $Z_{34}$             | $(126\rho^8 - 280\rho^6 + 210\rho^4 - 60\rho^2 + 5)\rho$ | $\cos(\theta)$  |
| $Z_{35}$             | $(126\rho^8 - 280\rho^6 + 210\rho^4 - 60\rho^2 + 5)\rho$ | $\sin(\theta)$  |

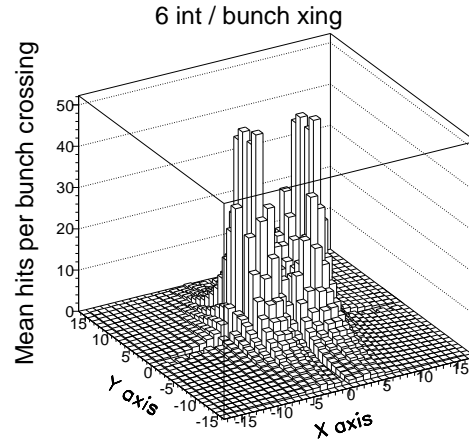
Table 5.5: Wavefront expansion in terms of Zernike's coefficient.

Table 5.6: Results on the Cherenkov angle resolution (in mrad) from simulations of the MAPMT and HPD systems. We consider two cases: on the left we show the scenario where we use an acrylic window in front of the photon detectors (baseline) and on the right we show the results when the acrylic window is absent.

| Resolution Type                  | Resolution (mrad) with Acrylic Window |       | Resolution (mrad) without Acrylic Window |       |
|----------------------------------|---------------------------------------|-------|--|-------|
|                                  | HPD                                   | MAPMT | HPD                                      | MAPMT |
| Total $\sigma_\theta$ per photon | 0.84                                  | 0.83  | 1.46                                     | 0.88  |
| Segmentation Error               | 0.45                                  | 0.51  | 0.45                                     | 0.51  |
| Chromatic Error                  | 0.52                                  | 0.44  | 1.42                                     | 0.51  |
| Emission Point Error             | 0.49                                  | 0.49  | 0.49                                     | 0.49  |
| Recon #Photons/Track             | 50.3                                  | 52.0  | 161.8                                    | 61.8  |
| Total $\sigma_\theta$ per track  | 0.118                                 | 0.115 | 0.116                                    | 0.111 |



(a)



(b)

Figure 5.64: The mean number of hits per bunch crossing in each HPD.

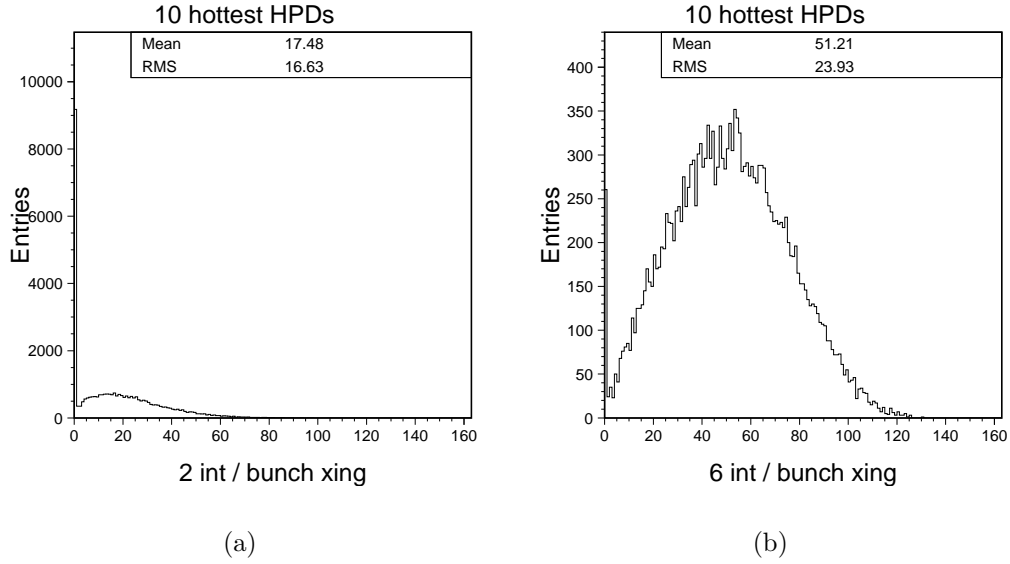


Figure 5.65: The distribution of the number of hits in a bunch crossing summed over the 10 hottest HPDs in the HPD array.

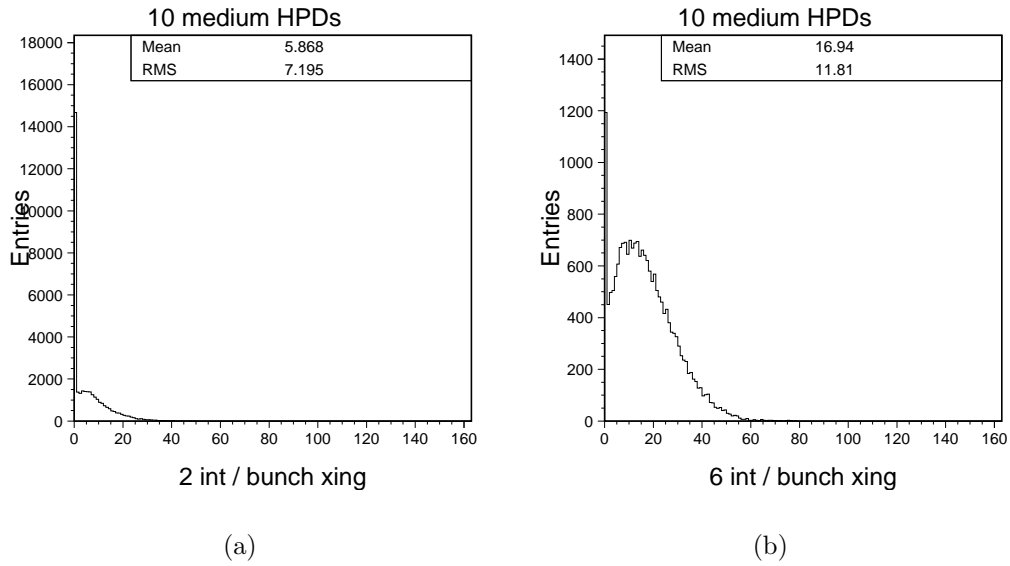


Figure 5.66: The distribution of the number of hits in a bunch crossing summed over a set of 10 HPDs with “medium” activity. These have an activity of 0.33 times the average activity of the 10 hottest HPDs.

of 58 photons, when the luminosity corresponds to 2 interactions per bunch crossing. The same numbers at a luminosity of 6 interactions per bunch crossing result in a mean of 16.9 photons, an RMS of 11.8 photons and a maximum of 78 photons per bunch crossing.

#### 5.7.1.4 Simulations of Data Readout

The RICH HPDs are grouped into 6-HPD modules. In total there are about 150 such modules in the entire RICH detector. Modules at the edge of HPD arrays may only contain 4 or 5 HPDs. Signals from HPDs in a single module are passed from the front end hybrids to a Front End Multiplexer (FEM) board, and then transmitted  $\sim 10$ -20 meters to a Data Combiner Board (DCB) via copper cables.

The high event rate requires that these cables transfer data at very high speed. The baseline design uses high speed point to point differentially driven serial lines. Each cable contains 4 twisted pairs. They provide for a reference clock (refclk) of 7.5 MHz, a beam crossing time and control data line (T/C link), and two pairs for event data. Each pair transfers data at 63.6 MByte/s and the data is encoded in the 8B10B format to balance the current.

The expected occupancy of the HPD has a strong dependence on location in the detector (see Section 5.7.1.3). We simulate the occupancy using BTeVGeant with two interactions per bunch crossing. The highest occupancy HPD module registers  $\sim 57$  hits per bunch crossing on average, whereas the mean number of hits per module is 6.8. The electronics of the HPD readout is expected to have a noise level below 1%. Assuming a 1% noise occupancy, the mean numbers of hits are 66 per bunch crossing for the highest-occupancy module and 16.4 when averaged over all modules.

The total number of bits to be transferred includes 18 bits per hit to uniquely identify an HPD (or MAPMT) channel and 2-3 additional words to indicate the event ID or bunch crossing number. The non-uniformity of the occupancy distribution across the detector implies a location-dependent number of readout cables. Some areas may require as few as 2, whereas the highest-occupancy areas may require as many as 11. Taking into account data transfer speeds, we estimate that 458 of such cables are needed to move data in the RICH HPD system, which includes a 20% overhead.

With this cable arrangement, we study the data flow between the FEMs and DCBs. We randomly pick up events from of a pool of 14,000 events fully simulated using BTeVGeant (with 1% noise). Each FEM is assumed to have an 128-Kbit FIFO memory chip. We simulated 10 million successive bunch crossings and observe no memory overflow. The final size may be much bigger than this if necessary.

Since the Tevatron accelerator will continue to run with 396 ns between beam crossings (mean of 6 interactions per crossing at  $\mathcal{L} = 2 \times 10^{32} \text{ cm}^{-2}\text{s}^{-1}$ ), we simulated this scenario as well. This reduces the burden on data transfer, assuming the noise level remains at 1%. For some of the low occupancy groups, 1 readout cable per group will be enough to transmit the data in a single crossing. In total we estimate that we will need 324 such cables for the

RICH HPD system. Once we gain test-beam experience with the HPDs and MAPMTs, we will refine these estimates.

## 5.7.2 Signal Simulations

Simulations of detector design must ultimately feed into simulations of physics signals. Here we present studies that have been performed to demonstrate the effectiveness of the RICH detector. For further physics simulations, see Part 2 in the BTeV Proposal Update [16]. For historical reasons, all simulations are run at 2 interactions/crossing. For one of the critical decay modes, we compare the RICH performance at 2 and 6 interactions per crossing. It should be realized that 6 interactions/crossing is only the starting value, with the average rate closer to 3 interactions/crossing.

### 5.7.2.1 Tagging Performance

In addition to the issue of resolution, the performance of the RICH will depend on other details such as occupancy and the degree to which Cherenkov rings overlap. A realistic simulation of efficiency and fake rates must take into account ambiguities in track-photon assignment. Since photons from the liquid radiator and the gas radiator fall on separate sensor arrays, the Cherenkov rings from the two radiators do not produce additional ambiguity in the pattern recognition.

We have analyzed simulated data with an algorithm which could be applied to real data. The reconstruction is performed in two steps. In the first pass, all hits within  $\pm 3\sigma$  of a mass hypothesis are included in the per track average, excluding those hits which are within  $\pm 3\sigma$  of the pion hypothesis for any other track. The second pass is essentially the same except that instead of assuming that all tracks are pions in the hit exclusion, the most likely mass hypotheses based on the first-pass results are used. To discriminate between two mass hypotheses for the same track (e.g.  $K$  or  $\pi$ ) we compute the likelihood ratio expressed as a  $\chi^2$  difference:

$$\Delta\chi_{K\pi}^2 = -2\log(L_\pi/L_K) \quad (5.3)$$

with,

$$L_h = P(N_h|N_h^{exp}) G(\theta_{trk\ h}|\theta_h^{exp}). \quad (5.4)$$

Here  $P(N_h|N_h^{exp})$  is the Poisson probability for observing  $N_h$  photons within  $\pm 3\sigma$  of this hypothesis when  $N_h^{exp}$  are expected, and  $G(\theta_{trk\ h}|\theta_h^{exp})$  is the Gaussian probability density for obtaining the Cherenkov angle (per track)  $\theta_{trk\ h}$  for given mass hypothesis  $h$  when  $\theta_h^{exp}$  is expected. The expected photon yield includes acceptance corrections and losses due to the Cherenkov ring overlaps. For a given cut value on the  $\Delta\chi_{K\pi}^2$  we obtain values for efficiency and fake rate.

To illustrate the performance of the  $C_4F_{10}$  system we show in Fig. 5.67 (left) the simulation of  $B_d \rightarrow K^\pm\pi^\mp$  background rejection as a function of  $B_d \rightarrow \pi^+\pi^-$  efficiency, and in



Fig. 5.67 (right) the efficiency for detecting the  $K^-$  in the decay  $B_s \rightarrow D_s^+ K^-$  versus the rejection of the  $\pi^-$  in the decay  $B_s \rightarrow D_s^+ \pi^-$ . These simulations include photon conversions and other backgrounds. We see that high efficiencies can be obtained with excellent rejection rates.

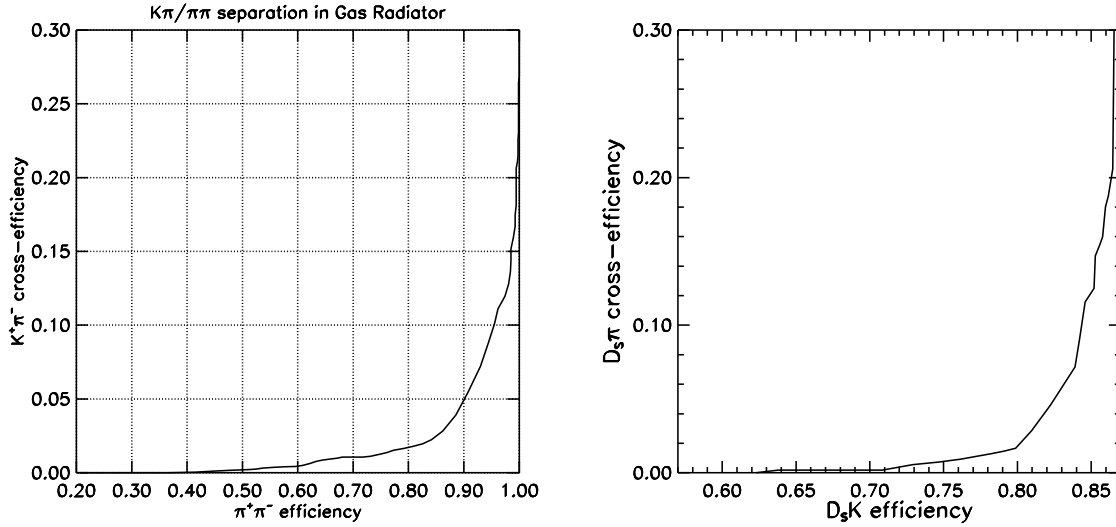


Figure 5.67: (left) Cross-efficiency of particle identification system for  $B_d \rightarrow K^\pm \pi^\mp$  as a function  $B_d \rightarrow \pi^+ \pi^-$  PID efficiency. (right) The efficiency to detect the fast  $K^-$  in the reaction  $B_s \rightarrow D_s^+ K^-$  versus the rate to misidentify the  $\pi^-$  from  $B_s \rightarrow D_s^+ \pi^-$  as a  $K^-$ . The efficiencies are defined relatively to number of events with both tracks entering the RICH detector. The Monte Carlo simulation included on average two minimum bias interactions in addition to the  $b\bar{b}$  production.

The gas radiator will also play a significant role in lepton identification as electrons below 22 GeV/c and muons below 15 GeV/c are separated by more than  $4\sigma$  from pions. Since the RICH acceptance is much larger than the calorimeter and muon system a great deal of efficiency is added.

To demonstrate the performance of the liquid radiator, we have analyzed Monte Carlo samples of  $b\bar{b}$  events to determine the efficiency and misidentification probability for kaons with momenta less than 9 GeV/c. These are significant in kaon flavor tagging because of the large number of protons which are produced at the interaction point. Background cross-efficiency, in this case the identification of a proton as a kaon, is plotted as a function of kaon efficiency in Fig. 5.68. Again, we find that high efficiencies are obtained with relatively low fake rates.

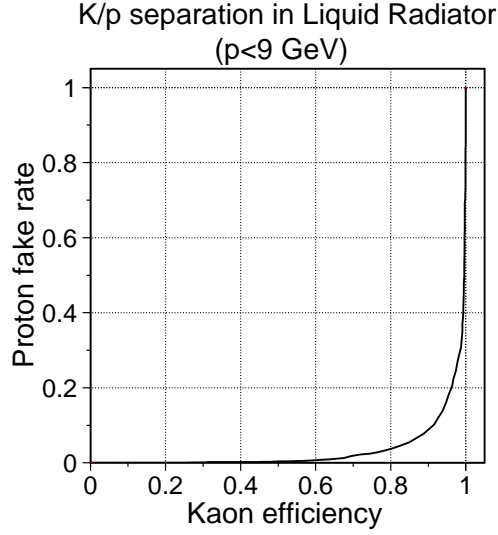


Figure 5.68: Proton fake-rate as a function of kaon identification efficiency for tracks with momenta  $<9$  GeV/c.

### 5.7.2.2 Simulations at 2 and 6 Interactions per Crossing

Simulations in the original BTeV proposal [13] were done assuming a luminosity of  $2 \times 10^{32} \text{ cm}^{-2} \text{ s}^{-1}$  with a 132 ns bunch crossing interval, which corresponds to a Poisson mean of 2 interactions per bunch crossing. Current plans are [17] that the Tevatron will run with a bunch spacing of 396 ns, corresponding to 6 interactions per bunch crossing. Examples of detected Cherenkov images for 6 minimum bias events added to a  $b\bar{b}$  event are shown in Figs. 5.69-5.70. The effect of this change in running conditions has been simulated and compared to the original assumption of 2 interactions per bunch crossing.

To investigate this, we considered the decay  $B_S \rightarrow D_S^\pm K^\mp$ ,  $D_S \rightarrow \phi\pi$ ,  $\phi \rightarrow K^+ K^-$  as a benchmark physics state needing good performance from the RICH for  $K - \pi$  separation to measure the CKM angle  $\gamma$  (and possible time-dependent CP violating effects).

This decay has three charged kaons and one charged pion in the final state. We require positive identification of the kaon from the  $B_S$  and at least one of the two kaons from the  $\phi$  decay. The analysis is identical to that in the proposal [13], with the addition of the charged particle identification by the RICH.

We generated signal and minimum bias events using Pythia [18]. The only requirements for the signal events were that the 4 tracks (3 kaons and 1 pion) were in the BTeV detector acceptance ( $10 \text{ mrad} \leq \theta < 300 \text{ mrad}$ ) and the  $D_S$  decay length was greater than 1 cm. These events are then passed through the BTeVGeant detector simulation package. Different simulations corresponding to exactly 0, 1, 2, ..., 10 minimum bias events per signal event were performed, and each was analyzed separately.

We look to quantify the change in the RICH performance in going from a mean of 2 interactions per crossing to 6 interactions per crossing. One important measure is to compare the difference in the negative log-likelihoods for the kaon and pion hypotheses ( $\chi_K^2 - \chi_\pi^2$ ) for the kaons and pions in the decay  $B_S \rightarrow D_S^\pm K^\mp$ . These log-likelihoods are shown in

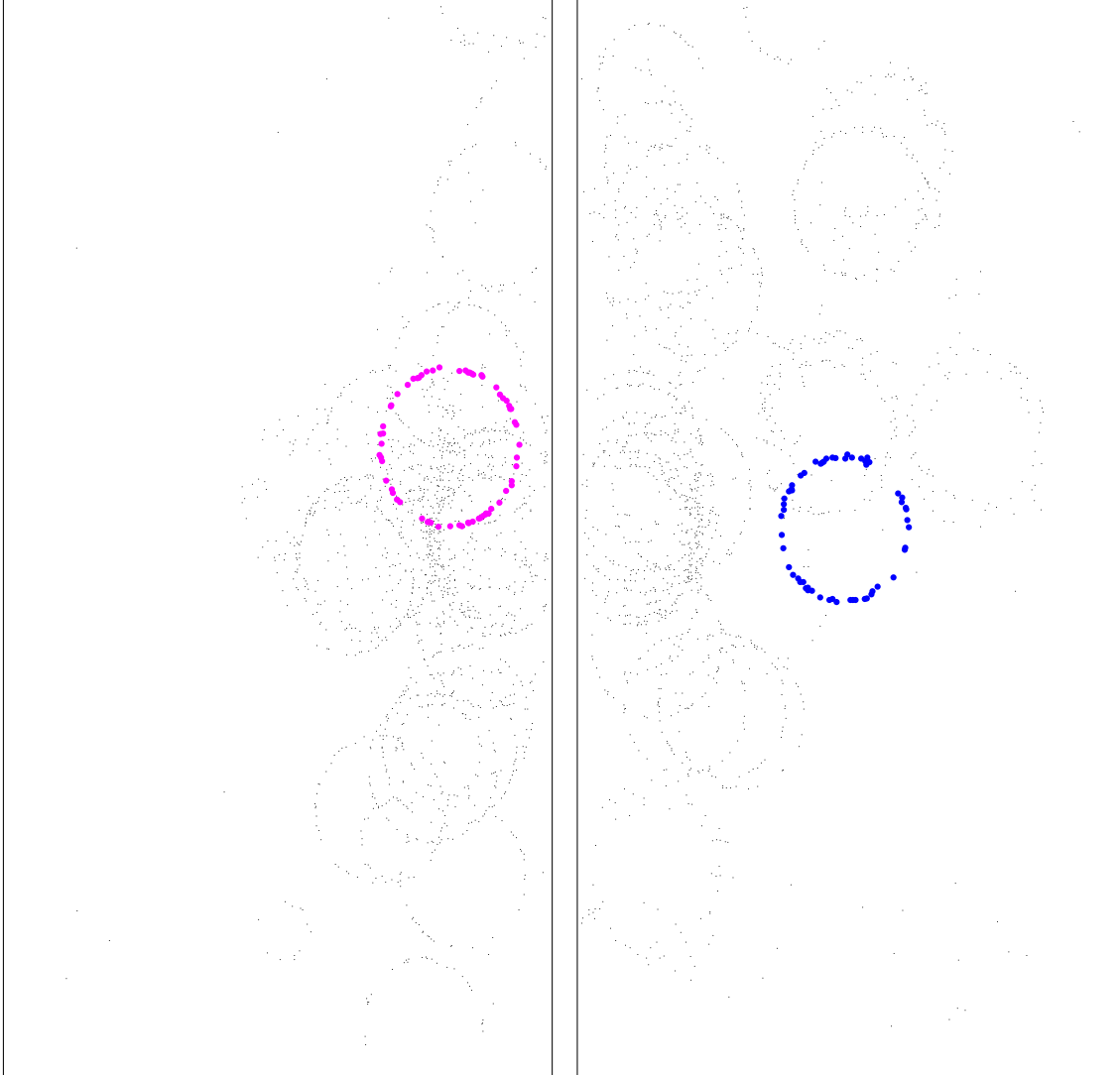


Figure 5.69: Cherenkov rings from the gas radiator detected in the HPD arrays as simulated for a  $B \rightarrow \pi^+\pi^-$  event with six minimum bias interactions in the same bunch crossing. The Cherenkov hits for the pions from the  $B$  decay are highlighted. Compare with Fig. 5.2 for two minimum-bias interactions.

Fig. 5.71(a) for 0, 1, 2 minimum bias events per bunch crossing and Fig. 5.71(b) for 7, 8, 9 minimum bias interactions per bunch crossing.

It is clear that separation between kaons and pions is degraded as the number of minimum bias events becomes large. The above chi-squared plots can be converted into an efficiency vs fake rate curve as shown in Fig. 5.72. In addition, a few of the other distributions were studied and two of them – the reconstructed  $B_S$  and  $D_S$  masses are shown in Figs. 5.73(a) and 5.73(b).

To determine the effect on the RICH tagging, we weight the events containing different numbers of minimum bias events according to Poisson distributions with means of 2.0 and

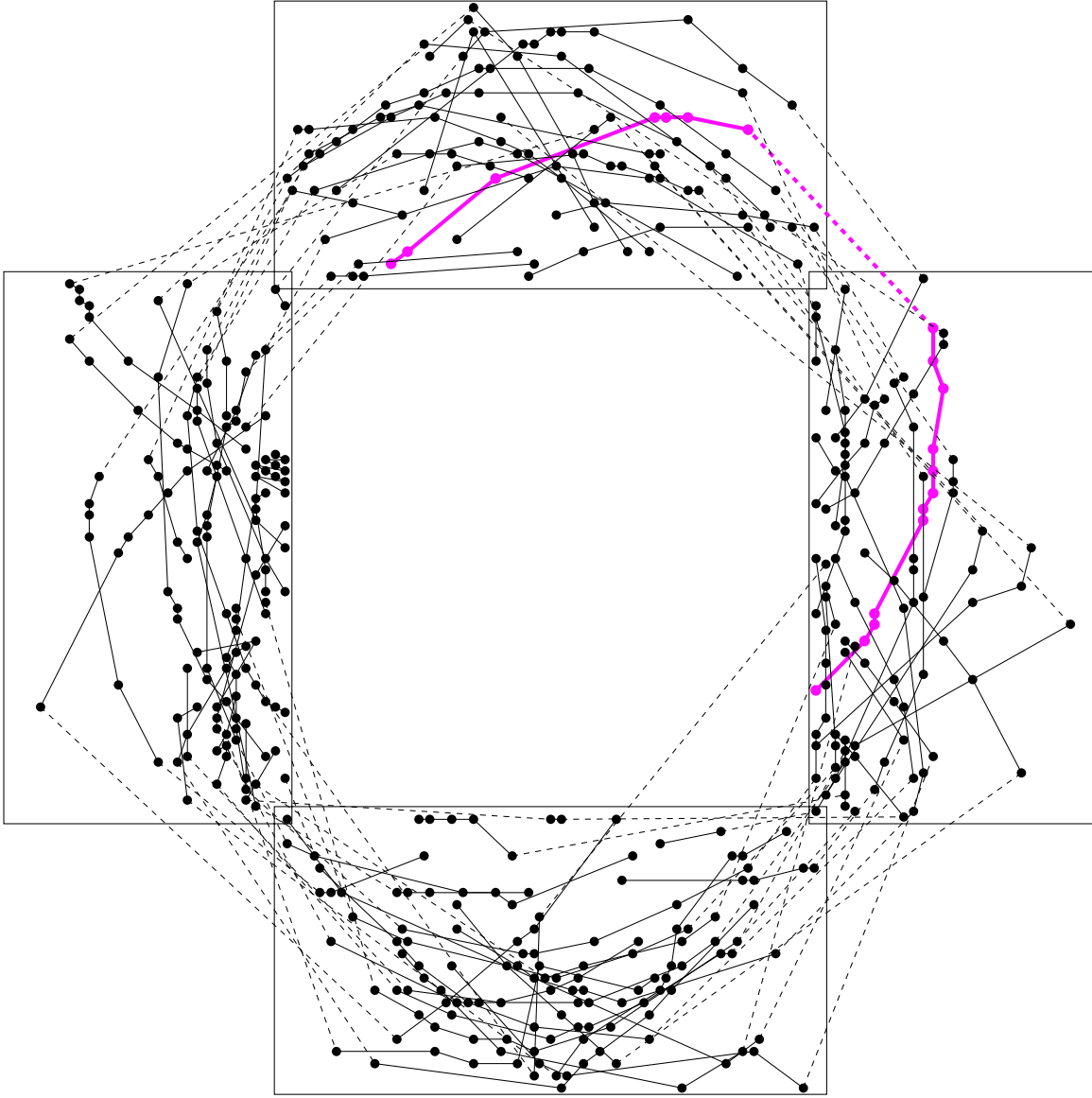


Figure 5.70: Cherenkov rings from the liquid radiator detected in the PMT arrays as simulated for a kaon tagged  $B$  event with six minimum bias in the same bunch crossing. Hits belonging to the same track are connected. The Cherenkov hits for the tagging kaon are connected by a thick line. Compare with Fig. 5.3 for two minimum-bias interactions.

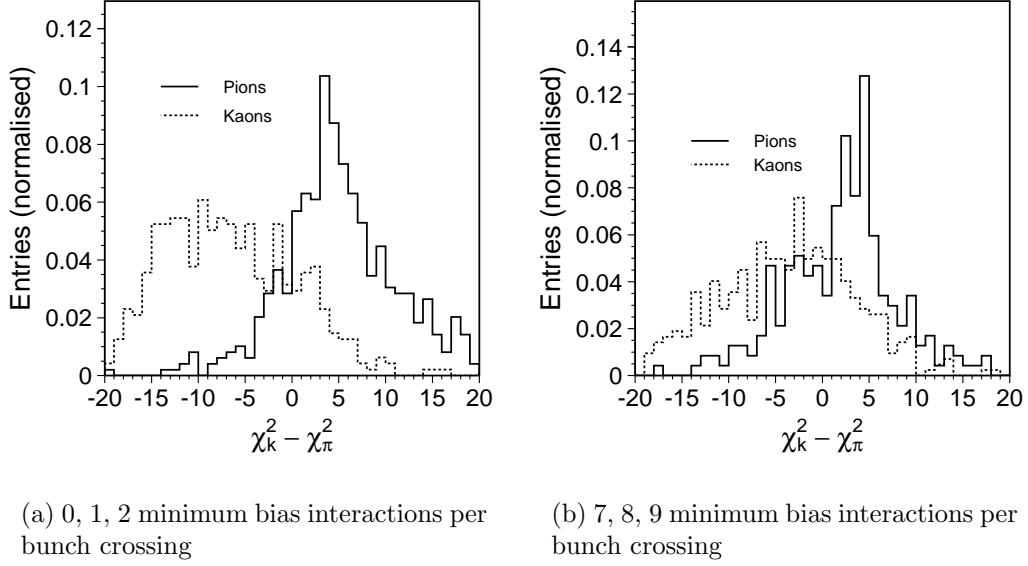


Figure 5.71:  $\chi_K^2 - \chi_\pi^2 \rightarrow$  The difference in the negative log-likelihoods for the kaon and pion hypotheses.

6.0 interactions per bunch crossing. Let us define  $\epsilon_{imin}$  to be the efficiency for tagging both the kaon from the  $B_s$  decay and at least one of the kaons from the  $\phi$  decay for a given value of  $imin$ , the number of minimum bias events per signal event in the sample. These efficiencies are normalized to the case of  $imin = 0$ . The distribution is then fit to an exponential function (of the form  $\exp(\text{constant} + \text{slope} \times x)$ ) to obtain values for  $\epsilon_{imin}$  at each value of  $imin$ . The distributions for  $\epsilon_{imin}$  are shown in Fig. 5.74(a) and Fig. 5.74(b).

To obtain efficiencies for averages of 2 and 6 interactions, we convolute  $\epsilon_{imin}$  with corresponding Poisson distributions having these mean values. Since we are primarily concerned with the change in performance in going from 2 interactions to 6 interactions per crossing on average, we compute a relative efficiency,  $\epsilon_{rel}$ , defined by:

$$\epsilon_{rel} = \frac{\sum \epsilon_{imin} * \text{Poisson}(6.0, imin)}{\sum \epsilon_{imin} * \text{Poisson}(2.0, imin)}$$

where,

$$\text{Poisson}(\mu, n) = \frac{\mu^n \exp(-\mu)}{n!}$$

After convolution, we find  $\epsilon_{rel} = 0.90$  if we require only one of the kaons from the  $\phi$  to be tagged. If we require both kaons to be tagged, we find  $\epsilon_{rel} = 0.76$ . Hence, even with a tight tagging requirement, a mean of 6 interactions per crossing still yields 76% of the value obtained for 2 interactions per crossing. We therefore conclude that the RICH will effectively separate kaons from pions, even at 6 interactions per bunch crossing. The performance is  $\sim 25\%$  better at 2 interactions per bunch crossing. Again, it is important to note that we

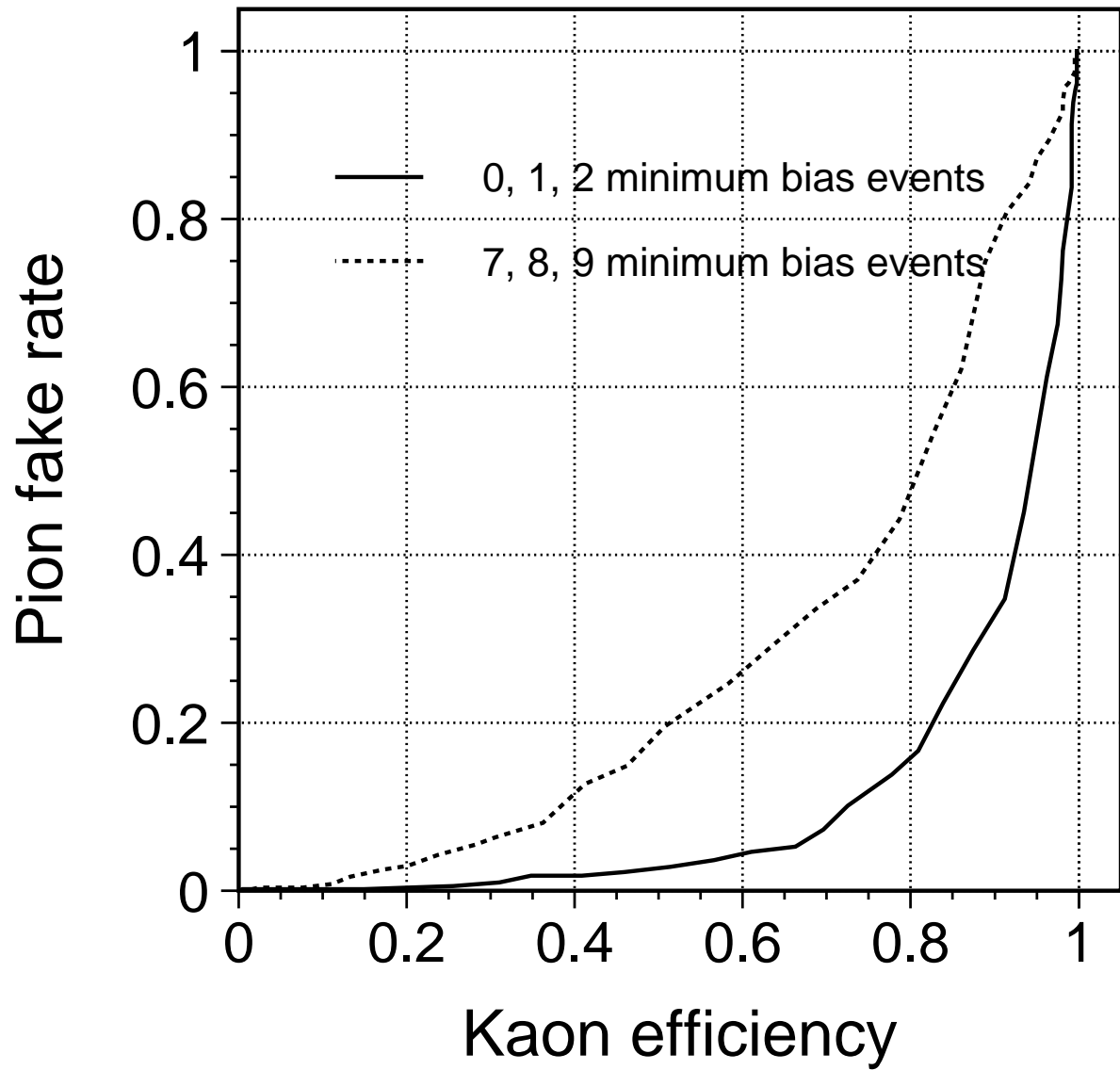


Figure 5.72: Curve for the kaon efficiency versus pion fake rate, for kaons and pions from  $B_S$  decays.

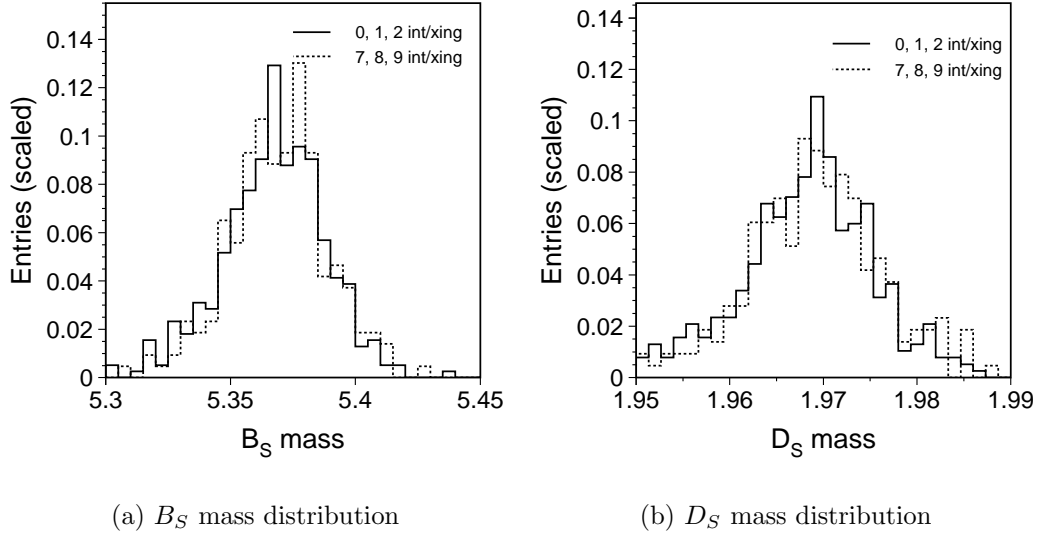


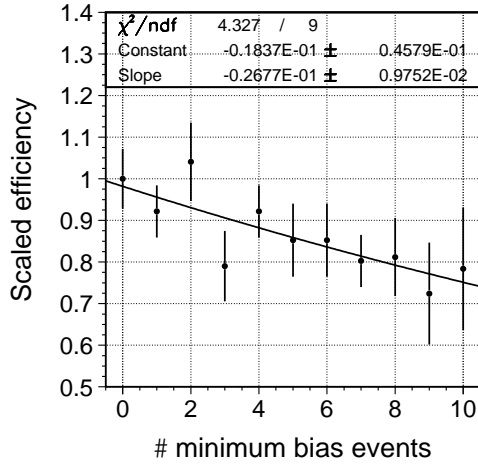
Figure 5.73: The  $B_S$  and  $D_S$  mass distributions for the selected events, after the full event reconstruction.

will only be running at 6 interactions per crossing at the beginning of the run; the average will be closer to 3 interactions per crossing, in which case we only lose 5% in relative tagging efficiency for the default analysis. Even with the more stringent requirement that both kaons from the  $\phi$  decay (as well as the kaon from the  $B_s$ ) be identified, we only incur a 12% relative loss in efficiency.

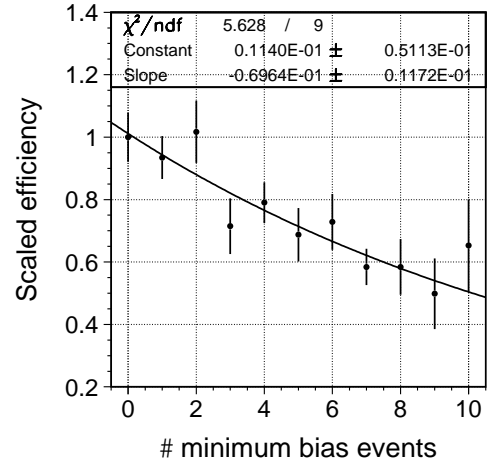
## 5.8 Cost, Schedule and Risk Analysis

### 5.8.1 RICH Risk Analysis and Management

#### 5.8.1.1 Risk Analysis



(a) At least one tagged kaon from  $\phi$  decays



(b) Both kaons from  $\phi$  decays are tagged

Figure 5.74: The scaled efficiency ( $\epsilon_{imin}$ ) distributions, both fitted to exponentials as mentioned in the text.



| WBS number | Risk Event  | Probability   | Impact  | Severity |
|------------|---|---|---|----------|
| 1.3.1.1.3  | Escalation of cost due to the single vendor of BTeV-MAPMTs.                     | Low (0.2)   | Very High (0.9)<br>MAPMT cost is approximately half of the entire RICH cost | 0.18     |
| 1.3.1      | Magnetic field distortions in HPD are larger than anticipated, if HPDs are used | Moderate (0.4)<br>Fringe fields may be underestimated. The magnetic effects on the HPD are still under study. | High (0.4)<br>Degradation of technical performance.                         | 0.16     |
| 1.3.3.1.1  | Coherent noise in HPD Front-end Hybrid too high, if HPDs are used               | Low (0.2)   | Very High (0.8)<br>Severe degradation of technical performance.             | 0.16     |
| 1.3.4.1    | Vendor fails to deliver sufficient quality, low mass mirrors at quoted cost.    | Moderate (0.3)<br>Technologies are relatively new.  | High (0.5)<br>Degradation of the technical performance.                     | 0.15     |

## Risk Listing with Mitigation Strategies

| WBS number | Risk Event   | Response/mitigation strategy   |
|------------|--|--|
| 1.3.1.1.3  | Escalation of cost due to the single vendor of BTeV-MAPMTs.                        | Fully develop HPD system as alternative.   |
| 1.3.1      | Magnetic field distortions of Cherenkov images in HPD are larger than anticipated. | <ol style="list-style-type: none"> <li>1. Use MAPMT system.</li> <li>2. Investigate significant fringe field reduction by massive external shielding plates.</li> <li>3. Simulate to which extent the distortions can be corrected for in software, possibly aided by the hardware calibration system installed inside the RICH volume.</li> </ol> |
| 1.3.3.1.1  | Coherent noise in HPD Front-end Hybrid too high in the full system tests.          | Use MAPMT system. (MAPMTs produce much larger signal pulses).  |
| 1.3.4.1    | Vendor fails to deliver sufficient quality, low mass mirrors at quoted cost.       | <ol style="list-style-type: none"> <li>1. Work with multiple vendors.</li> <li>2. Switch to more massive mirrors and accept slight degradation in calorimeter (WBS1.4) performance.</li> </ol>   |

# Bibliography

- [1] W. Adam *et al.*, Nucl. Instrum. Meth. **A343**, 60 (1994).
- [2] I. Arino *et al.*, Nucl. Instrum. Meth. **A516**, 445 (2004).
- [3] Y. Miyachi, HERMES Collaboration, Nucl. Instrum. Meth **A502**, 222 (2003); Y. Sakemi, HERMES Collaboration, Nucl. Instrum. Meth **A453**, 284 (2000); Y. Sakemi, HERMES Collaboration, Nucl. Phys. Proc. Suppl. **78**, 366 (1999); P. Carter, “Proposal for Dual Proceedings of the Third International Workshop on Ring Imaging Cherenkov Detectors, Weizmann Institute of Science, Ein-Gedi, Dead Sea, Israel, Nov. 15-20, 1998; E. Cisbani *et al.*, HERMES Internal Note 97-005.
- [4] LHC-B: RICH Technical Design Report, CERN-LHCC-2000-037; LHC-B Technical Proposal, CERN LHCC 98-4, LHCC/P4, 1998.
- [5] Hera-b gives the index of refraction as function of photon energy as

$$n - 1 = 0.0013178 + 1.723x10^{-7}E_{\gamma} + 5.495x10^{-6}E_{\gamma}^2 \quad . \quad (5.5)$$

See A. Bulla, “Die Entwicklung eines ringabbildenden Cerenkov-Zählers für den Detektor HERA-B,” Ph.D. thesis (1997). This formula is an extrapolation of measurements made at Delphi in the ultraviolet wavelength region. See E. Fokitis *et al.*, Nucl. Phys. Proc. Suppl. **B44**, 246 (1995); E. Fokitis *et al.*, Nucl. Instrum. Meth **A371**, 255 (1996).

- [6] R. Forty, CERN-PPE/96-176, Sept. 1996. Published in Proceedings of the Fourth International Workshop on B-Physics at Hadron Machines, Rome, Italy, June (1996), F. Ferroni, P. Schlein (Eds.), North-Holland, 1996.
- [7] The mirrors will be fabricated as composite sandwich structure, 12 to 25 ply facesheets and a CFRP (Continuous Fiber Re-enforced Plastic) core material. CFRP prepreg is referred to as M46J/EX-1515 material, produced from Torray M46J fibers (63 msi tensile modulus and near zero CTE) and Bryte Technologies EX-1515 cyanate ester polymer matrix.
- [8] E. Albrecht *et al.*, “Performace of Hybrid Photon Detector Prototypes with 80% Active Area for the RICH Counters of LHCb”, Nucl. Instrum. Meth. XXXX; See also GLAS-PPE-1999-22 (hep-ex/0001053) and Nucl. Instrum. Meth. Phys. Res. **A433**, 159 (1999).

- [9] R. Mountain, for the BTeV Collaboration, “Development of a Hybrid Photodiode and its Front End Electronics for the BTeV Experiment”, Presented at the Fourth International Conference on RICH Detectors, Pylos, Greece, June, 2002; Nucl. Instrum. Meth. **A502**, 183 (2003).
- [10] LHCb RICH Technical Design Report, CERN LHCC 2000-037.
- [11] M. Artuso *et. al.*, Nucl. Instrum. Meth. **A502**, 91 (2003).
- [12] F. Muheim, “Multi-Anode Photo Multipliers as Photo Detectors for Ring Imaging Cherenkov Detectors”, presented at the 4th International Workshop on Ring Imaging Cherenkov Detectors, Pylos, Greece, 5-10 June 2002.  
See <http://www.nestor.org.gr/rich2002/list/participants.htm> .
- [13] The BTeV Proposal (2000).  
See: <http://www-btev.fnal.gov/DocDB/0000/000066/002/index.html> .
- [14] J. Friese, “A New Carbon based VUV Mirror of High Radiation Length for the HADES RICH” presented at the 4th International Workshop on Ring Imaging Cherenkov Detectors, Pylos, Greece, 5-10 June 2002.  
See <http://www.nestor.org.gr/rich2002/list/participants.htm> .
- [15] E. Albrecht *et. al.*, Nucl. Instrum. Meth. A **502**, 236 (2003).
- [16] The BTeV Proposal Update (2002).  
See: <http://www-btev.fnal.gov/cgi-bin/public/DocDB/ShowDocument?docid=316>
- [17] S. Stone and J. Butler, BTeV Internal document, BTeV-doc-1571.
- [18] T. Sjostrand and L. Lonnblad, Pythia 6.2, hep-ph/0108264, August 2001.
- [19] P. Lebrun *et. al.*, BTeV Internal document, BTeV-doc-113.